NADÁCIA VÝSKUM RAKOVINY

SÚŤAŽ MLADÝCH ONKOLÓGOV

YOUNG ONCOLOGIST AWARD 2026

PROCEEDINGS

Nadácia Výskum Rakoviny
(Cancer Research Foundation)

MARCH 10, 2026

Title: Young Oncologist Award competition 2026. Proceedings

The proceedings consist of peer-reviewed short papers and abstracts of presentations from the 2026 Young Oncologists Award Competition.

Authors: Alena Gábelová, PhD and Ján Sedlák, DSc.

Publisher: Nadácia Výskum Rakoviny (Cancer Research Foundation)
Karloveská 6C
841 04 Bratislava

www.nvr.sk
Bratislava, June 2026

Reviewers: Gabriela Pavlíková, PhD. and Margita Klobušická, PhD.

ISBN **978-80-971621-6-0**

CONTENT

LIST OF COMPETITORS IN INDIVIDUAL CATEGORIES

Undergraduate students

Hasanin E.H., Kovacsova T., Liener J.J., Maseda P., Naimushina L., Tothova M., Vagovicova B.

PhD students

Bernatova K., Fekiacova A., Fried A., Galvankova K., Gazova S., Hudakova L., Juhasikova L., Kloc D., Lukac B., Mojzesova N., Samuel R.D., Scasna K., Talac T., Tsokkou P., Vanova D., Vavrusakova B.

Post-docs up to 35 years

Heinzl N., Klein L., Moráňová L., Pacalajova M., Pös O., Szabóová D., Štefík P., Trnková L., Wu X.

Participants of the ***Young Oncologists Award*** competition

MEMBERS OF THE EVALUATION COMMITTEES

Category: **Undergraduate students**

Chairman: Univ. Prof. Shiv K. Singh, PhD.

Prof. Bruno Sainz, Jr., PhD.
Assoc. Prof. Sona Ciernikova, PhD.
Lucia Kucerova, DSc.
Lucia Messingerova, PhD.
Assoc. Prof. Michal Pastorek, PhD.
Bozena Smolkova, PhD.
Eliska Svastova, PhD.

Category: **PhD students**

Chairman: Assoc. Prof. Maria Dusinska, DSc

Andrea Babelova, PhD.
Assoc. Prof. Lubos Danisovic, PhD.
Jana Jakubikova, PhD.
Miroslava Matuskova, PhD.
Prof. Peter Racay, PhD.

Category: **Post-docs up to 35 years**

Chairman: Prof. Bruno Sainz, Jr., PhD.

Univ. Prof. Shiv K. Singh, PhD.
Assoc. Prof. Sona Ciernikova, PhD.
Lucia Kucerova, DSc.
Bozena Smolkova, PhD.
Eliska Svastova, PhD.

Members of the Evaluation Committees

WINNERS OF INDIVIDUAL CATEGORIES

Category: Undergraduate students

First place winner: Pablo MASEDA

Cancer Stem Cells and Fibroinflammatory Microenvironment Group, Instituto de Investigaciones Biomédicas Sols-Morreale; Biomarkers and Personalized Approach to Cancer Group, Instituto Ramón y Cajal de Investigación Sanitaria, Madrid, Spain

Univ. Prof. Shiv K. Singh, PhD. and Pablo Maseda

Second place winner: Barbora VAGOVICOVA

Department of Radiobiology, Cancer Research Institute, Biomedical Research Center of the Slovak Academy of Sciences, Bratislava, Slovak Republic

Univ. Prof. Shiv K. Singh, PhD. and Barbora Vagovicova

Third place winner: **Jan Jozef LIENER**

Department of Molecular Oncology, Cancer Research Institute, Biomedical Research Centre, Slovak Academy of Sciences, Bratislava; Piaristické gymnázium Františka Hanáka, Prievidza, Slovakia

Jan Sedlak, DSc., and Jan Jozef Liener

Category: PhD. students

First place winner: Panagiota TSOKKOU

Department of Dermatology, Medical University of Vienna, Austria

Assoc. Prof. Maria Dusinska, DSc., and Panagiota Tsokkou

Second place winner: **Rebecca Diya SAMUEL**

Department of Gastroenterology, GI-Oncology and Endocrinology, University Medical Center, Göttingen, Germany

Assoc. Prof. Maria Dusinska, DSc., and Rebecca Diya Samuel

Third place winner: Lucia JUHASIKOVA

Cancer Research Institute, Biomedical Research Center of the Slovak Academy of Sciences, Bratislava, Slovakia

Assoc. Prof. Maria Dusinska, DSc., and Lucia Juhasikova

Category: **Post-docs up to 35 years**

First place winner: **Lukas KLEIN**

Department of Gastroenterology, GI-Oncology and Endocrinology, University Medical Center Göttingen, Göttingen, Germany; Cancer Stem Cell Group, The Institute of Cancer Research, London, United Kingdom

Prof. Bruno Sainz, Jr., PhD. and Lukas Klein

Second place winner: **Lenka TRNKOVA**

Department of Molecular Oncology, Cancer Research Institute, Biomedical Research Center of the Slovak Academy of Sciences, Bratislava, Slovakia

Prof. Bruno Sainz, Jr., PhD. and Lenka Trnkova

Third place winner: **Xueyan WU**

Department of Gastroenterology, GI-Oncology and Endocrinology, University Medical Center Göttingen, Germany

Prof. Bruno Sainz, Jr., PhD. and Xueyan Wu

SHORT PAPERS & ABSTRACTS OF PRESENTATIONS

PROGNOSTIC EFFECT OF NON-PHOTOACTIVATED HYPERICIN IN HYPOXIA ON THE MIGRATORY POTENTIAL OF LUNG CARCINOMA CELLS

Tamara Kovacsova, Viktoria Decmanova, Rastislav Jendzelovsky, Peter Fedorocko

Pavol Jozef Safarik University in Kosice, Faculty of Science, Institute of biology and ecology, Srobarova 2, 041 54 Kosice, Slovakia

Introduction

Carcinomas, tumors of epithelial origin, represent the most numerous type of tumors and account for approximately 80 – 90 % of all diagnosed malignancies. A key property of epithelial cancer cells is the ability to acquire migratory and invasive potential, which leads to tumor progression and metastasis to distant tissues. The process involved in acquiring these properties is the epithelial-mesenchymal transition (EMT), during which cells lose their epithelial characteristics and acquire a mesenchymal phenotype accompanied by increased motility, migration, invasion, and the ability to colonize distant sites. EMT is a dynamic and tightly regulated process in which several transcription factors (TF), mainly from the Snail, Twist, and Zeb families, participate. Among them, Snail1 plays a key role, acting as the main initiator of EMT. A significant factor influencing EMT is hypoxia, which is a characteristic feature of the microenvironment of solid tumors. Hypoxic conditions lead to the stabilization of hypoxia-inducible factors HIF-1α and HIF-2α, which regulate the expression of genes involved in cell adaptation to oxygen deficiency, but also genes encoding EMT-TFs, including Snail1, thereby contributing to a more aggressive phenotype of cancer cells. Currently, increasing attention is being paid to bioactive natural compounds as potential modulators of tumor processes. One such compound is hypericin, a secondary metabolite of plants of the genus *Hypericum*, known for its broad-spectrum biological effects. In addition to its use as a photosensitizer in photodynamic diagnosis and therapy, the effects of its non-photoactivated form, which exhibits anticancer properties independent of light activation, are also being investigated. It has been shown that hypericin under hypoxic conditions can modulate the levels of HIF-1α [1,2]. Moreover, hypericin has been shown to affect the properties of the SP population with a cancer stem cell phenotype, reducing its size [3], although the surviving SP cells exhibit increased migratory potential [2].

The aim of this study was therefore to investigate the effect of non-photoactivated hypericin under hypoxic conditions on the migratory potential of the entire A549 lung

cancer cell population, with a focus on HIF signaling and Snail1. A key aspect of this work was the evaluation of functional cell behaviour, particularly migratory ability, which is a critical factor contributing to the invasive and metastatic potential of cancer cells. At the same time, we investigated whether these effects depend on hypericin concentration and oxygen conditions (normoxia and hypoxia) in order to better understand its potential mechanisms of action in the tumor microenvironment and its possible use in anticancer therapy.

Material and methods

Cell cultivation.

In our experiments, the human lung adenocarcinoma cell line A549 (ATCC) was used. Cells were cultured under standard conditions (37 °C, 20 % O_2, 5 % CO_2 and 75 % N_2) in RPMI-1640 medium (Sigma-Aldrich) supplemented with 10 % fetal bovine serum (FBS; Biosera), antibiotics, and antimycotics. At the beginning of each experiment, cells were seeded at densities adjusted to reach 80 % confluence at the time of analysis for the methods described below. The initial density was 15,000 cells/cm^2 for 16-hour incubation with hypericin and 10,000 cells/cm^2 for 40-hour incubation with hypericin. Cells were cultured under standard (normoxic) or hypoxic conditions (37 °C, 1 % O_2, 5 % CO_2, and 94 % N_2) in a hypoxic chamber (Coy Laboratory Products).

Reagents.

A 2 mM stock solution of hypericin (Sigma-Aldrich) was prepared in dimethyl sulfoxide (DMSO) (Sigma-Aldrich) and stored at -80 °C. Working solutions of hypericin (1 and 5 μM) were diluted in culture medium containing 10 % FBS and added to the cells after 24 hours of hypoxic cultivation in the dark to prevent photoactivation.

Western blot analysis.

Cells were harvested 16 and 40 hours after hypericin treatment by scraping on ice, washed with cold PBS and lysed in cold lysis buffer supplemented with protease and phosphatase inhibitors. Protein concentration was determined using the Lowry method, and samples were adjusted to equal protein amounts. Proteins were separated by SDS-PAGE (10 % gel) and transferred onto PVDF membranes (Bio-Rad). Membranes were blocked with 5 % milk and incubated overnight at 4 °C with primary antibodies. After washing, HRP-conjugated secondary antibodies were added to the membranes. Protein expression was detected using a chemiluminescent substrate (Pierce ECL, Thermo Scientific) and visualized on X-ray film (AGFA). Densitometric analysis was performed using ImageLab software (Bio-Rad), and protein levels were normalized to the reference protein β-actin.

Migration analysis.

Cell migration was assessed using a wound healing assay under normoxic and hypoxic conditions with either 16-hour preincubation or continuous incubation with hypericin. Cells (15,000 cells/cm^2) were seeded into 96-well plates (Sartorius). After 24 hours, hypericin (1 and 5 μM) was added, and cells were incubated for 16 hours. The medium containing 10 % FBS was then replaced with medium containing 1 % FBS to inhibit cell proliferation. In the preincubation group, hypericin was removed, whereas in the continuous incubation group, hypericin was re-added with the medium containing 1 % FBS. After 24 hours of proliferation inhibition, a wound (scratch) was created in the cell monolayer using a WoundMaker (Essen BioScience). Cells were washed with sterile PBS and incubated in medium containing 1 % FBS with or without hypericin. Cell migration (wound closure rate) was monitored and quantified using IncuCyte ZOOM software at 3-hour intervals for 96 hours.

Statistical analysis.

Data are presented as mean ± standard deviation (SD). One-way ANOVA followed by Tukey's post-hoc test was used for multiple group comparisons. Two-way ANOVA followed by Bonferroni's post-hoc test was used to evaluate the effects of hypericin treatment and experimental conditions (normoxia and hypoxia). Statistical significance is indicated in each figure and its caption.

Results

Effect of hypoxia and hypericin on HIF-1α protein levels

Since the study of Barliya et al. [1] demonstrated that non-photoactivated hypericin reduced the levels of HIF-1α protein, the aim of the initial experiment was to verify the effect of 5 μM hypericin on the level of this protein in A549 cells incubated under normoxic and hypoxic conditions.

The increased level of HIF-1α in hypoxic control groups confirmed the correct induction of hypoxic conditions in our experiments (Fig. 1). Five μM hypericin significantly reduced HIF-1α protein levels after 16 hours of incubation under hypoxic conditions. A decrease was also observed after 40 hours of incubation; however, this decrease was not statistically significant. A decrease in HIF-1α levels was also observed after incubation with hypericin under normoxic conditions despite the low basal levels of HIF-1α, but without statistical significance (Fig. 1).

Effect of hypoxia and hypericin on Snail1 protein levels

HIF-1α is one of the main regulatory factors of the hypoxic response and is known to stimulate the expression of TF families associated with EMT. Based on this, we focused on the analysis of the TF Snail1, which is considered a key regulator of this process.

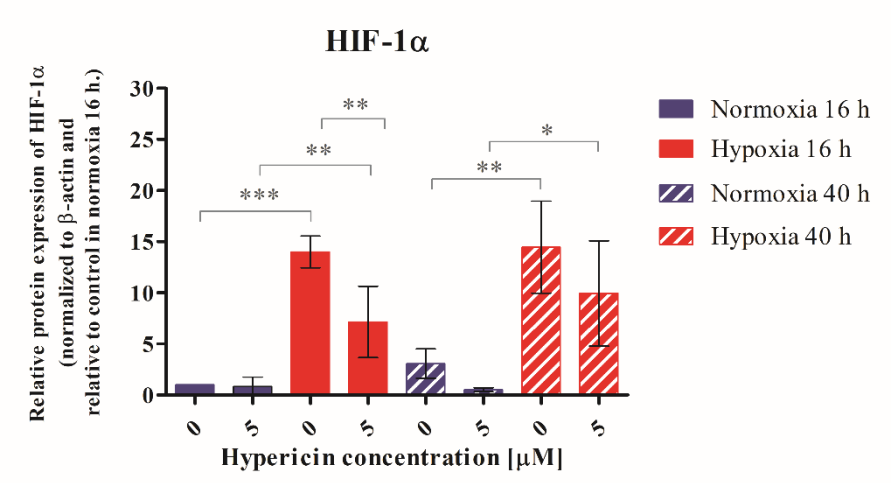

Figure 1. Effect of hypoxia and hypericin on HIF-1α. HIF-1α protein levels were analyzed by Western blotting at 16 and 40 hours of incubation of cells with hypericin in normoxia and hypoxia. Protein levels were normalized to β-actin and relative to the control at 16 h in normoxia. Results are presented as mean ± SD of three biological replicates. Statistical analysis was performed by two-way ANOVA for each analyzed time point (16 h and 40 h) separately with Bonferroni post-hoc test (* $p < 0.05$; ** $p < 0.01$; *** $p < 0.001$).

Hypoxic conditions led to a significant increase in Snail1 protein levels, particularly after 16 hours of incubation with hypericin, compared to the normoxic control. At the later analyzed time point (40 h), we did not observe an increase in the level of Snail1 in hypoxia compared to normoxia (Fig. 2).

We found that 5 μM hypericin significantly decreased Snail1 protein levels after 16 hours of incubation under hypoxic conditions and after 40 hours of incubation under both normoxic and hypoxic conditions (Fig. 2).

Modulation of cell migration by hypericin

Based on previous results showing that hypericin reduces Snail1 protein levels, we also investigated its effect on cell migration. A functional migration assay, known as the wound healing assay, was used to evaluate changes in cell migratory activity.

The results showed that preincubation of cells with 1 or 5 μM hypericin did not affect their migration capacity under normoxic (Fig. 3A) and hypoxic conditions (Fig. 3B). Conversely, continuous incubation of cells with hypericin (1 and 5 μM) resulted in a statistically significant reduction in their migratory ability both under normoxic (Fig. 3A) and hypoxic conditions (Fig. 3B).

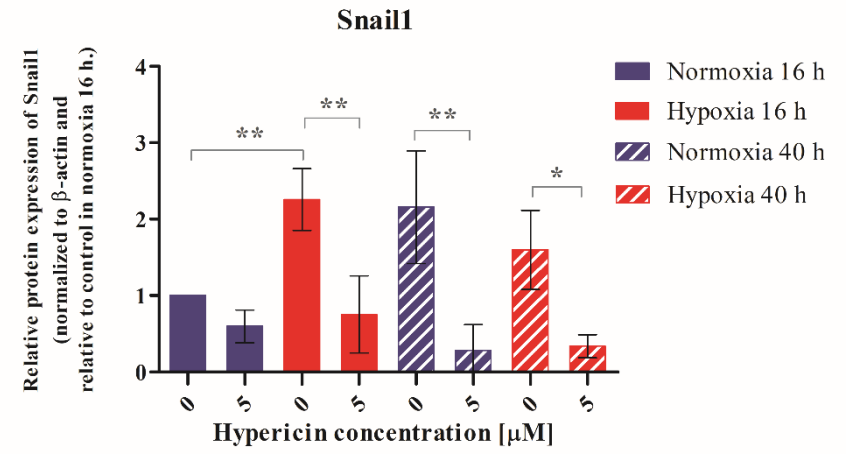

Figure 2. Effect of hypoxia and hypericin on Snail1. Snail1 protein level was analyzed by Western blotting after 16 and 40 hours of incubation of cells with hypericin in normoxia and hypoxia. Protein level was normalized to β-actin protein level and relative to the control in normoxia 16 h. Results are presented as mean ± SD of three biological replicates. Statistical analysis was performed by two-way ANOVA for each analyzed time point (16 h and 40 h) separately with Bonferroni post-hoc test (* $p < 0.05$; ** $p < 0.01$).

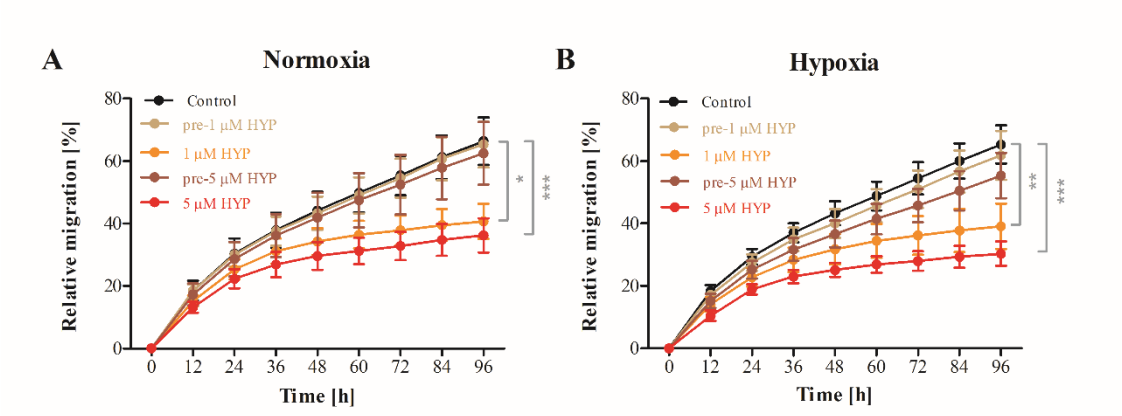

Figure 3. Changes in the migratory potential of cancer cells under the influence of hypericin. The graphs show the course of migration expressed as relative wound density (%) in A) normoxic and B) hypoxic conditions after 16-hour preincubation of cells with 1 and 5 μM hypericin and during continuous incubation of cells with 1 and 5 μM hypericin. The results are presented as mean ± SD of two biological replicates with two technical replicates. Statistical analysis was performed by one-way ANOVA with Tukey's post-test. Changes in the migratory activity of experimental groups were compared with the respective control (* $p < 0.05$; ** $p < 0.01$; *** $p < 0.001$).

Discussion

Barliya et al. [1] were the first to demonstrate that hypericin reduces HIF-1α protein levels. A later study using lower concentrations of hypericin (0.1, 0.5, 1 and 5 μM) observed the strongest reduction in HIF-1α levels after 16 hours of incubation with 5 μM hypericin in hypoxia [2]. The elevated HIF-1α levels in hypoxic controls compared to normoxic controls confirmed the validity of hypoxia induction in our experimental setup. Consistent with previous findings, our results show that 5 μM hypericin significantly decreased HIF-1α protein levels, with the strongest effect detected at 16 h in hypoxia. The absence of a significant decrease in HIF-1α in the later phase of hypoxia may reflect an adaptive response of cells to hypoxia. It has been shown that the regulation of HIF factors during hypoxia is dynamic and varies depending on the duration of hypoxic exposure as well as the cell line tested [4, 5]. This time-dependent mechanism may lead to the attenuation of the effect of hypericin despite the persistently elevated levels of HIF-1α.

Given that Snail1 is considered one of the strongest inducers of EMT [6] and is regulated by HIF-1α [7], we next analyzed the expression of this protein. As expected, hypoxia significantly increased Snail1 levels at the earlier analyzed time (harvest at 16 h), which confirmed its regulation by HIF-mediated signaling. However, a slight decrease in Snail1 levels in hypoxia at the later analyzed time (harvest at 40 h) may reflect the adaptive mechanisms of cells to long-term hypoxia, during which the stability of HIF-1α protein is disrupted [4]. This may lead to an alteration in its transcriptional activity and consequently to a weakened induction of its target genes, such as Snail1. Importantly, hypericin (5 μM) significantly reduced Snail1 levels at both time points in hypoxia, supporting the hypothesis that hypericin interferes with hypoxia-driven EMT, probably through inhibition of HIF signaling [1, 2].

To assess the functional relevance of these molecular changes, we analyzed the migratory activity of the entire A549 cell population. In the experiment, cells were treated with 1 μM or 5 μM hypericin either by 16-hour preincubation or by continuous incubation throughout the analysis. The results showed that hypericin at both concentrations (1 μM and 5 μM) significantly reduced the migratory activity of cells, but only during continuous incubation, both under normoxic and hypoxic conditions. Notably, the antimigratory effect correlated with reduced Snail1 levels at 5 μM, supporting its role in migration control. However, migration was also inhibited at 1 μM, where no significant change in Snail1 expression was observed, indicating that additional mechanisms beyond Snail1 regulation likely contribute to the observed phenotype. In contrast, Buľková et al. (2023) demonstrated that a 16-hour preincubation of SP cells isolated from the same A549 cell population with 1 μM hypericin under hypoxic conditions led to an increase in their migratory activity. The authors report that the combination of hypericin and hypoxia reduced the size of this subpopulation, but the remaining surviving SP cells showed an increased migratory potential, suggesting the

selection of a more aggressive subpopulation of cells with a CSC phenotype [2]. These differences in the response of the SP subpopulation and the entire cell population to hypericin indicate a significant heterogeneity of the tumor population. While hypericin may have an antimigratory effect on the entire cell population, it may have a different, potentially adverse effect on a minority subpopulation with CSC properties. This aspect should also be taken into account in its therapeutic application, for example as a potential neoadjuvant drug aimed at reducing tumor invasiveness. Moreover, a clinical study of hypericin demonstrated that synthetic hypericin was well tolerated in patients with recurrent glioma and in some cases led to stabilization or even reduction in tumor size [8]. While that study focused primarily on clinical outcomes, our *in vitro* results further extend these findings and suggest that hypericin may represent a promising candidate for neoadjuvant therapeutic strategies aimed at limiting cancer cell migration and invasiveness, potentially reducing the risk of metastasis prior to surgery.

Conclusion

Overall, it can be concluded that hypericin modulates hypoxia-regulated signaling pathways and affects the migratory potential of A549 cancer cells. Our results indicate that hypericin could represent a promising candidate for reducing cancer cell migration, thereby potentially limiting their ability to metastasize, particularly in neoadjuvant therapeutic strategies.

Acknowledgements

This work was supported by the Scientific Grant Agency of the Ministry of Education of the Slovak Republic under the contract No. VEGA 1/0003/23.

References

[1] Barliya T, Mandel M, Livnat T, Weinberger D, Lavie G. Degradation of HIF-1alpha under Hypoxia Combined with Induction of Hsp90 Polyubiquitination in Cancer Cells by Hypericin: a Unique Cancer Therapy. PLoS ONE 2011; 6: e22849. doi: 10.1371/journal.pone.0022849

[2] Buľková V, Vargová J, Babinčák M, Jendželovský R, Zdráhal Z et al. New findings on the action of hypericin in hypoxic cancer cells with a focus on the modulation of side population cells. Biomed Pharmacother 2023; 163: 114829. doi: 10.1016/j.biopha.2023.114829

[3] Vargová J, Mikeš J, Jendželovský R, Mikešová L, Kuchárová B et al. Hypericin affects cancer side population via competitive inhibition of BCRP. Biomed Pharmacother 2018; 99: 511-522. doi: 10.1016/j.biopha.2018.01.074

[4] Lin Q, Cong X, Yun Z. Differential Hypoxic Regulation of Hypoxia-Inducible Factors 1α and 2α. Mol Cancer Res 2011; 9: 757-765. doi: 10.1158/1541-7786.MCR-11-0053

[5] Von Fournier A, Wilhelm C, Tirtey C, Stöth M, Kasemo TE et al. Impact of Hypoxia and the Levels of Transcription Factor HIF-1α and JMJD1A on Epithelial-Mesenchymal

Transition in Head and Neck Squamous Cell Carcinoma Cell Lines. Cancer Genomics Proteomics 2024; 21: 591-607. doi: 10.21873/cgp.20476

[6] Gras B, Jacqueroud L, Wierinckx A, Lamblot C, Fauvet F et al. Snail Family Members Unequally Trigger EMT and Thereby Differ in Their Ability to Promote the Neoplastic Transformation of Mammary Epithelial Cells. PLoS ONE 2014; 9: e92254. doi: 10.1371/journal.pone.0092254

[7] Zhang L, Huang G, Li X, Zhang Y, Jiang Y et al. Hypoxia induces epithelial-mesenchymal transition via activation of SNAI1 by hypoxia-inducible factor -1α in hepatocellular carcinoma. BMC Cancer 2013; 13: 108. doi: 10.1186/1471-2407-13-108

[8] Couldwell WT, Surnock AA, Tobia AJ, Cabana BE, Stillerman CB et al. A phase 1/2 study of orally administered synthetic hypericin for treatment of recurrent malignant gliomas. Cancer 2011; 117: 4905-4915. doi: 10.1002/cncr.26123

XANTHOHUMOL IN COMBINED THERAPY OF PANCREATIC DUCTAL ADENOCARCINOMA: SYNERGISTIC EFFECT WITH GEMCITABINE AND EPIGENETIC ANALYSIS

Jan Jozef Liener[1,2], Bozena Smolkova[1], Viera Horvathova-Kajabova[1], Lenka Trnkova[1], Tatiana Klempova[3,4]

[1]*Department of Molecular Oncology, Institute of Experimental Oncology, Biomedical Research Centre, Slovak Academy of Sciences, Dúbravská cesta 9, 845 05 Bratislava, Slovakia*
[2]*František Hanák Piarist Gymnasium in Prievidza*
[3]*Faculty of Chemical and Food Technology, Slovak University of Technology, Bratislava, Slovakia*
[4]*Central Laboratories, Faculty of Chemical and Food Technology, Slovak University of Technology, Bratislava, Slovakia*

Introduction

Eight percent. That is how many PDAC patients are still alive five years after diagnosis [1]. The number has barely moved in decades. Around 90% of patients arrive already past the point of surgery [1], and gemcitabine (GEM), one of the main treatments, loses its effect fairly quickly once tumour cells develop resistance [2]. Finding something that could keep it working longer, or make tumour cells more sensitive to it, would matter.

Xanthohumol (XN) is a flavonoid from hop cones (*Humulus lupulus*) with published anticancer activity in several tumour types including pancreatic cancer [3]. Safety at relevant concentrations demonstrates a favourable safety profile . The main obstacle was cost. Commercial XN runs at around EUR 375 per 5 mg, and at that price running a proper multi-condition study gets expensive fast. So we extracted it from dried hops ourselves and compared it to the commercial product. We could not find this kind of direct comparison in a PDAC experiment in the literature.

At the same time, we wanted to look at DNA methylation. In PDAC, genes like fibronectin 1 (FN1) and N-cadherin (CDH2) are often silenced by hypermethylation of their promoters [4]. Both play a role in how tumour cells invade and spread. Some flavonoids have been shown to interfere with the enzymes that control methylation [5]. Whether XN does anything similar in PDAC was not clear.

The study had two main aims: to develop and cost-compare an in-house xanthohumol isolation method, and to test both the in-house material and the commercial

version, alone and combined with gemcitabine, in two PDAC cell lines, with DNA methylation and epigenetic enzyme expression measured alongside.

Materials and Methods

Cell lines.
MIA PaCa-2 is derived from a primary tumour and is relatively sensitive to treatment. SU.86.86 came from a liver metastasis and is harder to affect with standard agents. Using both gave us a way to test whether results from the more sensitive line would hold up in a more resistant context

Xanthohumol isolation.
We developed a seven-step protocol from dried *Humulus lupulus* cones: milling, defatting with n-hexane, three rounds of ethanol extraction (96%), rotary evaporation at or below 35°C, liquid-liquid extraction with ethyl acetate, silica gel column chromatography with a hexane/EtOAc gradient, and crystallisation in ethanol/water at 4°C. Purity was confirmed by TLC and HPLC. This preparation is called XI throughout. Commercial xanthohumol (XK; CAS No. 6754-58-1, Hangzhou Hyper Chemicals Limited, China) was run in parallel in every experiment. Costs for both were tracked.

Cell viability.
Cells (5,000–8,000 per well in 96-well plates) were treated with XK or XI across a concentration range for 72 hours. Viability was measured with the CellTiter-Glo assay; IC50 values. For combination experiments, XI was added first for 72 hours, then gemcitabine (GEM) at 20 nM for three more days. Decitabine (DAC) was included as a reference compound. DMSO was kept at or below 0.1%.

Synergy analysis.
Synergy between XI and GEM was assessed using SynergyFinder version 3.0 [6] with four models: ZIP, HSA, Loewe, and Bliss. Scores above 10 indicate strong synergy. Statistical significance was assessed for all four models.

DNA methylation.
Genomic DNA was bisulfite-converted and *FN1* and *CDH2* promoter methylation was measured by pyrosequencing (PyroMark Q24). DAC served as positive control; we had used it in this cell system previously [4].

Gene expression.
DNMT1 and *TET1* mRNA levels were measured by RT-qPCR from total RNA, with *HPRT1* as the reference gene.

Ethical approval.
As only established commercial cell lines were used and no patient material was involved, no ethics committee approval was required.

Results

Isolation of xanthohumol
Starting from 10 g of dried hops, we obtained 20 mg of xanthohumol (0.2% yield, 92% purity by HPLC). The cost was about EUR 125 per 5 mg, compared to EUR 375 for the commercial product.

Single-agent cytotoxicity.
Both XK and XI reduced viability in PDAC cells in a dose-dependent manner (Figure 1). In MIA PaCa-2, XK IC50 was about 12 µM and XI about 19 µM. In SU.86.86 the gap was larger: XK was still active (IC50 roughly 22µM) but XI had almost no effect at 25 µM (viability above 85%). Decitabine had modest effects in both lines (MIA PaCa-2: 82–95% viability; SU.86.86: 62–81%).

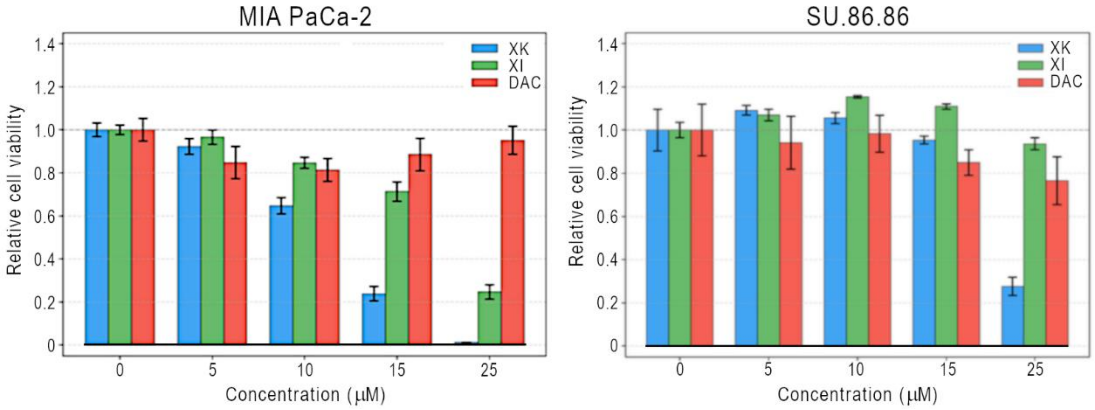

Figure 1. Relative cell viability in MIA PaCa-2 (left) and SU.86.86 (right) after 72-hour treatment with commercial xanthohumol (XK), in-house isolated xanthohumol (XI), and decitabine (DAC). Error bars represent standard deviation.

Combination with gemcitabine. GEM at 20 nM left 97% of SU.86.86 cells alive, and XI alone at tested concentrations had little effect on this line. The combination brought viability down substantially in both lines (Figure 2). In SU.86.86, viability fell to 1.9% at the highest combination dose (XI 20 µM + GEM 20 nM). In MIA PaCa-2 the same dose reduced viability to 12%, compared to 31% with XI alone. Both experiments were performed in duplicates .

Synergy scores. MIA PaCa-2: ZIP 10.53, HSA 11.82, Loewe 10.70, Bliss 11.25. SU.86.86: ZIP 18.77, HSA 20.19, Loewe 15.18, Bliss 19.69. All values exceeded 10 and all were statistically significant at $p < 0.001$ (MIA PaCa-2: ZIP $p = 4.68\times10\text{-}7$, HSA $p = 4.96\times10\text{-}6$, Loewe $p = 5.03\times10\text{-}5$, Bliss $p = 4.64\times10\text{-}6$; SU.86.86: ZIP $p = 7.38\times10\text{-}4$, HSA $p = 5.26\times10\text{-}4$, Loewe $p = 1.31\times10\text{-}3$, Bliss $p = 7.10\times10\text{-}4$). Scores in SU.86.86 were roughly double those in MIA PaCa-2.

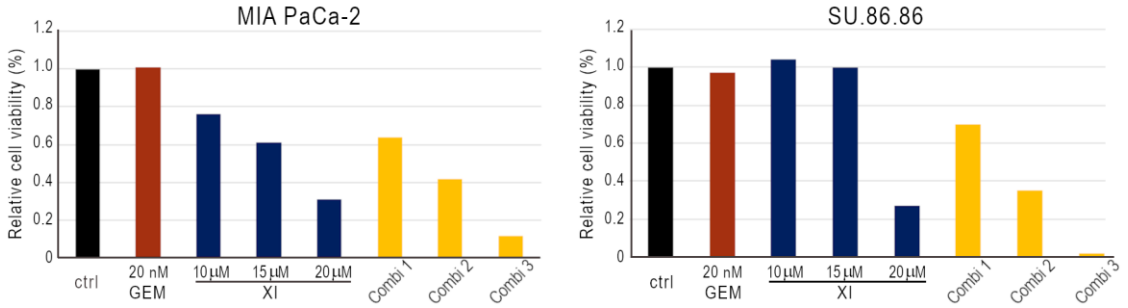

Figure 2. Relative cell viability after combination treatment in MIA PaCa-2 (left) and SU.86.86 (right). Cells were pre-treated with XI for 72 hours followed by GEM at 20 nM for 72 hours. Combi 1: XI 10 µM + GEM 20 nM; Combi 2: XI 15 µM + GEM 20 nM; Combi 3: XI 20 µM + GEM 20 nM.

DNA methylation. XN did not reduce FN1 or CDH2 promoter methylation in either line. In MIA PaCa-2, both genes were heavily methylated at baseline (FN1 84%, CDH2 98%) and remained so after XN treatment. In SU.86.86, baseline methylation was already low (4–5%). DAC reduced FN1 methylation to 43% and CDH2 to 47% in MIA PaCa-2, confirming the assay was working correctly.

Gene expression of epigenetic regulators. In SU.86.86, both DNMT1 and TET1 expression went down after XN treatment (Figure 3). In MIA PaCa-2 the changes were smaller and less consistent.

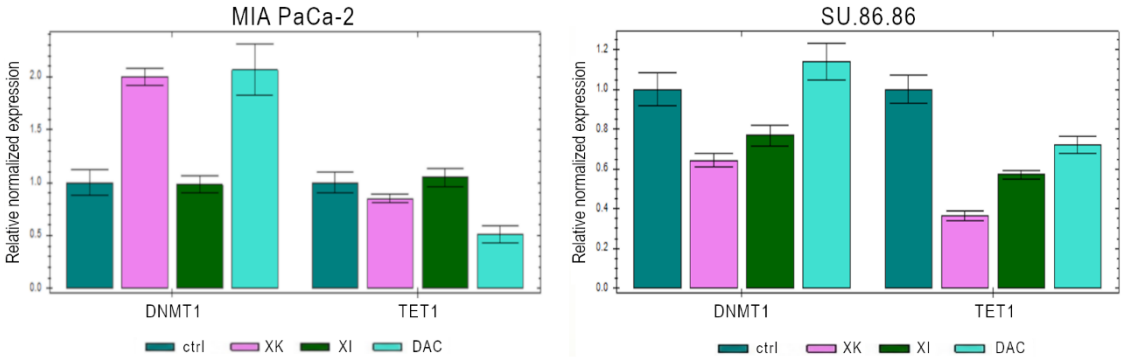

Figure 3. Relative normalized expression of DNMT1 and TET1 in MIA PaCa-2 (left) and SU.86.86 (right) after treatment with XK, XI, and DAC, measured by RT-qPCR. HPRT1 was used as the reference gene. Error bars represent standard deviation.

Discussion

The effect of combination therapy on SU.86.86 was the result we checked twice. GEM at 20 nM does nothing this cell line‘s viability : 97% of cells survive monotherapy. XI alone at tested doses had little effect either. When both drugs were combined, viability fell below 2%. Synergy scores in SU.86.86 were roughly double those in MIA

PaCa-2, which is the opposite of what you would typically expect from a more resistant line.

Palanisamy et al. [7] demonstrated synergistic anticancer activity of xanthohumol in combination with another phytochemical in PDAC models, including in vivo, but did not examine interactions with gemcitabine or behaviour in a resistant line. Our guess is that the resistance adaptations in SU.86.86 (possibly changes in nucleoside transport or metabolic enzyme expression) create a specific vulnerability that XN can use. To test that properly, we would need to measure transporter expression and intracellular GEM handling directly.

XI worked well enough for this type of experiment. The IC50 difference in MIA PaCa-2 (19 μM vs. 12 μM for XK) most likely comes from the lower purity, and for precise pharmacology work XK is the better choice. For testing many conditions on a limited budget, XI at one-third of the cost is a reasonable option.

XN did not demethylate the *FN1* or *CDH2* promoters. DAC did, under the same conditions, so the assay was working. These findings indicate that XN does not exert hypomethylating effects on the *FN1* or *CDH2* promoters under the tested conditions

The *DNMT1* and *TET1* changes in SU.86.86 confirm the effect of XN on enzymes involved in DNA methylation regulation. Both went down after XN treatment. Since they work in opposite directions on methylation, losing both at once does not give a simple prediction of the net effect. Link et al. [5] noted that polyphenols can shift enzyme levels without producing consistent locus-specific changes, and our data fit that picture. In MIA PaCa-2 the pattern was different. This work has several limitations. Cell culture cannot capture the full complexity of a real tumour, and whether XN reaches the needed concentrations in actual tissue is not known.

Conclusion

XN and gemcitabine show strong synergy in PDAC cells, confirmed by four independent models with p-values well below 0.001 in both lines tested. The largest effect was in a drug-resistant metastatic line where neither agent does much on its own. In-house isolation from hop cones gave 92% purity material at about one-third of the commercial cost. XN did not demethylate *FN1* or *CDH2* promoters directly, but reduced *DNMT1* and *TET1* expression in SU.86.86, suggest a mechanism different from DAC. The precise mechanism behind the synergy is not yet clear.

Acknowledgement

The authors acknowledge the Hangzhou Hyper Chemicals Limited, China, for providing xanthohumol for their experiments. This research received no specific grant from any funding agency.

References

[1] Ubezio P, Falcetta F, Carrassa L, Lupi M. Integrated experimental and simulation study of the response to sequential treatment with erlotinib and gemcitabine in pancreatic cancer. *Oncotarget* 2016; 7:15492–15506. doi: 10.18632/oncotarget.7491.

[2] Nevala-Plagemann C, Hidalgo M & Garrido-Laguna I. From state-of-the-art treatments to novel therapies for advanced-stage pancreatic cancer. Nat Rev Clin Oncol 2020; 17: 108–123. doi: 10.1038/s41571-019-0281-6
[3] Kunnimalaiyaan S, Trevino J, Tsai S, Gamblin TC, Kunnimalaiyaan M. Xanthohumol-Mediated Suppression of Notch1 Signaling Is Associated with Antitumor Activity in Human Pancreatic Cancer Cells. Mol Cancer Ther 2015; 14(6): 1395–1403. doi: 10.1158/1535-7163.MCT-14-0915
[4] Maria Urbanova, Verona Buocikova, Lenka Trnkova, Sabina Strapcova, Viera Horvathova Kajabova et al. DNA methylation mediates EMT gene expression in human pancreatic ductal adenocarcinoma cell lines. Int J Mol Sci 2022; 23: 2117. doi: 10.3390/ijms23042117
[5] Link A, Balaguer F, Goel A. Cancer chemoprevention by dietary polyphenols: promising role for epigenetics. Biochem Pharmacol 2010; 80: 1771-1792. doi: 10.1016/j.bcp.2010.06.036
[6] Ianevski A, Giri AK, Aittokallio T. SynergyFinder 3.0: an interactive analysis and consensus interpretation of multi-drug synergies across multiple samples. Nucleic Acids Res 2022; 50: W739-W743. doi: 10.1093/nar/gkac382
[7] Palanisamy R, Kahingalage NI, Archibald D, Casari I, Falasca M. Synergistic Anticancer Activity of Plumbagin and Xanthohumol Combination on Pancreatic Cancer Models. Int J Mol Sci 2024; 25: 2340. doi: 10.3390/ijms25042340
[8] Fang MZ, Wang Y, Ai N, Hou Z, Sun Y, Lu H et al. Tea polyphenol (-)-epigallocatechin-3-gallate inhibits DNA methyltransferase and reactivates methylation-silenced genes in cancer cell lines. Cancer Res 2003; 63: 7563-7570. doi: 10.1158/0008-5472.CAN-03-2983

A TROJAN HORSE APPROACH TO EXPLOITING RIBOFLAVIN UPTAKE FOR TARGETED THERAPY IN PANCREATIC CANCER STEM CELLS

Pablo Maseda[1,2,3], Adrian Palencia-Campos[1,2], Diego Navarro[1,2,3], Sandra Batres-Ramos[1,2,3], Sonia Alcala[1,2], Bruno Sainz Jr.[1,2]

[1]*Cancer Stem Cells and Fibroinflammatory Microenvironment Group, Instituto de Investigaciones Biomédicas Sols-Morreale (IIBM, CSIC-UAM), 28029 Madrid*
[2]*Biomarkers and Personalized Approach to Cancer Group (BIOPAC), Instituto Ramón y Cajal de Investigación Sanitaria (IRYCIS), Área 3 Cáncer, 28049 Madrid*
[3]*Department of Biochemistry, Autónoma University of Madrid (UAM), 28029 Madrid*

Introduction

Pancreatic ductal adenocarcinoma (PDAC) is a metastatic and chemo-refractory tumor with a 11 % 5-year survival rate [1], partly due to a subpopulation within the tumor known as cancer stem cells (CSCs). CSCs make up 2-5 % of the tumor mass and are responsible for tumor heterogeneity due to their self-renewal capacity and their intrinsic ability to differentiate into different cancer cell lineages. They are also believed to play an important role in the onset of tumor relapses and metastases, drug resistance and treatment failure [2]. This has inspired the design of innovative antitumoral strategies aimed at eliminating CSCs, for which it is necessary to locate them specifically. While there are validated cell surface markers to distinguish CSCs from other tumor cells, none have proven to be universal. Dr. Bruno Sainz's laboratory discovered that CSCs of various epithelial tumors contain intracellular vesicles coated with the ATP transporter ABCG2, responsible for the accumulation of naturally fluorescent vitamin B2 (i.e., riboflavin) within these vesicles [3]. This allows for CSC identification and isolation based on their intrinsic autofluorescence (AF) using fluorescence-based techniques.

Riboflavin is the precursor of flavin mononucleotide (FMN) and flavin adenine dinucleotide (FAD), cofactors of numerous flavoenzymes involved in oxidative phosphorylation (OXPHOS). Indeed, CSCs of many tumor types, such as PDAC, preferentially rely on aerobic OXPHOS over anaerobic glycolysis, typical of regular cancer cells [4]. The role that this accumulated riboflavin plays in CSC physiology is unclear, but it is reasonable to predict that it may represent a limiting factor in OXPHOS metabolism and, therefore, an intrinsic susceptibility of CSCs. Given that riboflavin accumulation in CSCs is mediated by ABCG2-coated vesicles, they may also accumulate riboflavin analogs or derivatives, such as lumichrome, which could cause competitive interference with riboflavin-dependent metabolic pathways (e.g.,

OXPHOS). Preliminary data from the laboratory showed that lumichrome administration to primary cultures of PDAC cells generated from patient-derived xenografts (PDX) resulted in a marked reduction in the AF-positive (AF^+) CSC populations (unpublished data), suggesting that it is replacing riboflavin. However, it yielded a notable toxicity.

Nanotechnology is emerging as a promising tool in the biomedical field. Miglyol® is a medium-chain triglyceride line frequently used in lipid nanoemulsion (NE) formulations due to its ability to dissolve hydrophobic drugs (e.g., lumichrome), enhancing drug loading capacity and stability. Furthermore, using Miglyol® would help augment lumichrome's biocompatibility for future *in vivo* approaches. Thus, Miglyol®-based NEs containing lumichrome could be a feasible therapeutic way of maintaining lumichrome's effects while limiting its toxicity.

Building on this strategy, additional approaches that further potentiate lumichrome's activity are of particular interest. A recent study has shown that exposure to blue light can significantly potentiate antitumoral treatment by inducing oxidative stress and mitochondrial dysfunction, in a distincly effective way when combined with blue-absorbing photosensitizers like riboflavin [5]. Thus, given that CSCs are highly dependent on OXPHOS and display an increased intracellular accumulation of riboflavin, it is reasonable to think that blue light exposure could sensitize them to metabolic perturbations. Furthermore, assuming that lumichrome retained riboflavin's photoreactive properties while displacing it, its effect could be combined with that of blue light exposure. That is, blue light could exacerbate mitochondrial vulnerabilities in lumichrome-loaded CSCs while maintaining low systemic toxicity, providing a novel strategy to target pancreatic CSCs. Once CSCs are depleted, standard-of-care chemotherapy (e.g., gemcitabine) should eliminate the remaining tumor cells, minimizing the risk of tumor relapse.

Materials and methods

Primary Human PDAC Cells.

Human PDAC tumors were obtained from Dr. Manuel Hidalgo under a Material Transfer Agreement with the Spanish National Cancer Research Centre (Ref. No. I409181220BSMH). Tumor samples were maintained by implantation into immunocompromised NOD/SCID and NU/NU mice, generating a library of PDAC PDXs. PDXs were generated in accordance with protocols approved by the Animal Care and Use Committee from Universidad Autónoma de Madrid (Ref. No. CEI-25-587) and Comunidad de Madrid (PROEX 294/19, 205.23). Cell cultures used in this work were derived from mechanical and enzymatic digestion of PDAC PDXs, and their use was approved by the Spanish National Research Council (CSIC) Ethical Committee (Ref. No. 329/2024). Primary PDX-derived *in vitro* cultures are referred to by their patient number designation (A6L, 185). 185 scd refers to a culture derived from an AF-sorted single cell of the 185 parental human tumor sample; its culture exhibits a higher percentage of autofluorescent CSCs. Cells were cultured in RPMI 1640 Medium (Corning, Cat. No. 10-040-CV) supplemented with 10 % fetal bovine serum (FBS, Invitrogen, Cat. No. 10270106), 0.4 % glutamine (Corning, Cat. No. 25-005-CI), 100 U/mL

penicillin/streptomycin (Invitrogen, Cat. No. 15140122) and 0.4 % fungizone (Invitrogen, Cat. No. 15290018).

Reagents

Lumichrome (Sigma-Aldrich, Cat. No. 103217) was dissolved in dimethyl sulfoxide (DMSO, Sigma-Aldrich, Cat. No. D2650) to a final concentration of 335 mM and stored at 4 °C.

Lipid NE synthesis

NEs compromising Miglyol®, sphingomyelin and lumichrome were formulated by the ethanol injection method previously outlined by collaborators (6). In short, Miglyol® 812 N (oil) (IOI Oleo GmbH) and sphingomyelin (surfactant) (Lipoid E SM, Lipoid GmbH) were mixed in a 10:1 ratio and dissolved in 100 µL of 100 % ethanol, with or without lumichrome. Subsequently, NEs were generated by injecting the organic phase into 1 mL of ultrapure water at RT.

Flow cytometry

Human PDAC PDX-derived cell cultures were harvested with trypsin (Corning, Cat. No. 25-052-CI), washed with 1× PBS and resuspended in Flow buffer (1× PBS, 3% FBS (v/v) and 3 mM ethylenediaminetetraacetic acid (EDTA) (v/v)) with 2 µg/mL of 4′,6-diamidino-2-phenylindole (DAPI) to differentiate dead cells. Cells were analyzed with 4-laser Attune NxT Acoustic Cytometer (Thermo Fisher Scientific, Cat. No. A24858). AF^+ populations were selected by exciting cells with 488 nm blue laser and gating the intersection with filters 530/40 (BL1) and 580/30 (BL2). Results were analyzed with FlowJo vX.0.7 software (Tree Star Inc.).

Annexin V assay

Both detached (presumably dead) and attached (presumably live) PDAC PDX-derived cells were recovered by collecting culture supernatant and harvesting attached cells after a 24 h-treatment. Cells were stained using Annexin V-CF®633 (Biotium, Cat. No. 29008) according to the manufacturer's protocol. Briefly, cells were centrifuged and cell pellets were resuspended in Binding buffer mixed with Annexin V-CF®633 on a 20:1 ratio. Incubation took place protected from light for 20 min at RT. After incubation, samples were resuspended in Flow buffer with 2 µg/mL DAPI to be analyzed by flow cytometry. Cells were plotted with filters 440/50 (VL1) and 670/14 (RL1). Quadrant gating, performed within whole or AF^+ populations, was used to distinguish viable cells (Annexin V^-DAPI^-), early apoptotic cells (Annexin V^+DAPI^-), late apoptotic cells (Annexin V^+DAPI^+) and dead cells (Annexin V^-DAPI^+).

Colony formation assay

PDAC PDX-derived cell cultures treated for 24 h were washed with 1× PBS and cells were harvested, counted and plated at a low density of 1×10^3 cells/well in 24-well cell culture plates (Thermo Fisher Scientific, Cat. No. 142475) and further treated to assess their clonogenic potential. After 7 days of growth, colonies were washed, fixed for 10 min with 4 % paraformaldehyde, stained with a 2 % (w/v) crystal violet solution for 1 h and subsequently washed with ultrapure water. Remaining dry crystal violet was dissolved in 1 % sodium dodecyl sulfate (SDS, Sigma, Cat. No. L4509) before

measuring its absorbance at 562 nm (Abs562 nm) with Agilent BioTek Synergy HT Microplate Reader (Agilent BioTek)

Cell metabolism assessment

Oxygen consumption rate (OCR) and ATP production were measured with Seahorse XFp HS Mini Analyzer (Agilent Technologies, Cat. No. S7802A). PDAC PDX-derived 7-day-old spheres were harvested with a 20 min trypsin incubation at 37 °C, plated in Seahorse XFp cell culture Miniplates (Agilent Technologies, Cat. No. 103722-100) at a density of 1.5×10^4 cells/ well and incubated overnight. Cells were then treated for 24 h. After that, cells were incubated in Seahorse XF DMEM media (Agilent Technologies, Cat. No. 103575-100) supplemented with 2 mM glutamine (Agilent Technologies, Cat. No. 103579-100), 10 mM glucose (Agilent Technologies, Cat. No. 103577-100) and 1 mM pyruvate (Agilent Technologies, Cat. No. 103578-100) for 1 h, following manufacturer's instructions. Raw data from the Analyzer were normalized to total protein (µg) using Pierce™ BCA protein assay kit (Thermo Fisher Scientific, Cat. No. 23225) following manufacturer's protocol.

Blue light and gemcitabine treatment regimen

PDAC PDX-derived nearly confluent cell cultures treated with or without NEs, empty or loaded with lumichrome, and 10 µg/mL gemcitabine for 24 h were washed with 1× PBS and exposed to a blue LED strip (460-465 nm, JOYLIT, SMD 5050, 12 V and 3.5 A input, 12 V and 2.2 A output) for 2 h at RT. The irradiation of cells was carried out in PBS. Another 1× PBS wash was performed before further treating with or without 10 µg/mL gemcitabine for 24 h.

Statistical analyses

Statistical analyses were performed using GraphPad Prism v8.0.1 software (GraphPad Software Inc.). The Shapiro–Wilk test was used to assess whether the data followed a normal distribution. When normality was confirmed, one- or two-way ANOVA and Tukey's multiple comparison test were applied as comparisons were always between three or more groups.

Results

Lumichrome NEs reduce cell AF without inducing global toxicity *in vitro*

Lumichrome NEs were successfully generated using the ethanol injection method, yielding stable NEs composed of Miglyol® (as the oil phase) and sphingomyelin (as the surfactant) at a 10:1 ratio (Fig. 1A). Flow cytometric analyses of nearly confluent A6L, 185 and 185 scd cell cultures after a 24 h-treatment with lumichrome, free or loaded in NEs, showed a marked reduction in the percentage of AF^+ cells after lumichrome administration (Fig. 1B, C).

Lumichrome NEs limit OXPHOS and ATP production in CSC-enriched PDAC cell cultures *in vitro*

Following the hypothesis of this study, to evaluate whether administration of lumichrome affects CSC respiratory metabolism, various mitochondrial functional parameters were analyzed in sphere-derived 185 scd cells using the Seahorse XF HS Mini Analyzer (Agilent Technologies). After a 24 h-treatment with lumichrome NEs,

basal and maximal respiration and ATP production rates decreased significantly (Fig. 2A). These data indicate that lumichrome administration may impair mitochondrial respiration in CSC-enriched PDAC PDX-derived cell cultures *in vitro*, supporting a specific effect towards CSC metabolism.

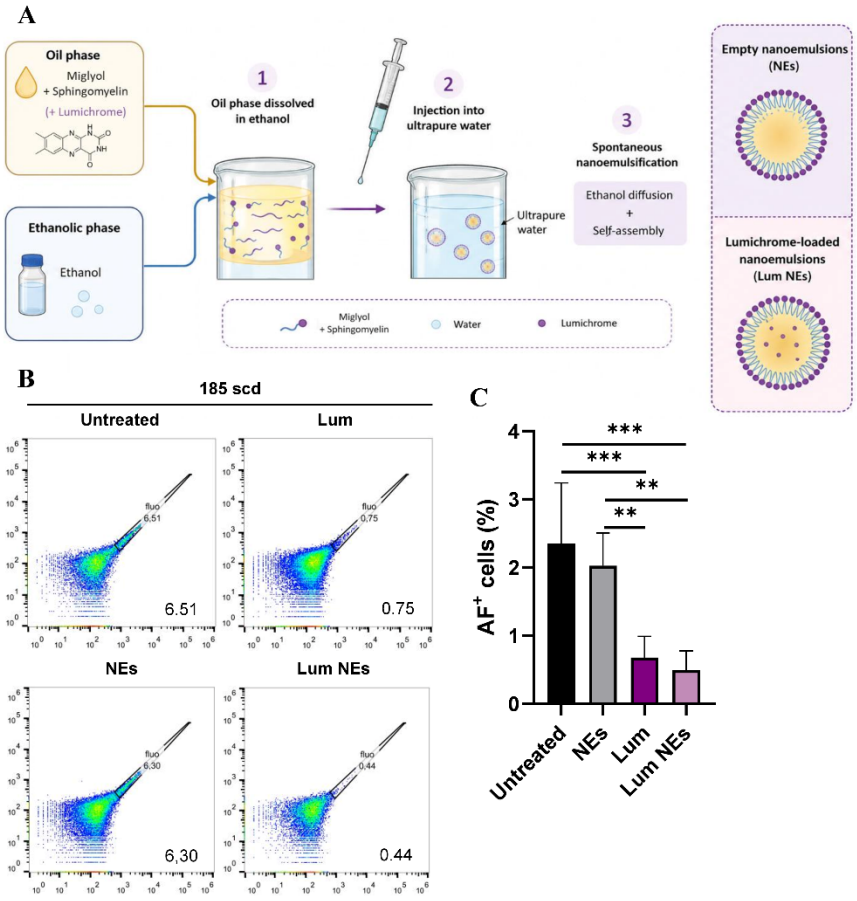

Figure 1. Outline of nanosystem development and quantification of the effect of lumichrome addition on autofluorescence and cell viability. **A**: schematic representation of the nanoemulsion (NE) synthesis protocol using the ethanol injection method. Briefly, Miglyol® (oil) and sphingomyelin (surfactant) were mixed in a 10:1 ratio in an ethanolic organic phase, with or without the addition of lumichrome. Subsequently, this mixture was injected in ultrapure water to spontaneously generate NEs. **B**: flow cytometric analyses of PDAC PDX-derived 185 scd cell cultures treated with or without free 200 µM lumichrome (Lum), empty NEs or 200 µM lumichrome-loaded NEs (Lum NEs). Autofluorescent cells (fluo) were excited with a 488 nm blue laser and selected as the intersection with filters 530/40 (BL1) and 580/30 (BL2). Percentage of autofluorescent cells is shown for each dot plot. **C**: bar graph showing differences in autofluorescent (AF^+) populations across indicated treatments. N = 3, five independent experiments. Statistical significance was assessed by a one-way ANOVA followed by a post-hoc Tukey's multiple comparison test (* = $p<0.05$, ** = $p<0.01$, *** = $p<0.001$).

Lumichrome NEs may be inducing apoptosis specifically in CSCs *in vitro*

To assess whether the observed OXPHOS impairment led CSCs to death, we studied the apoptotic status of A6L and 185 scd PDAC PDX-derived cell cultures via an Annexin

V assay after a 24-h treatment with lumichrome NEs. Using phosphatidylserine-binding protein Annexin V and DAPI, this flow cytometry-based assay allows for the detection and stratification of apoptosis based on the percentage of cells that have flipped phosphatidylserine to their outer membrane and/or have intracellular DAPI. Cells were analyzed either as total populations or after stratification according to AF. While no drastic changes were detected in the apoptotic status of the bulk cell populations, a higher percentage of late-apoptotic cells was found within the AF^+ (CSC) subpopulations after lumichrome treatment (Fig. 2B). These findings may indicate that lumichrome NEs can trigger apoptosis in CSCs from PDAC PDX-derived A6L and 185 scd cells under the tested conditions.

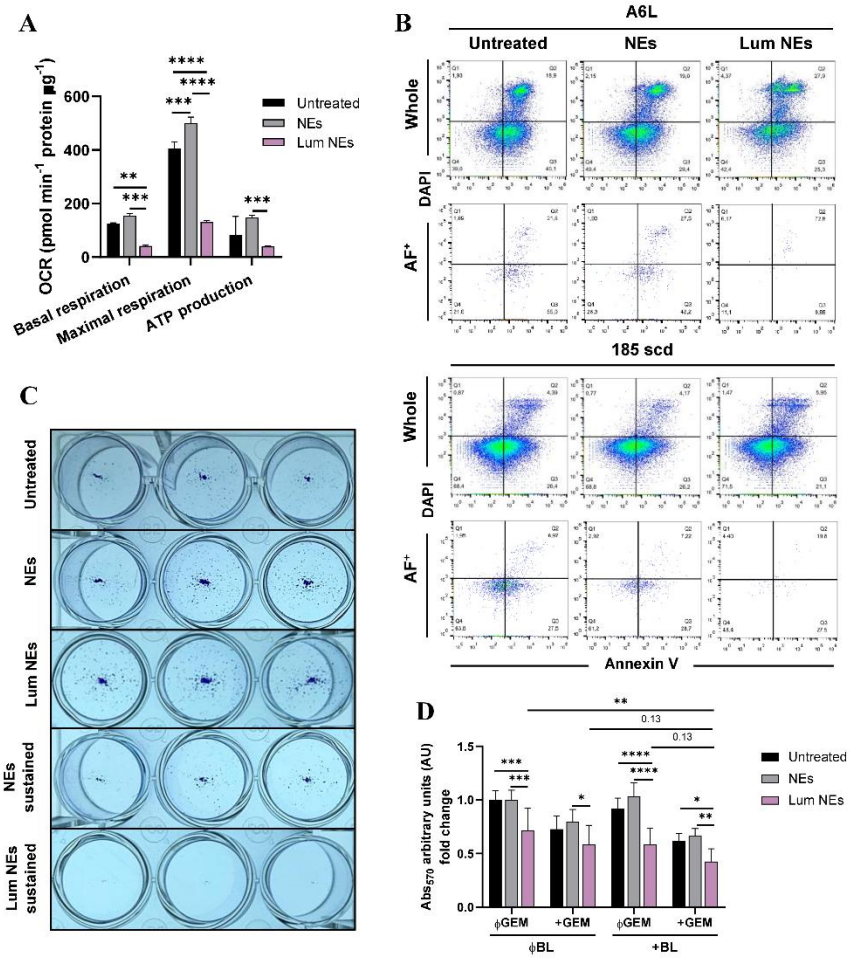

Figure 2. Integrated effects of lumichrome on apoptosis, colony formation capacity and metabolic activity of primary PDAC cultures *in vitro*. **A**: mean ± standard deviation of measured and calculated mitochondrial function parameters for sphere-enriched 185 scd cells treated with empty NEs (NEs) or 200 µM lumichrome-loaded NEs (Lum NEs) as indicated. Graphs shown are representative of one primary PDAC PDX-derived in vitro cell culture (N = 1) with three readings, normalized to total protein content using a BCA kit (measured as BCA $Abs_{562\ nm}$). **B**: representative dot plots from flow cytometric analyses of Annexin V and DAPI staining illustrating the apoptotic status in A6L and 185 scd cells, ungated (Whole) or in autofluorescent (AF^+) populations, treated with or without empty NEs (NEs) or 200 µM lumichrome-loaded NEs (Lum NEs). Quadrant gating distinguishes viable cells (Annexin V DAPI), early apoptotic cells (Annexin V^+DAPI^-), late apoptotic cells (Annexin V^-DAPI^-) and necrotic cells

(Annexin V$^-$DAPI$^+$). **C**: evaluation of cell self-renewal and proliferation via a colony formation assay. Representative images of macroscopic colonies photographed under the indicated conditions after treating 185 cells with NEs or 200 µM lumichrome-loaded NEs as indicated. Cells that had been treated for 24 h with shown conditions were washed before being grown for 7 additional days in colony-promoting conditions with no further treatment (NEs, Lum NEs) or retreated with NEs (NEs sustained) or 200 µM lumichrome-loaded NEs (Lum NEs sustained) for those 7 days. **D**: bar graph showing the number of living 185 cells, detected by MTT assay, that had been treated with or without empty nanoemulsions (NEs) or 200 µM lumichrome-loaded NEs (Lum NEs 200 µM) and with or without 10 µg/mL gemcitabine (Gem) for 24 h, exposed to an LED source of blue light (BL, 460-465 nm) for 2 h and retreated with 10 µg/mL gemcitabine for 24 h. Data from two independent experiments. Statistical significance was assessed by a two-way ANOVA followed by a post-hoc Tukey's multiple comparison test (* = $p<0.05$, ** = $p<0.01$, *** = $p<0.001$, **** = $p<0.0001$).

Sustained lumichrome treatment impairs functional stemness *in vitro*

Next, to study if the observed outcomes of lumichrome administration translated into a sustained impaired cancer stem cell function, the clonogenic capacity of 185 cells was assessed by evaluating proliferation from a very low initial cell seeding density through a colony formation assay (CFA). Cells were treated with empty or lumichrome NEs for 24 h, washed and allowed to grow for 7 additional days under colony-promoting conditions, with or without sustained empty or lumichrome NEs treatment. Although no changes in 185 colony-forming capacity were observed after a single 24 h-treatment with lumichrome NEs, maintaining the treatment during the whole duration of the assay led to the elimination of CSCs capable of forming colonies (Fig. 2C). Taken together, these results suggest that sustained lumichrome treatment (i.e., sustained decreased AF) blocks functional stemness properties of the tested PDAC PDX-derived cells.

Blue light exposure enhances the effects of lumichrome administration

Building on the effects of lumichrome treatment on CSCs, we investigated whether blue light exposure could further potentiate them. Accordingly, 185 cells were treated with lumichrome NEs and gemcitabine for 24 h, exposed to a blue LED source (460-465 nm) for 2 h, and further treated with gemcitabine for 24 hours. The observed trend suggests that the combination of lumichrome and blue light enhances the effectiveness of PDAC's standard-of-care chemotherapy, gemcitabine, as the triple-therapy regimen led to the most powerful blocking of tumor cell growth across all conditions (Fig. 2D).

Discussion

PDAC remains one of the most lethal human malignancies. Its characteristic therapeutic resistance and high rate of relapse is partly attributed to a small stem-like subpopulation of CSCs which sustain tumor growth, evade cytotoxic therapies and display remarkable metabolic plasticity. In PDAC, CSCs are distinguished by their reliance on mitochondrial OXPHOS and by their capacity to accumulate riboflavin within specialized intracellular vesicles, causing a characteristic intrinsic AF. In this context, the present study explored a "Trojan Horse" strategy in which riboflavin analog lumichrome is preferentially internalized by CSCs through their flavin-handling machinery, thereby perturbing mitochondrial metabolism from within. Our results

suggest that Miglyol®-based NEs loaded with lumichrome can can be taken up by CSC, readily alter CSC AF by displacing riboflavin and affect mitochondrial respiration.

Lumichrome NEs treatment indeed led to an effective and rapid decrease in cell AF, as it had been noted for free-form lumichrome. Consistent with the hypothesis that displacement of the CSC riboflavin reservoir by lumichrome could affect OXPHOS CSC metabolism, we demonstrated that lumichrome-loaded NEs significantly reduced both mitochondrial respiration and ATP production in a CSC-enriched PDAC PDX-derived culture *in vitro*. This could explain the fact that Annexin V assays pointed to a greater increase in late apoptosis within the AF^+ (CSC) subpopulations compared to the bulk tumor cells after treatment with lumichrome NEs, as our approach would be targeting a specific CSC population. This hypothesis requires deeper investigation through repetition with other PDAC PDX-derived cell models. Moreover, sustained treatment with lumichrome NEs might provide a more robust effect. This may explain why 185 scd cells suffered a smaller effect compared to A6L, as 185 scd are enriched in AF^+, likely requiring a more agressive treatment to effectively target the entire AF^+ CSC population.

Ultimately, functional stemness assays should provide a more reliable assessment of long-term stemness alterations mediated by lumichrome. In this study, the CFA performed revealed persistent reductions in clonogenic capacity not after a single 24 h-lumichrome NEs treatment prior to sphere or colony seeding, but with sustained treatment during the whole duration of the assay. We wanted to see if the combination of blue light exposure and lumichrome NEs could make up for a shorter lumichrome treatment, as the photoactivation of riboflavin and blue-absorbing related flavins has been shown to exacerbate mitochondrial stress and redox imbalance, particularly in cells with high mitochondrial reliance (e.g., PDAC CSCs) [7]. Indeed, the combined blue light and lumichrome NEs regimen held a greater effect on tumor cell growth over lumichrome NEs alone. This effect seems to be stronger when combined with gemcitabine. The rapid loss of AF and subsequent metabolic priming of PDAC CSCs observed after lumichrome addition and blue light exposure suggests that, through this combination, we may be able to sensitize PDAC CSC populations to chemotherapeutic stress (e.g. gemcitabine).

Although not part of this project, the potential extrapolation of this work to *in vivo* preclinical models is needed. Even if the blue light strategy explored here relies on external illumination rather than autonomous light generation, the successful *in vivo* implementation of self-illuminating nanosystems by our group supports the feasibility of exploiting flavin photoreactivity in deep-seated pancreatic tumors [8]. Besides, a comprehensive physicochemical characterization of lumichrome NEs is necessary. Parameters such as encapsulation efficiency, drug loading capacity, particle size distribution, polydispersity index, surface charge, and formulation stability over time were not exhaustively assessed in this study and will be essential for the rigorous interpretation of biological effects, especially when considering future *in vivo* applications.

Conclusion

In conclusion, this study identifies a metabolic vulnerability of PDAC CSCs and proposes to target it using lumichrome NEs. We demonstrate that these formulations are effectively internalized by CSCs, displace intracellular riboflavin (reducing AF) and impair mitochondrial respiration and ATP production, leading to preferential induction of apoptosis within CSC-enriched (AF^+) populations. Functionally, sustained exposure to lumichrome NEs reduces clonogenic capacity, while combination of lumichrome NEs with blue light enhances metabolic stress and potentiates antitumor effects *in vitro*, particularly in combination with chemotherapy. Together, these findings support lumichrome-loaded Miglyol® NEs as a promising approach to selectively target PDAC CSC metabolism and sensitize these resistant populations to conventional antitumoral treatment.

Acknowledgement

This research received no specific grant from any funding agency.

References

[1] Sohal DPS, Kennedy EB, Cinar P, Conroy T, Copur MS, et al. Metastatic pancreatic cancer: ASCO guideline update. J Clin Oncol 2020; 38(27): 3217–3230. doi: 10.1200/JCO.20.01364

[2] Walcher L, Kistenmacher AK, Suo H, Kitte R, Dluczek S, et al. Cancer stem cells—origins and biomarkers: perspectives for targeted personalized therapies. Front Immunol 2020; 11: 1400. doi: 10.3389/fimmu.2020.01280

[3] Miranda-Lorenzo I, Dorado J, Lonardo E, Alcala S, Serrano AG, et al. Intracellular autofluorescence: a biomarker for epithelial cancer stem cells. Nat Methods 2014; 11: 1161–1169. doi: 10.1038/nmeth.3112

[4] Sancho P, Burgos-Ramos E, Tavera A, Bou Kheir T, Jagust P, et al. MYC/PGC-1α balance determines the metabolic phenotype and plasticity of pancreatic cancer stem cells. Cell Metab 2015; 22(4): 590–605. doi: 10.1016/j.cmet.2015.08.015

[5] Sturm S, Niegisch G, Windolf J, Suschek CV. Exposure of bladder cancer cells to blue light (λ = 453 nm) in the presence of riboflavin synergistically enhances the cytotoxic efficiency of gemcitabine. Int J Mol Sci 2024; 25(9): 4872. doi: 10.3390/ijms25094868

[6] Bouzo BL, Lores S, Jatal R, Alijas S, Alonso MJ, et al. Sphingomyelin nanosystems loaded with uroguanylin and etoposide for treating metastatic colorectal cancer. Sci Rep 2021; 11: 1–12. Doi: 10.1038/s41598-021-96578-z

[7] Chen PJ, Hsieh JP, Chang HT, Chen YL, Chuang SF. Use of photoreactive riboflavin and blue light irradiation in improving dentin bonding—multifaceted evaluation. J Funct Biomater 2025; 16(1): 11. doi: 10.3390/jfb16010011

[8] Abal-Sanisidro M, Ruiz-Cañas L, Batres-Ramos S, Blanco MG, García-Bermejo ML, et al. Evaluation of self-illuminating nanoconjugates against pancreatic ductal adenocarcinoma. Int J Nanomedicine 2026; 21: 545161. doi: 10.2147/IJN.S545161

EXPERIMENTAL EVALUATION OF INTRACELLULAR EFFECTS OF NON-UNIFORM IRRADIATION FOR IMPROVING THE RADIOBIOLOGICAL MONITORING OF RADIOTHERAPEUTIC EXPOSURE

Lada Naimushina[1], Matus Durdik[2], Pavol Kosik[2], Volodymyr Vinnikov[2]

[1]Department of Molecular Biology, Faculty of Natural Sciences, Comenius University Bratislava, Bratislava, Slovak Republic
[2]Department of Radiobiology, Institute of Cancer Research, Biomedical Research Center, v.v.i., Slovak Academy of Science, Bratislava, Slovak Republic

Introduction

Nowadays, there is a high demand in radiation oncology for robust biomarkers to assess intrinsic radiosensitivity in patients undergoing radiotherapy. A promising approach in this area may be to irradiate patients' cells ex vivo [1 – 3]. In our view, this strategy can be improved by simulating partial exposure in the experiment. However, an accurate measurement of a non-uniform irradiation in terms of "dose – volume" using any stand-alone radiation biomarker is very challenging [4].

To address this limitation, this study explores a multiparametric approach combining DNA damage response, apoptosis, and chromosomal aberrations assays in human blood lymphocytes. We hypothesized that such a biomarker panel, if applied to an in vitro model of non-uniform irradiation, could improve the detection and quantification of heterogeneous irradiation and provide insight into individual cellular radiosensitivity.

Materials and methods

Blood samples collection.
The study was conducted in accordance with the ethical standards of the Declaration of Helsinki and with the informed consent of the participants. Blood samples were collected by venipuncture in Vacutainers containing sodium heparin anticoagulant from 4 healthy, non-smoking donors: 2 males (38 and 52 years old) and 2 females (30 years old each).

Irradiation of cells.
Peripheral blood mononuclear cells (PBMCs) were isolated from whole blood immediately after obtaining samples and exposed ex vivo to 2.73 Gy of 6 MV linac photons, which is the typical radiation dose-per-fraction used for radiotherapy of breast cancer. Irradiated samples were accompanied by respective sham-irradiated controls. Samples were transferred into 2 ml plastic cryovial tubes, which were inserted into 15 ml centrifuge tubes. The latter were filled with water of ambient temperature and placed

into the improvised water-filled phantom for irradiation. During transportation and irradiation, the tubes were kept in thermostatic conditions at about +35-37 °C for apoptosis and cytogenetic assays and about 0 °C for the DNA damage response assay. Partial body irradiation (PBI) was simulated by mixing irradiated and unirradiated cells in a 1:1 ratio. DNA damage response (γ-H2AX foci) and radiation-induced lymphocyte apoptosis (RILA, Annexin V assay) were measured using flow cytometry. The number of cells undergoing apoptosis was assessed 30 min, 24 h, and 48 h after irradiation, while timepoints for γ-H2AX were 30 min and 24 h. The samples stained with respective fluorescent markers were analyzed on the FACSCanto II cytometer (BD Biosciences, Franklin Lakes, New Jersey, USA).

Chromosome aberrations.

Chromosome aberrations, namely dicentrics and centric rings (Dic+CR), were analyzed using the standard protocol [5]. After irradiation, samples were placed in an incubator at a temperature +37°C; 5% CO2; humidified atmosphere, for 2 h to allow completing of DNA repair. Subsequently, lymphocyte cultures were initiated by phytohemagglutinin. Colcemid was used for mitotic arrest. After 48-50 h culturing cells were fixed, dropped onto microscopy slides, and stained by the Fluorescence-plus-Giemsa (FPG) method. Slides were scanned on the automated computerized microscopy system Metafer 5_v.3.11.7 (MetaSystems, Altlussheim, Germany) mounted on the AxioImager.Z2 microscope (Carl Zeiss, Germany). In the TBI scenario, 300 metaphases were analyzed, in the PBI scenario 500 metaphases, and in the sham-irradiated controls (0 Gy) 1000 metaphases. A metaphase was accepted for analysis only if it represented the first mitosis, distinguished by a uniform dark FPG-staining of both chromatids.

Results

The effects of radiation exposure are presented in the figures. 1, 2, and 3. The averaged values of measured parameters are given in Table 1. At 30 min post-exposure in TBI scenario, a massive accumulation of γ-H2AX-positive cells was observed. In PBI scenario a distinctive double-peak distribution occurred showing proportions of 50% irradiated and 50% non-irradiated fraction (Fig. 1). At 24 h after irradiation the DNA repair process was mostly completed, and PBI scenario became indistinguishable from TBI. However, enough γ-H2AX foci, representing unrepaired DNA damage, were still detectable at 24 h, providing a statistical increase above control, which was proportional to the irradiated fraction.

The kinetics of RILA comprised a gradual time-dependent increase of the frequency of Annexin-positive cells (Fig. 2). However, at 24 h and 48 h this end-point became manifested much clearer in irradiated samples. At both time points the accumulation of RILA in TBI was more pronounced compared to that in PBI. However, the frequency of dead cells in PBI scenario after subtracting the control level ($PBI_{induced}$) appeared to be systematically higher than an expected half of the induced yield in TBI (1/2 $TBI_{induced}$).

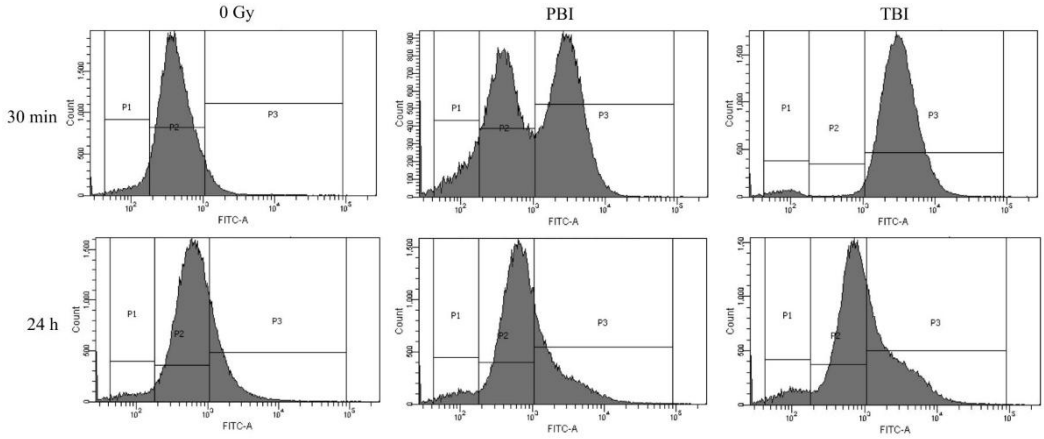

Figure 1. γ-H2AX intensity measured by flow cytometry. P1 – debris, dead cells, excluded from analysis; P2 – γ-H2AX-negative cells (no DNA DSB); P3 – γ-H2AX-positive cells (the presence of γ-H2AX foci indicates the ongoing DNA repair process); FITC-A – channel, displaying the γ-H2AX signal, reflecting the presence of DSB; Count – number of detected signals; 0 Gy – the unirradiated control; PBI – partial body irradiation; TBI – total body irradiation.

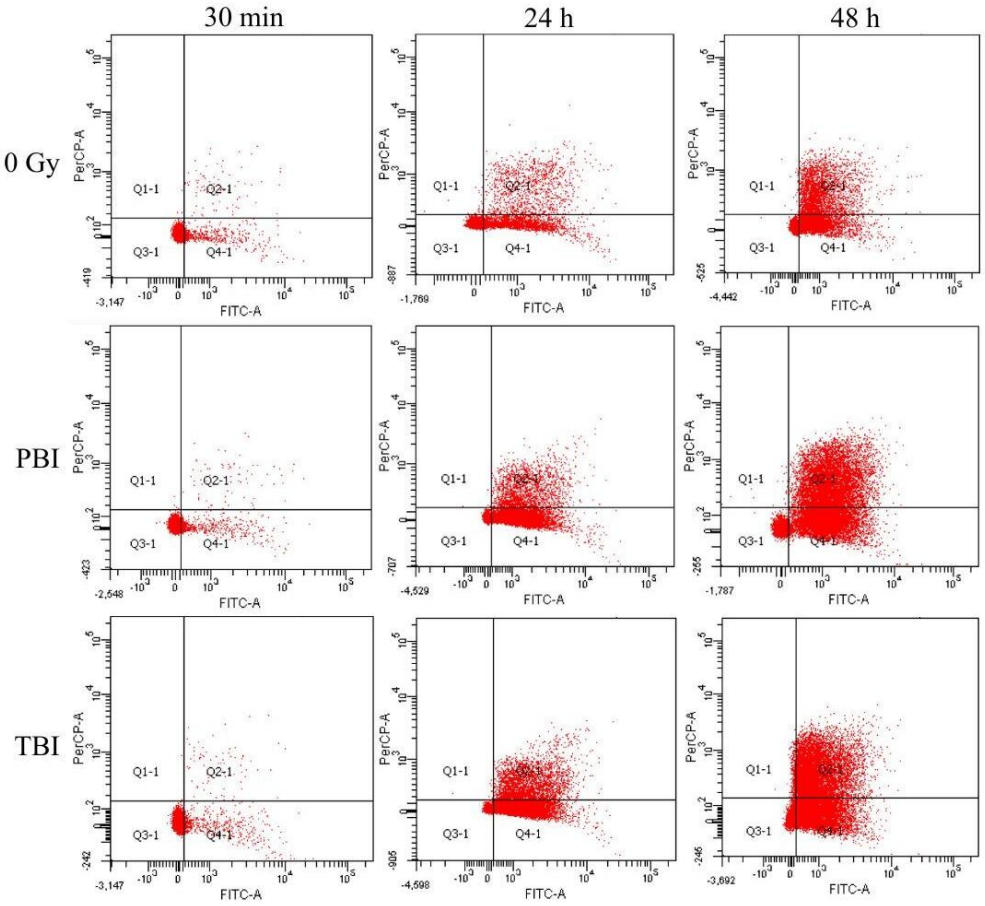

Figure 2. Cell distribution according to Annexin V staining measured by flow cytometry. Q1-1 – primarily necrotic cells; Q2-1 – late apoptotic cells; Q3-1 – viable cells; Q4-1 – early apoptotic cells; PerCP-A – channel, measuring the fluorescence of 7-AAD; FITC-A – channel, representing the fluorescence of Annexin V-FITC; 0 Gy – the unirradiated control; PBI – partial body irradiation; TBI – total body irradiation.

Cytogenetic damage also demonstrated an overall positive correlation with the size of irradiated fraction, however this parameter had mechanistically more complex dependence on the radiation dose and exposed volume because of the overlap between ChA formation and interphase cell death, which are mutually independent events (Fig. 3). In cells of each donor the distribution of ChA per cell followed a Poisson distribution at 0 Gy and in the TBI scenario. Meanwhile, in the PBI simulation, the Dic+CR per cell distribution showed significant overdispersion compared to Poisson statistics (in the pooled dataset $\sigma 2/Y = 1.3652$; u-value = 11.56 > 1.96), pointing at the non-uniform character of radiation exposure. Interphase cell death, calculated from cytogenetic parameters, was about 44 %.

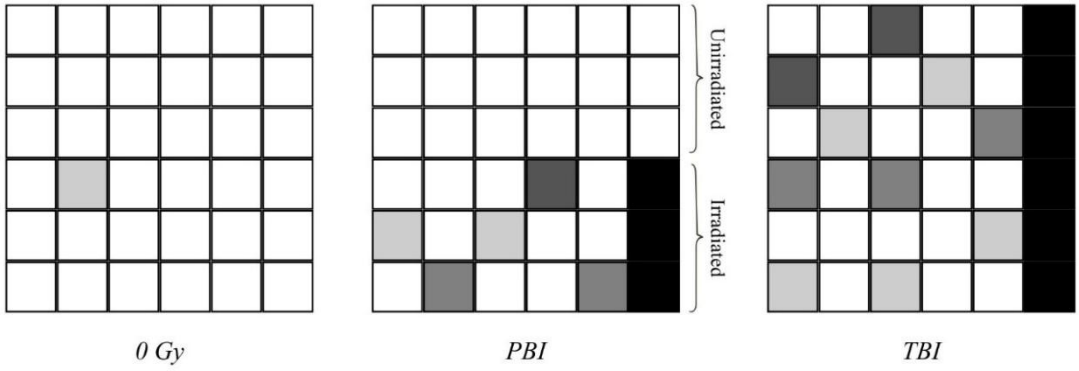

$$Y_{PBI} = \frac{Y_{TBI}\ x\ IF\ x\ ICS}{(1-IF)+IF\ x\ ICS} \qquad ICD = 1 - ICS = [1 - \frac{Y_{PBI}}{Y_{TBI} - Y_{PBI}}]\ \text{x}\ 100\%$$

Fig. 3. Schematic distribution of Dic+CR in different irradiation scenarios. Dic+CR – Dicentrics plus Centric Rings; White squares – cells with no Dic+CR; Light-gray squares – cells with 1 Dic+CR; Medium-grey squares – cells with 2 Dic+CR; Dark-grey squares – cells with ≥3 Dic+CR;
Black squares – cells, which underwent interphase death; 0 Gy – the unirradiated control; PBI – partial body irradiation; TBI – total body irradiation; Y – aberration yield; IF – irradiated fraction; ICS – interphase cell survival; ICD – interphase cell death.

Table 1. Mean yields of radiation biomarkers in different exposure scenarios.

End-point	**γ-H2AX± SE, %**		**RILA± SE, %**		**Dic+CR per 100 cells**	
Scenario	**30 min**	**24 h**	**24 h**	**48 h**	**Y_{dr}± SE**	**Y_{cdr}± SE**
0 Gy	2.15±1.25	9.13±2.22	20.00±2.50	39.45±0.80	0.10±0.05	0.10±0.05
PBI	50.00±3.04	15.38±2.07	51.65±4.42	76.38±2.68	21.80±1.22	16.60±0.83
TBI	93.10±2.25	22.13±3.22	70.10±3.27	88.25±4.40	60.42±2.23	46.17±1.44
PBI_{ind}	47.85±3.31	6.25±0.63	31.65±2.10	36.93±2.32	21.70±1.22	16.50±0.83
½ TBI_{ind}	45.48±1.67	6.50±0.74	25.05±0.58	24.40±2.06	30.16±1.58	23.03±1.72
TBI_{ind}	90.95±3.35	13.00±3.93	50.10±1.16	48.80±4.11	60.32±2.23	46.07±1.44

SE – standard error of the mean; PBI_{ind} – obtained estimates with subtracting background level (0 Gy); TBI_{ind} – obtained estimates with subtracting background level (0 Gy); ½ TBI_{ind} – expected estimates as half of TBI_{ind}.

Discussion

Radiation exposure to a dose of 2.73 Gy with 6 MV linear accelerator X-ray photons leads to a significant increase in cellular radiomarkers in PBMC, including the accumulation of γ-H2AX foci, induction of apoptosis, and the formation of chromosomal aberrations.

However, measuring DNA damage response using γ-H2AX foci has limited applicability over time due to a decrease in foci intensity to below control levels 24 hours after irradiation under both uniform and non-uniform irradiation conditions. Futhermore, RILA assay cannot be used as a standalone tes due to its unapplicability to represent a partial exposure model but can provide an additional, supporting estimate of the proportion of surviving cells.

Irradiation-induced cell death, which determines the biological estimate of the proportion of irradiated cells, increased across endpoints in the following order: interphase cell death as determined by cytogenetic analysis < G_0 apoptosis after uniform irradiation < G_0 apoptosis in non-uniformly irradiated cell populations. The difference between cytogenetic and RILA results can be explained by methodological peculiarities of the dicentric and Annexin V assays: cells for cytogenetic analysis were stimulated to proliferate, and they could have passed through the interphase to mitosis with two checkpoints for DNA repair, while cells in the RILA assay remained in G_0 phase. The phenomenon of higher death processes in the PBI scenario by apoptosis probably could be resultant from a bystander effect, when irradiated cells excrete soluble signals reaching non-irradiated cells and initiating the apoptotic process in the latter [6].

Conclusion

The combination of three endpoints provides a more accurate and reliable quantitative assessment of partial radiation exposure compared to any assay taken alone. The results obtained can make a valuable contribution to the theoretical foundations of radiobiology and provide a better understanding of the mechanisms underlying radiation-induced effects in normal human tissue cells. Furthermore, the obtained results can improve existing methodological approaches and assist in the development of practical radiobiological test-systems for radiation oncology and radiation protection.

Acknowledgement

This research work was supported by the EU NextGenerationEU through the Recovery and Resilience Plan for Slovakia under the project No. [09I03-03-V01-00068].

References

[1] Vinnikov V, Hande MP, Wilkins R, Wojcik A, Zubizarreta E et al. Prediction of the Acute or Late Radiation Toxicity Effects in Radiotherapy Patients Using Ex Vivo Induced Biodosimetric Markers: A Review. J Pers Med 2020; 10(4): 285. doi: 10.3390/jpm10040285

[2] Azria D, Haviland JS, Brengues M, Griffin C, Moquet J et al. Radiation-induced lymphocyte apoptosis and chromosomic aberrations for prediction of toxicities in patients undergoing radical radiotherapy for breast or prostate cancers. Br J Radiol 2025; 98(1170): 929–937. doi: 10.1093/bjr/tqaf056

[3] Solana-Peña Á, Pujol-Canadell M, Macià, M, Pérez EM, Linares I et al. Evaluation of predictive biomarkers for late radiation toxicity in breast cancer patients. Sci Rep 2026; 16(1): 1366. doi: 10.1038/s41598-025-31033-x
[4] Vinnikov VA, Ainsbury EA, Maznyk NA, Lloyd DC, Rothkamm K. Limitations Associated with Analysis of Cytogenetic Data for Biological Dosimetry. Radiat Res 2010; 174(4): 403. doi: 10.1667/RR2228.1
[5] International Atomic Energy Agency. Cytogenetic Dosimetry: Applications in Preparedness for and Response to Radiation Emergencies. Vienna: IAEA, 2011.
[6] Tang H, Cai L, He X, Niu Z, Huang H et al. Radiation-induced bystander effect and its clinical implications. Front Oncol 2023; 13: 1124412. doi: 10.3389/fonc.2023.1124412

HIF-1A-DEPENDENT REGULATION OF EMT UNDER HYPOXIC CONDITIONS AND ITS INHIBITION BY HYPERICIN

Michaela Tothova, Viktoria Decmanova, Peter Fedorocko

Pavol Jozef Safarik University in Kosice, Faculty of Science, Institute of Biological and Ecological Sciences, Srobarova 2, 041 54 Kosice, Slovakia

Introduction

Epithelial–mesenchymal transition (EMT) is a biological process through which cancer cells acquire properties associated with increased migration, invasiveness, and phenotypic plasticity [1]. At the regulatory level, EMT is controlled by several families of transcription factors, mainly Snail, Zeb, and Twist, which suppress the epithelial phenotype and support the acquisition of mesenchymal features [2].

The course of EMT can be influenced by conditions of the cancer microenvironment, including hypoxia. Hypoxia is a typical feature of solid tumours and develops mainly as a result of rapid cancer cell proliferation and insufficient oxygen supply. One of the key mediators of the cellular response to hypoxia is hypoxia-inducible factor 1-alpha (HIF-1α), which is stabilized under reduced oxygen availability and regulates several processes involved in cancer progression [3]. Hypoxia has also been associated with EMT activation and may therefore contribute to a more aggressive cancer cell phenotype [4].

In this context, hypericin, a secondary metabolite derived from plants of the genus Hypericum, represents a compound of interest. Previous studies have shown that hypericin can contribute to HIF-1α degradation in hypoxic cancer cells, and this mechanism involves cathepsin B-dependent lysosomal degradation [5]. Hypericin has also been shown to act in hypoxic cancer cells and affect hypoxia-related cellular responses [6].

The aim of this study was to determine whether the effect of hypericin under hypoxic conditions is also reflected in the modulation of EMT regulation in cancer cells. We focused mainly on the classical EMT markers E-cadherin and vimentin, the EMT-associated transcription factors Snai1 and Slug, and the possible relationship between HIF-1α and Snai1 after hypericin treatment.

Materials and methods

Human cancer cell lines

A549 cells, derived from lung adenocarcinoma, and HT-29, derived from colorectal adenocarcinoma, were used in this study. Cells were cultured in RPMI-1640 medium

supplemented with 10% fetal bovine serum and an antibiotic-antimycotic mixture. Normoxic conditions were maintained at 21% O2, 5% CO2, and 37 °C. Hypoxic conditions were set to 1% O2, 5% CO2, 94% N2, and 37 °C.

Cell exposure

Hypericin was prepared as a 2 mM stock solution in sterile dimethyl sulfoxide (DMSO) and stored at -80 °C in the dark. Before treatment, hypericin was diluted in serum-containing culture medium to a final working concentration of 5 μM. All manipulations with hypericin were performed in the dark to prevent its photoactivation. In experiments focused on the mechanism of hypericin action, the cathepsin B inhibitor CA-074 was used at a concentration of 100 μM.

After seeding, cells were allowed to adhere for at least 2 hours under standard culture conditions. Subsequently, they were transferred to the hypoxic chamber or maintained under normoxic conditions. After 24 hours, hypericin was added to the cells, and samples were collected after 16 h and 40 h of hypericin treatment.

In experiments with the cathepsin B inhibitor, CA-074 was added after 16 h or 40 h of hypericin treatment, followed by an additional 6-hour incubation. Thus, the total treatment times were 22 h and 46 h after hypericin addition.

Western blot

Protein levels were analyzed by Western blot. Cells were lysed in lysis buffer supplemented with protease and phosphatase inhibitors. After determination of protein concentration, samples were separated by SDS-PAGE and transferred to a PVDF membrane. Membranes were incubated with primary and secondary antibodies, and the signal was detected by chemiluminescence. Densitometric analysis was performed using ImageLab software, and protein levels were normalized to β-actin.

Statistical analyses

The results are presented as mean values ± standard deviation (SD) from at least two independent experiments. Comparisons between two experimental groups were analyzed using an unpaired t-test. For datasets with at least three biological replicates, two-way ANOVA with Bonferroni's post hoc test was used to evaluate the effect of hypericin under normoxic and hypoxic conditions separately for each time point. Statistical significance is indicated in the legend of each figure.

Ethical approval

Ethical approval was not required, as only established commercially available human cancer cell lines were used.

Results and discussion

Hypoxia represents one of the important factors of the cancer microenvironment that can influence cancer cell plasticity and EMT regulation. In our experimental model, cultivation under hypoxic conditions increased HIF-1α levels, confirming the activation of hypoxic response in the analyzed cancer cells. Since HIF-1α is involved in the regulation of several adaptive mechanisms under reduced oxygen availability, including EMT-related processes, we further examined whether hypericin-mediated reduction of HIF-1α is reflected in EMT regulation.

The effect of hypoxia, hypericin, and their combination was first evaluated at the level of classical EMT markers. In A549 cells, E-cadherin and vimentin were analyzed, whereas in HT-29 cells only E-cadherin was evaluated, as vimentin was not detectable under these conditions. No clear changes in these markers were observed after hypoxia or hypericin treatment. Therefore, the effect of hypericin was not demonstrated at the level of classical EMT markers.

We then focused on the EMT-associated transcription factors Snai1 and Slug. Hypericin showed a more pronounced effect on Snai1 than on Slug. In A549 cells, hypoxia increased Snai1 levels, especially after 16 h, while hypericin reduced Snai1 under both normoxic and hypoxic conditions. A similar decrease in Snai1 after hypericin treatment was also observed in HT-29 cells, mainly under hypoxic conditions (Figure 1). These results suggest that hypericin affects EMT regulation rather than inducing clear changes in classical EMT markers under the conditions used.

Since Snai1 followed a similar pattern as HIF-1α, we further examined whether its reduction after hypericin treatment could be associated with HIF-1α degradation. Hypericin reduced HIF-1α levels under hypoxia, which is consistent with previous studies describing hypericin-mediated HIF-1α degradation in cancer cells [5,6]. To verify the involvement of this mechanism, we used the cathepsin B inhibitor CA-074. In A549 cells, co-treatment with CA-074 restored HIF-1α levels after hypericin treatment and was accompanied by an increase in Snai1 levels (Figure 2). These results support the conclusion that, under hypoxic conditions, Snai1 is regulated by hypericin at least partly through HIF-1α. The fact that hypericin also reduced Snai1 under normoxia suggests that other regulatory mechanisms may also contribute to this effect.

Together, these findings indicate that hypericin does not markedly affect classical EMT markers in the analyzed conditions, but it interferes with the regulatory level of EMT, mainly through Snai1. The restoration of both HIF-1α and Snai1 after cathepsin B inhibition supports the involvement of the HIF-1α/Snai1 axis in the response of hypoxic cancer cells to hypericin.

Conclusion

This study showed that hypericin reduced HIF-1α levels in hypoxic cancer cells and that this effect was accompanied by a decrease in Snai1. In contrast, changes in E-cadherin and vimentin were not clearly demonstrated.

The use of the cathepsin B inhibitor CA-074 restored both HIF-1α and Snai1 levels after hypericin treatment, supporting the conclusion that Snai1 is regulated by hypericin through HIF-1α under hypoxic conditions. These findings suggest that hypericin may affect the regulatory level of EMT in cancer cells and support further investigation of the HIF-1α/Snai1 axis in hypoxia-driven EMT regulation.

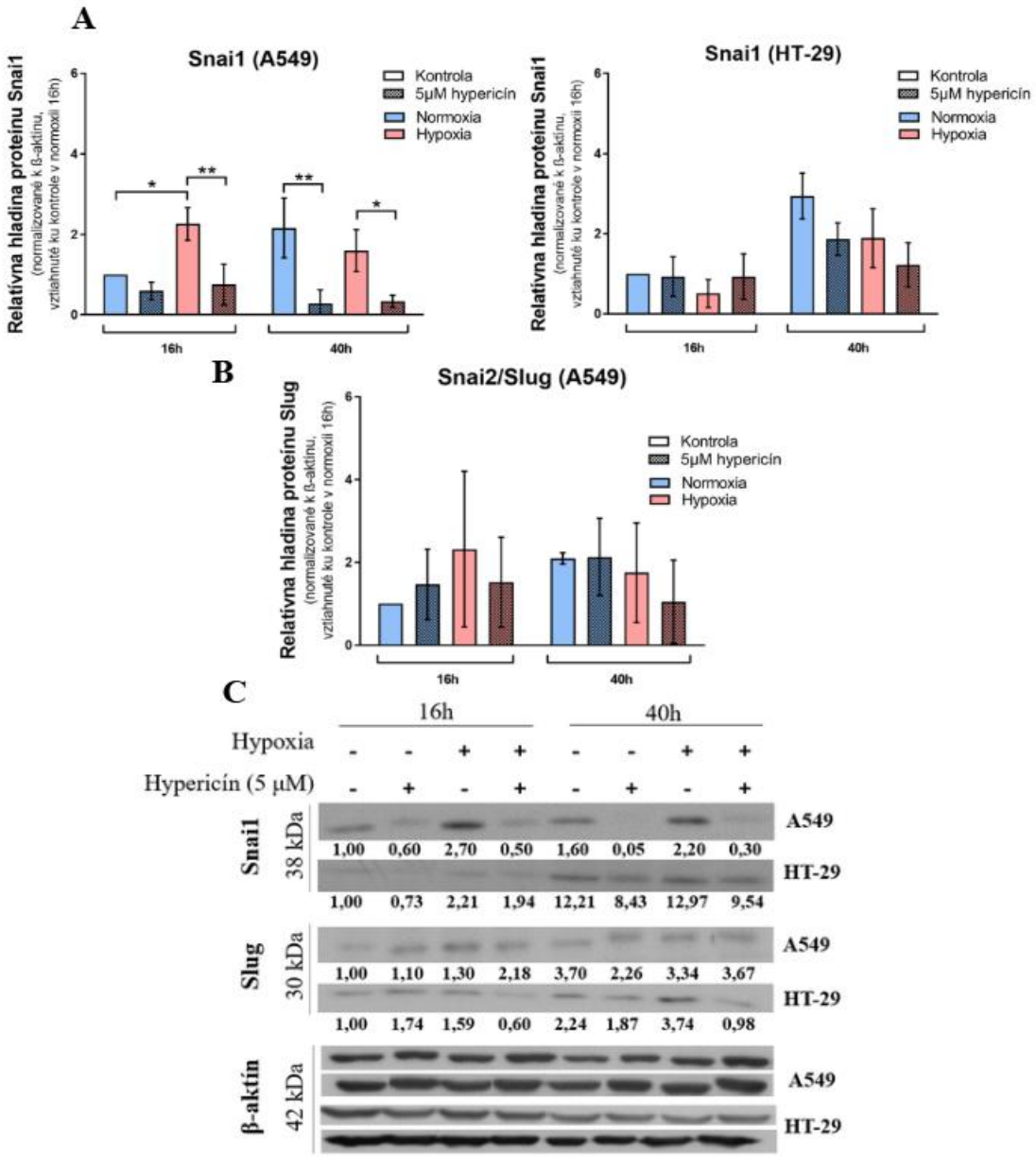

Figure 1. Effect of hypericin and/or hypoxia on EMT transcription factor protein levels. Snai1 and Slug protein levels were analyzed by Western blot after 16 and 40 hours of incubation with hypericin (5 μM) under normoxic and hypoxic conditions. (A) Relative Snai1 protein level in A549 cells (left) and HT-29 cells (right). (B) Relative Slug protein level in A549 cells. Protein levels were normalized to β-actin and related to the 16 h normoxic control. Snai1 results in A549 and HT-29 cells are presented as mean ± SD of three independent experiments and were analyzed by two-way ANOVA with Bonferroni post-hoc test (* $p < 0.05$; ** $p < 0.01$). Slug results in A549 cells are presented as mean ± SD of two independent experiments and were analyzed by t-test ($p > 0.05$). (C) Representative Western blot images of Snai1 and Slug protein levels are shown.

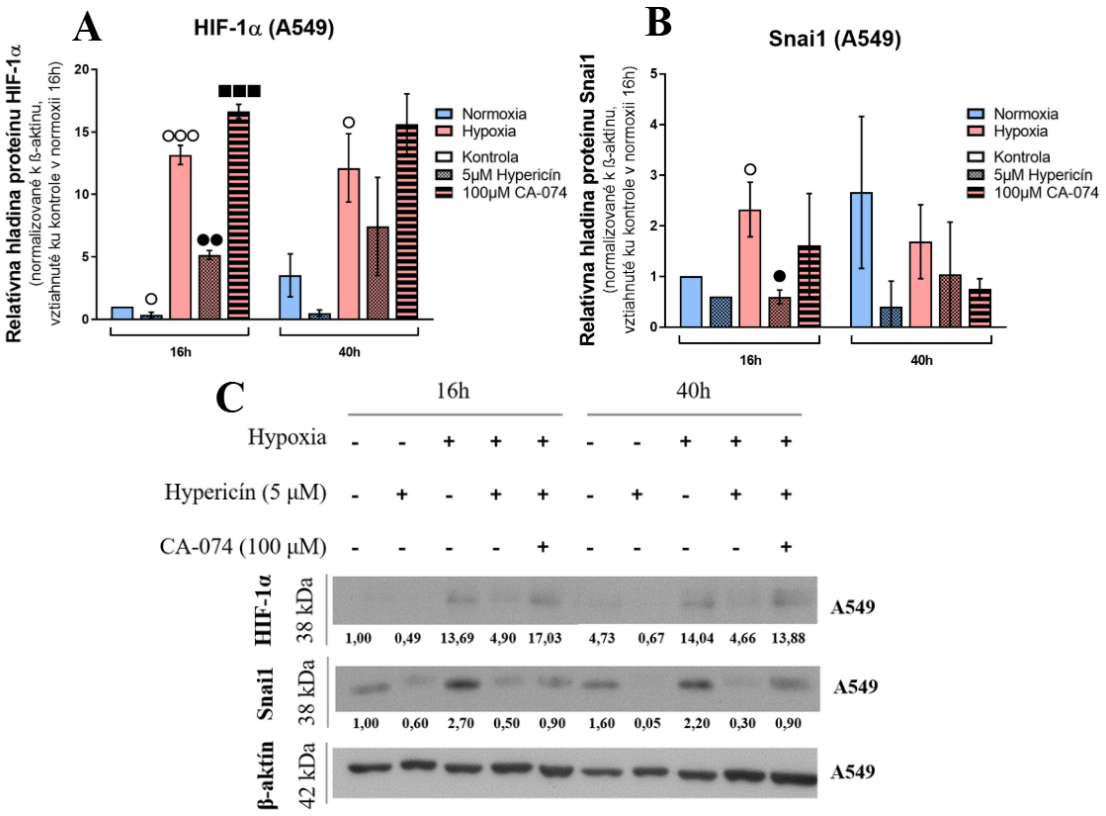

Figure 2. Effect of cathepsin B inhibition on HIF-1α and Snai1 protein levels after hypericin treatment. HIF-1α and Snai1 protein levels were analyzed by Western blot in A549 cells after 16 and 40 hours of incubation with hypericin (5 μM) and/or CA-074 (100 μM) under normoxic and hypoxic conditions. Protein levels were normalized to β-actin and related to the 16 h normoxic control. Results are presented as mean ± SD of two biological replicates. Statistical analysis was performed by t-test. Experimental groups were compared with the 16 h normoxic control (○ $p < 0.05$; ○○○ $p < 0.001$), the 16 h hypoxic control (● $p < 0.05$; ●● $p < 0.01$), or 16 h hypoxia + hypericin (■■■ $p < 0.001$). Representative Western blot images are shown.

Acknowledgement

This work was supported by the Scientific Grant Agency of the Ministry of Education, Research, Development and Youth of the Slovak Republic and the Slovak Academy of Sciences under the contract No. VEGA 1/0003/23.

References

[1] Savagner P. The epithelial–mesenchymal transition (EMT) phenomenon. Ann Oncol 2010; 21: vii89–vii92. doi: 10.1093/annonc/mdq292

[2] Debnath P, Huirem RS, Dutta P, Palchaudhuri S. Epithelial–mesenchymal transition and its transcription factors. Biosci Rep 2022; 42: BSR20211754. doi: 10.1042/BSR20211754

[3] Rankin EB, Giaccia AJ. The role of hypoxia-inducible factors in tumorigenesis. Cell Death Differ 2008; 15: 678–685. doi: 10.1038/cdd.2008.21

[4] Hapke RY, Haake SM. Hypoxia-induced epithelial to mesenchymal transition in cancer. Cancer Lett 2020; 487: 10–20. doi: 10.1016/j.canlet.2020.05.012

[5] Barliya T, Mandel M, Livnat T, Weinberger D, Lavie G. Degradation of HIF-1alpha under hypoxia combined with induction of Hsp90 polyubiquitination in cancer cells by hypericin: a unique cancer therapy. PLoS ONE 2011; 6: e22849. doi: 10.1371/journal.pone.0022849
[6] Buľková V, Vargová J, Babincák M, Jendželovský R, Zdráhal Z et al. New findings on the action of hypericin in hypoxic cancer cells with a focus on the modulation of side population cells. Biomed Pharmacother 2023; 163: 114829. doi: 10.1016/j.biopha.2023.114829

LIQUID BIOPSY – A BIOMARKER FOR THE DIAGNOSIS AND TREATMENT OF BRAIN TUMORS

Barbora Vagovicova[1], Dominika Kochanova[2], Pavol Kosik[2], Igor Belyaev[2]

[1]Comenius University Bratislava, Faculty of Natural Sciences, Department of Molecular Biology, Mlynská dolina, Ilkovičova 6, 842 15 Bratislava, Slovak Republic
[2]Department of Radiobiology, Cancer Research Institute, Biomedical Research Center of the Slovak Academy of Sciences, Bratislava, Slovak Republic

Introduction

Glioblastoma multiforme (GBM) is one of the most aggressive primary malignant brain tumors, observed mainly in older adults. In less than 3 months after diagnosis, the tumor more than doubles in volume. Due to its rapid growth over such a short period, the median overall survival of patients is less than 15 months despite treatment. [1].

Tumor tissue biopsy represents a key diagnostic step in brain tumors; however, it does not allow for repeated sampling. Liquid biopsy is an alternative non-invasive method that could contribute not only to disease detection but also to monitoring treatment response and early detection of therapy resistance [2].

Frequent regulators of gene expression are short molecules, approximately 22 nucleotides in length, known as microRNAs (miRNAs) [3]. According to available studies, miRNAs are involved in the regulation of tumor growth, exhibiting oncogenic or tumor-suppressive roles [4] and are also associated with resistance to chemotherapy and/or radiation therapy (RT).

Therefore, in our study, we used RT-qPCR to monitor the expression of candidate miRNAs in the peripheral blood of GBM patients before, during, and after treatment. As exposure to RT triggers DNA damage, we further aimed to assess patient's response to ionizing radiation (IR). We used the cytokinesis-block micronucleus (CBMN) assay to detect micronuclei (MN) in the peripheral blood of GBM patients throughout therapy. MN are small, nucleus-like structures, which form as response to DNA damage. They contain chromosomal fragments or entire chromosomes, which fail to be incorporated into the main nucleus after cell division [5;6].

The results of this study could help improve the evaluation of treatment response in GBM patients and possibly improve personalized treatment strategies.

Materials and methods

Design of the study

Peripheral blood samples of 14 patients with GBM (35 – 86 years old, mean age 59,4) and 9 healthy controls (28 – 68 years old, mean age 50,2) were collected by qualified clinicians. All patients received standardized concomitant chemotherapy with temozolomide (TMZ) and RT according to the Stupp protocol. Patient samples were collected at four subsequent stages of therapy: i) diagnosis, ii) first stage therapy (one fraction of chemo-radiotherapy, 2 Gy dosage), iii) second stage therapy (six fractions of therapy, 12 Gy dosage), and iV) at the end of therapy (60 Gy dosage). Participants were separated into two cohorts; miRNA expression analysis and MN analysis. The selected miRNAs analyzed in this study were miR-10, miR-191, miR-195, miR-20, miR-21, miR-221, miR-223, miR-34 and miR-590.

MicroRNA isolation

In case of miRNA analysis, plasma was separated by centrifugation and pelet was suspended in RBC lysis buffer. After erythrocyte lysis, the leukocyte-enriched pellet was resuspended in 1,2 ml RNazol® RT and RNA was stabilized with 480 µl DEPC-treated water and stored at -80˚C. Frozen samples were thawed and treated with 3 µl 4-bromoanisole (BAN). Total RNA isolation was performed using 100% isopropanol precipitation and twice 75% ethanol washing at 1:1 ratio. Extracted total RNA was resuspended in 30 µl DEPC-treated water and stored at -70˚C. cDNA synthesis was performed using RevertAid reverse transcriptase. Real-time PCR analysis was conducted using TB Green® Premix Ex Taq™ II according to manufacturer's protocol. PCR amplification was performed using AriaMX Real-Time PCR System (Agilent Technologies). Relative miRNA expression levels were normalized to reference genes SNORD66 and SNORD44.

Micronucleus test

As for MN analysis, a modified CBMN (cytokinesis-block micronucleus) assay using cytochalasin B was used. Participant samples after diagnosis were separated into two cohorts; controls and in vitro irradiated with a dosage 2 Gy using TrueBeam linear accelerator (Varian, Palo Alto, CA, USA). Samples from patients undergoing RT were monitored during treatment, without any additional in vitro irradiation. Lymphocyte suspension was stained with 4% Giemsa-Romanowski solution and analyzed using automated microscopy with Metafer_v.4 (MetaSystems Altlussheim, Germany) and AxioImager.Z2 (Carl Zeiss, Germany). Relative miRNA expression was calculated using the $2^{-\Delta\Delta Ct}$ method. Statistical analysis included the Mann-Witney test and a linear mixed-effects model (LMM). MN frequency was tested for normality using the Shapiro-Wilk test, followed by ANOVA analysis in GraphPad Prism 8.0 software (San Diego, CA, USA). Results were considered significant at $p < 0,05$.

Results and Discussion

We analyzed the expression of 9 miRNAs (miR-10, miR-191, miR-195, miR-20, miR-21, miR-221, miR-223, miR-34, and miR-590) in the peripheral blood of 14 GBM patients and 9 controls (Figures 1 and 2). At first, we compared miRNA expression levels between patients before therapy and healthy controls to assess whether these

changes could be used for GBM detection and the prediction of prognosis (Figure 1). The expression did not differ significantly between controls and patients before therapy, except for oncogenic miR-10, which showed significantly lower expression in patients ($p = 0{,}0456$). Although we initially expected oncogenic miRNAs to upregulated, several biological factors may have a role in this finding. One possible explanation is the selective blood-brain barrier (BBB), which regulates the transport of molecules between the central nervous system and peripheral blood. GBM is highly invasive and capable of infiltrating brain regions, where BBB remains intact – this might explain, why tumor-derived oncogenic miRNAs are not released into peripheral blood and why GBM can effectively escape therapy [7]. Reduced miR-10 levels were observed in patients whose overall survival (OS) was above 12 months, indicating less invasive tumor phenotype and improved prognosis [8].

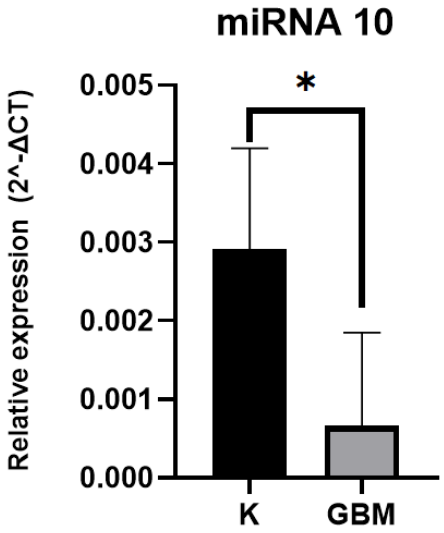

Figure 1: Relative expression changes between healthy controls and glioblastoma patients before therapy. The graph shows relative expression ($2^{-\Delta\Delta Ct}$) of miR-10 in healthy controls (K, n = 9) and GBM patients at the time of diagnosis (GBM, n = 14). Data are presented as median with 95% CI (confidence interval). Statistical analysis was performed with Mann-Whitney, $*p < 0{,}05$.

Next, we analyzed miRNA levels in patients throughout therapy across four therapy stages (collections 1 – 4) to identify miRNAs with significant changes reflecting therapy response (Figure 2). Expression profiles differed between patients, although they remained relatively stable within individual patients during therapy. These results were not confirmed as statistically significant. Tumor-suppressive miR-34 showed decreased levels at collection 2, however, a significant increase was observed after collection 3 ($p = 0{,}014518$) and collection 4 ($p = 0{,}00000316$) in all patients. Increased expression of miR-34 disrupts tumor cell proliferation through the inhibition of oncogenes [9] and simultaneously enhances sensitivity to TMZ [10]. Since miR-34 is considered a tumor-suppressive miRNA, we assume that patients with a better therapeutic response will have higher miR-34 levels, although more studies are needed to further validate our claims.

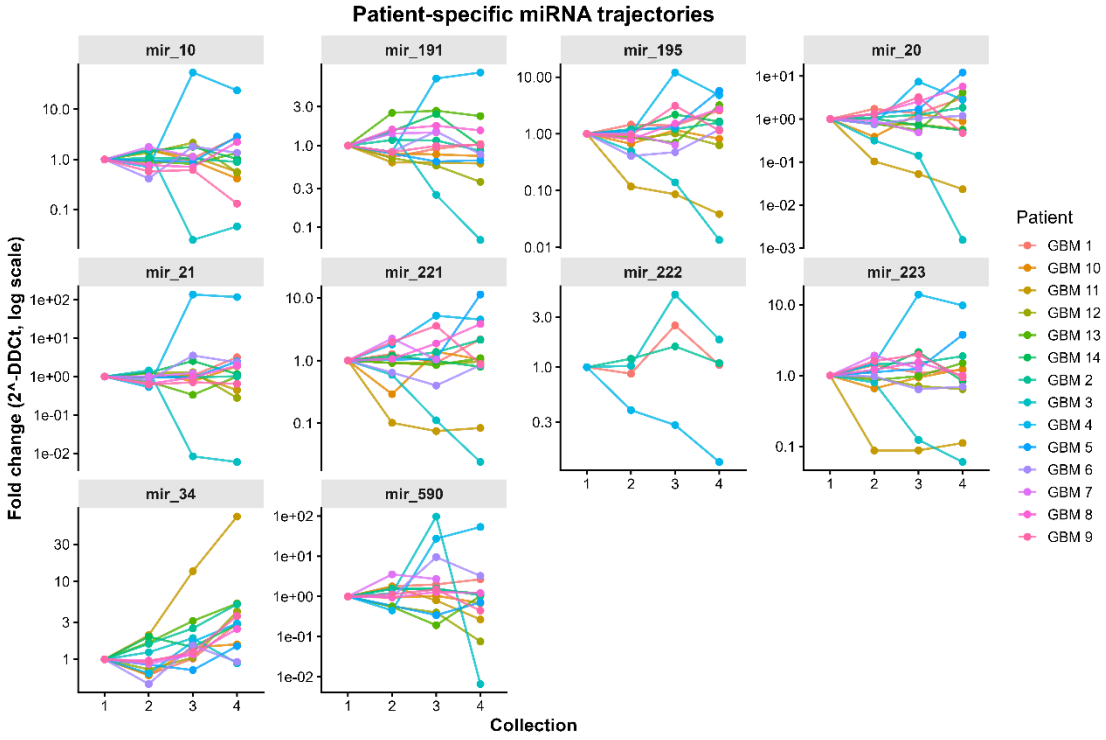

Figure 2: miRNA expression in glioblastoma patients throughout therapy. The figure shows relative expression of 9 miRNAs (miR-10, miR-191, miR-195, miR-20, miR-21, miR-221, miR-223, miR-34 a miR-590) in GBM patients (n=14) throughout therapy (collection 1-4). Relative miRNA expression was calculated using the 2−ΔΔCt method (log scale) and normalized to housekeeping genes SNORD66, SNORD44 and therapy stage 1 using LMM. miR-222 was excluded from the study.

To evaluate the genotoxic effects of RT in 4 GBM patients, we scored MN in 1000 binucleated cells per sample (Figure 3A). A significantly higher frequency of MN was observed in therapy stage 4 compared to stage 2 (p = 0,0231), suggesting enhanced chromosomal damage caused by IR. To assess radiation-induced changes ex vivo, we analysed MN yield of GBM patients and healthy controls before therapy (0 Gy) as well as after exposure to 2 Gy (Figure 3B). Significant differences were observed among several groups, notably control 0 Gy and control 2 Gy (p = 0.0029) and GBM 0 Gy and GBM 2 Gy (p = 0.0025). Differences between controls and patients under the same conditions (0 Gy vs. 0 Gy; 2 Gy vs. 2 Gy) were not observed. This might suggest that both samples received the same in vitro irradiation dose of 2 Gy and that cells did not show increased MN formation in the absence of IR. These results indicate that IR exposure may contribute to genomic instability and induce changes in MN frequency, reflecting higher levels of DNA damage.

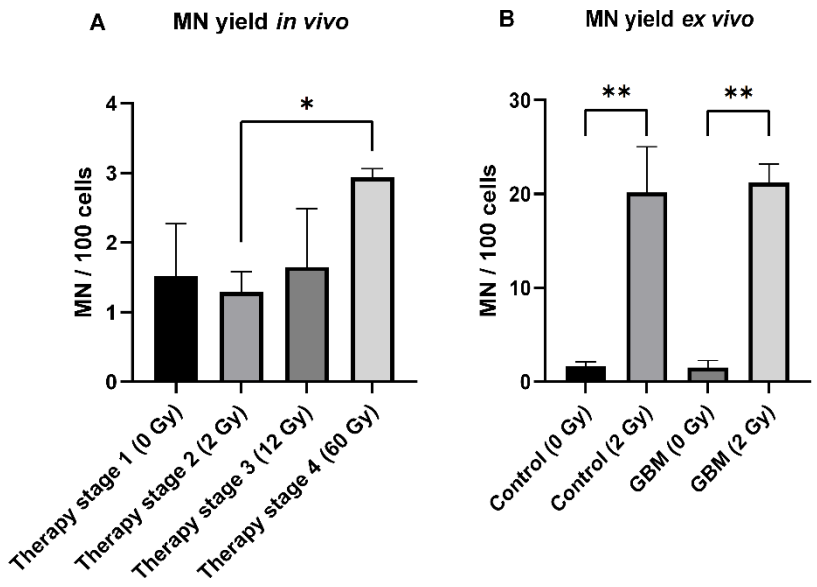

Figure 3: Micronuclei yield in glioblastoma patients in vivo and ex vivo. The graphs show micronuclei (MN) frequency with 95% CI (confidence interval) as a number of MN in 100 binucleated cells for each sample. (A) MN yield in peripheral blood cells of GBM patients (n=4) at 4 subsequent therapy stages. (B) MN yield in peripheral blood cells of GBM patients (n=4) and controls (n=3) before (0 Gy) after ex vivo irradiation (2 Gy). Statistical analysis was performed with ANOVA, *$p < 0,05$; **$p < 0,01$).

Conclusion

Our analysis revealed significant downregulation of oncogenic miR-10 in GBM patients before therapy compared with controls; however, no other miRNAs were statistically significant despite noticeable differences in expression levels. We observed significant changes in miR-34 expression following treatment, suggesting its potential as a biomarker for therapy response. Our results further indicate that MN frequency changes throughout therapy, possibly reflecting IR-induced DNA damage. Significant differences between early and late collections suggest that MN frequency might serve as a biomarker for monitoring therapy response. However, more functional studies with larger cohorts are needed to validate these claims and assess the role of miR-10, miR-34, and MN in GBM treatment. Overall, our results may help to monitor the efficacy of anti-cancer treatment in GBM patients and improving individualized patient care.

Acknowledgement

We would like to thank Oncology Clinic of Saint Elisabeth in Bratislava for performing in vitro cell irradiation and Mgr. Jan Roška, PhD. for help with primer design.

References

[1] Grochans S, Cybulska AM, Simińska D, Korbecki J, Kojder K et al. Epidemiology of glioblastoma multiforme–literature review. Cancers 2022; 14(10), 2412. doi: 10.3390/cancers14102412

[2] Ronvaux L, Riva M, Coosemans A, Herzog M, Rommelaere G et al. Liquid biopsy in glioblastoma. Cancers 2022; 14(14), 3394. doi: 10.3390/cancers14143394.

[3] Bartel DP. MicroRNAs: genomics, biogenesis, mechanism, and function. Cell 2004; 116(2), 281-297. doi: 10.1016/s0092-8674(04)00045-5.

[4] Zhang B, Pan X, Cobb GP, Anderson TA. microRNAs as oncogenes and tumor suppressors. Dev. biol. 2007; 302(1), 1-12. doi: 10.1016/j.ydbio.2006.08.028.

[5] Hintzsche H, Hemmann U, Poth A, et al. Fate of micronuclei and micronucleated cells. Mutat Res Rev Mutat Res. 2017; 771:85. doi: 10.1016/j.mrrev.2017.02.002.

[6] Krupina K, Goginashvili A, Cleveland DW. Causes and consequences of micronuclei. Curr Opin Cell Biol. 2021; 70:91–99. doi: 10.1016/j.ceb.2021.01.004.

[7] Banelli B, Forlani A, Allemanni G, Morabito A, Pistillo MP, Romani M. MicroRNA in glioblastoma: an overview. Int J Genomics. 2017; 2017:7639084. doi: 10.1155/2017/7639084.

[8] Bafiti V, Ouzounis S, Chalikiopoulou C, et al. A 3-miRNA signature enables risk stratification in glioblastoma multiforme patients with different clinical outcomes. Curr Oncol. 2022; 29(6):4315–4331. doi: 10.3390/curroncol29060345.

[9] Hermeking H. The miR-34 family in cancer and apoptosis. Cell Death Differ. 2010; 17(2):193–199. doi: 10.1038/cdd.2009.56.

[10] Abdoli Shadbad M, Baghbanzadeh A, Baradaran B. hsa-miR-34a-5p enhances temozolomide anti-tumoral effects on glioblastoma: in-silico and in-vitro study. EXCLI J. 2024; 23:384. doi: 10.17179/excli2023-6404.

OPTIMIZATION OF 3D *IN VITRO* MODELS FOR CCRCC RESEARCH

Kamila Bernatova, Barbora Puzderova, Petra Belvoncikova, Eva Kocianova, Monika Barathova

Biomedical Research Center SAS, Institute of Virology, Dubravska cesta 9, 845 05 Bratislava, Slovakia

Introduction

Modern experimental oncology is increasingly focused on the refinement and expansion of preclinical models capable of mimicking the heterogeneity of tumor tissue, the dynamics of cellular interactions, and the complexity of processes occurring within tumors. In vitro models represent a key tool in cancer research, as they enable the study of tumor cells under controlled conditions, the analysis of mechanisms of growth, invasion, and metastasis, as well as the testing of the efficacy of anticancer therapeutics. However, traditional 2D cell cultures are unable to adequately replicate the complexity and heterogeneity of the tumor microenvironment; therefore, it is essential to develop and optimize more advanced in vitro models, such as spheroids and organoids [1]. Spheroids, as an important type of 3D model, enable the growth of cells in multiple layers, thereby more faithfully mimicking the architecture of tumor tissue. The cells establish intercellular interactions and form gradients of nutrients, oxygen, and pH, including a hypoxic to necrotic core. Co-culture spheroids further expand this complexity by incorporating interactions between different cell types, more accurately reflecting tumor heterogeneity and enabling more precise prediction of treatment response. Despite these advantages, however, spheroids are still unable to fully reproduce the complex tumor microenvironment [2]. Tumor organoids are three-dimensional structures derived from tissue-specific stem cells. They retain the key morphological and genetic characteristics of the original tumor, enabling comparison with benign or untreated tissue as well as the analysis of autologous immune responses. Their limitations include variable success rates in preparation and cultivation depending on the tissue type, as well as the need for specifically optimized culture conditions. Nevertheless, they represent a promising and one of the most advanced tools for studying tumor biology and developing personalized therapeutic strategies [3].

In the tumor microenvironment, carbonic anhydrase IX (CA IX) plays an important role, with its catalytic domain participating in the reversible hydration of CO_2 into bicarbonate ions and protons. Bicarbonate reabsorption leads to extracellular proton accumulation, thereby enabling CA IX to contribute to the maintenance of physiological

intracellular pH while simultaneously promoting acidification of the extracellular environment. CA IX plays a key role in the adaptation of tumor cells to hypoxia and supports their migration and invasiveness. It is strongly associated with hypoxic tumors or tumors with inactive pVHL. CA IX is considered one of the most reliable markers of tumor hypoxia, and its expression is linked to an aggressive phenotype, metastatic potential, and poor response to treatment. CA IX expression is primarily activated by hypoxia through the hypoxia inducible factor 1 (HIF-1) signaling pathway [4].

Clear cell renal cell carcinoma (ccRCC) represents the most common type of renal cell carcinoma (RCC). ccRCC tumors are characterized by mutations associated with the loss of the short arm of chromosome 3p, which contains key tumor suppressor genes such as VHL, BAP1, PBRM1, and SETD2. In up to 90% of ccRCC cases, pVHL is inactivated, leading to stabilization of the alpha regulatory subunit of HIF-1(HIF-1α) and subsequent oxygen-independent activation of HIF signaling. The result is a condition referred to as pseudohypoxia, which subsequently increases CA IX expression in ccRCC [5].

In our experiments, we focus on optimizing the preparation and cultivation of advanced 3D in vitro models, including spheroids derived from commercial cell lines (both homotypic and heterotypic with fibroblasts) and organoids prepared from native patient tumor tissue. Using co-culture models with PBMCs (peripheral blood mononuclear cells), we investigate the interactions and infiltration of immune cells into 3D structures. These models are also employed for testing novel potential therapeutics targeting CA IX in combination with standard therapy. The use of tumor tissue in in vitro analyses may significantly contribute to improved patient stratification for effective therapy.

Materials and methods

Cell culture and spheroid preparation.

Commercially available cell lines SKRC-52, RCC4, and A498 (derived from RCC patient tumor tissue carrying a mutated VHL gene), as well as RCC4 VHL and A498 VHL cell lines (containing a functional copy of the VHL gene), were cultured in DMEM growth medium (Biosera) supplemented with 10% fetal bovine serum (HyClone Laboratories) and 0.1% gentamicin (Biosera). HFK cells (human kidney fibroblasts) were cultured in FM Plus growth medium (Innoprot) supplemented with 10% fetal bovine serum (HyClone Laboratories), 0.1% gentamicin (Biosera), and Fibroblast Growth Kit–Serum-Free growth factors (ATCC). Spheroids were prepared using ultra-low attachment plates, with cells seeded at a density of 50 cells/µl for SKRC-52 cells and 100 cells/µl for the remaining cell lines. For the preparation of co-culture spheroids, renal tumor cells were seeded together with HFK cells at a 1:1 ratio. Spheroid growth was maintained for 5 days. In experiments involving treatment with Everolimus (50 nM), either alone or in combination with CA9hu-2 (25 µg/ml), the incubation period lasted 3 days. PBS and DMSO, in which Everolimus was dissolved, were used as controls.

Western blot

Spheroids were lysed using RIPA lysis buffer (1 mM EDTA, 0.1% SDS, 50 mM Tris-HCl, pH 7.4, 150 mM NaCl, 1% Triton X-100, 0.05% sodium deoxycholate). Following

electrophoretic separation of proteins by SDS-PAGE and their transfer onto PVDF membranes (Macherey-Nagel), the membranes were blocked with 5% milk. Subsequently, the membranes were incubated with primary antibodies (HIF-2α 1:500, HIF-1α 1:250, CA IX 1:200, β-actin 1:1000). After incubation, the membranes were washed and then incubated with secondary antibodies, anti-mouse IgG/HRP (Dako) or anti-rabbit IgG/HRP (Dako), diluted 1:5000 for 1 h. Following washing, the membranes were developed using a chemiluminescent substrate (ECL), and the signal was detected by exposure to X-ray films (FUJI).

Immunofluorescence

Spheroids and organoids were fixed with 4% paraformaldehyde and incubated with the primary antibody M75 (anti-CA IX) at 37 °C for 1 h. After washing, samples were incubated with the secondary antibody anti-mouse Alexa Fluor 555 diluted 1:1000 at 37 °C for 1 h. For immunofluorescent staining of monolayers derived from patient organoids, fixation was performed using methanol, followed by incubation with primary antibodies at 37 °C for 1 h in the following order: anti-CA IX (mouse). After washing, cells were incubated with a primary anti-α-SMA antibody (rabbit) diluted 1:300. After further washing, cells were incubated with a mixture of secondary antibodies, anti-mouse Alexa Fluor 555 and anti-rabbit Alexa Fluor 488, both diluted 1:1000 at 37 °C for 1 h. Cell nuclei were stained with Hoechst 33342 (Invitrogen H3570) diluted 1:1000 for 10 min at 37 °C. Fluorescent signals were detected using a Cytation C10 imaging system (BioTek).

Organoid preparation

Patient tissue samples were first mechanically and then enzymatically dissociated using 1% collagenase. The resulting single-cell suspension was subsequently washed several times, cells were mixed with extracellular matrix (BME) and plated as droplets in suspension plates in the presence of optimized growth medium enriched with kidney-specific growth factors.

Immunohistochemistry

On tissue sections, CA IX protein was detected using the Dako EnVision FLEX+ System, HRP. Sections were incubated for 1 h with the primary antibody M75 diluted 1:100 in Antibody Diluent (Dako). After washing, incubation with a secondary anti-mouse-HRP antibody (Dako) was performed for 30 min. Staining was visualized using 3,3′-diaminobenzidine (DAB) as the chromogenic substrate, with incubation for 1 min. After washing, nuclei were counterstained with hematoxylin (Dako) for 8 min. Slides were mounted using Aquatex mounting medium (Merck). Prepared slides were subsequently analyzed using a Leica DM4500B microscope equipped with a Leica DFC480 camera.

Treatment and detection of apoptosis and necrosis in organoids

After expansion, patient-derived organoids were incubated for 3 days with tyrosine kinase inhibitors (TKIs), Axitinib (5 μM) and Pazopanib HCl (10 μM), either alone or in combination with a humanized antibody against CA IX, CA9hu-2, which effectively inhibits the enzymatic activity of CA IX at a concentration of 25 μg/ml [6]. Organoids incubated with PBS served as controls. The level of apoptosis and necrosis was assessed using the Apoptosis/Necrosis Assay Kit (Abcam). Cell nuclei were stained with Hoechst

33342 (Invitrogen H3570) diluted 1:1000 for 10 min. Fluorescent signals were detected using a Cytation C10 imaging system (BioTek).

Results and discussion

In our experiments, we prepared homotypic spheroids (renal tumor cells) as well as heterotypic spheroids (renal tumor cells + fibroblasts). The heterotypic spheroids exhibited higher compactness and density, more pronounced proliferative gradients, and the formation of a hypoxic to necrotic core, thereby more faithfully recapitulating tumor characteristics (Fig. 1).

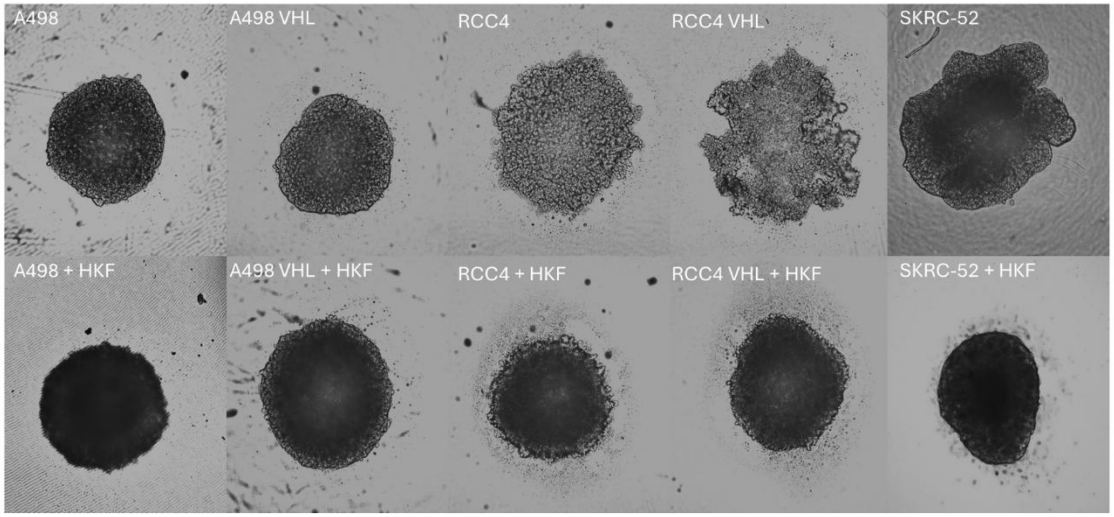

Fig. 1 Comparison of spheroid formation by tumor cells and by a combination of tumor cells and HKF (human kidney fibroblasts).

Given the high expression of CA IX in ccRCC, we focused on evaluating the effect of its inhibition using the humanized antibody CA9hu-2 in combination with standard therapy. The mTOR inhibitor Everolimus (EVR), tested both alone and in combination with CA9hu-2, showed a more pronounced effect under combined treatment conditions. Western blot analysis revealed a reduction in the levels of HIF-1α, HIF-2α, and CA IX, although these are not direct targets of EVR (Fig. 2A). These findings were further validated by immunofluorescence analysis of SKRC-52 spheroids, where combined EVR and CA9hu-2 treatment resulted in the most pronounced decrease in CA IX expression. In addition, morphological changes in spheroids were also observed (Fig. 2B).

Organoids represent an advanced in vitro model for studying tumor biology. Organoids derived from ccRCC patients whose tumor tissues showed CA IX positivity by immunohistochemical staining retained this characteristic in vitro, as confirmed by immunofluorescence analysis. In contrast, benign tissues and organoids derived from them were CA IX-negative (Fig. 3A), indicating the preservation of key molecular characteristics of the original tissue in organoid models.

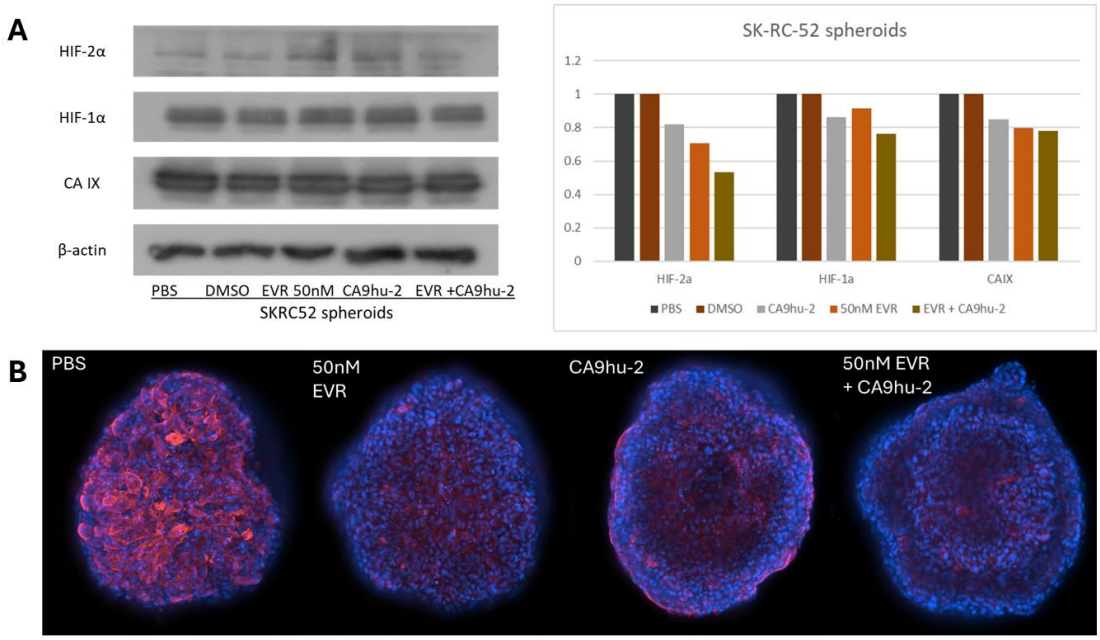

Fig. 2 A. Western blot analysis of the effect of Everolimus (EVR), CA9hu-2, and their combination on the protein levels of hypoxia-related signaling molecules HIF-1α, HIF-2α, and CA IX in SKRC-52 spheroids. β-actin was used as a loading control. PBS and DMSO were used as controls.

Fig. 2 B. Immunofluorescence analysis of CA IX protein levels in SKRC-52 spheroids following treatment with EVR, CA9hu-2, and their combination. PBS was used as a control.

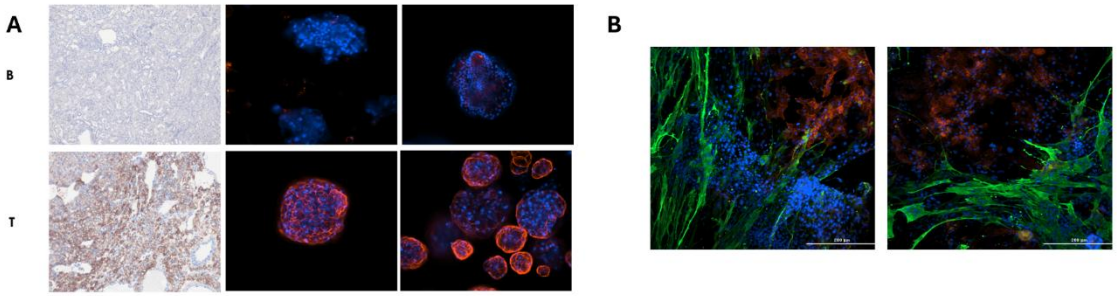

Fig. 3 A. Immunohistochemical staining of CA IX in benign (B) and tumor (T) tissue from a ccRCC patient, and immunofluorescence staining of CA IX (red) in organoids derived from these tissues. Cell nuclei were stained with Hoechst 33342 (Invitrogen H3570) (blue).

Fig. 3 B. Immunofluorescence staining of CA IX (red) and α-SMA (green) in a monolayer derived from patient organoids. Cell nuclei were stained with Hoechst 33342 (Invitrogen H3570) (blue).

Patient-derived tumor organoids were incubated with Axitinib and Pazopanib alone, as well as in combination with CA9hu-2, and the levels of apoptosis and necrosis were assessed. In the first patient, induction of apoptosis was observed, with a more pronounced effect in the Axitinib plus CA9hu-2 combination than with Axitinib alone, while Pazopanib exhibited the strongest effect overall. In contrast, the second patient showed a high level of necrosis already in the control samples, which persisted after drug treatment without a significant induction of apoptosis, indicating a low therapeutic response (Fig. 4). Immunofluorescence analysis of monolayers derived from organoids confirmed marked cellular heterogeneity, with detection of CA IX-positive cells (red) and α-SMA-positive fibroblasts (green), as well as cell populations lacking detectable

signal (Fig. 3B). These findings demonstrate pronounced intratumoral and interindividual heterogeneity and highlight the importance and necessity of a personalized therapeutic approach.

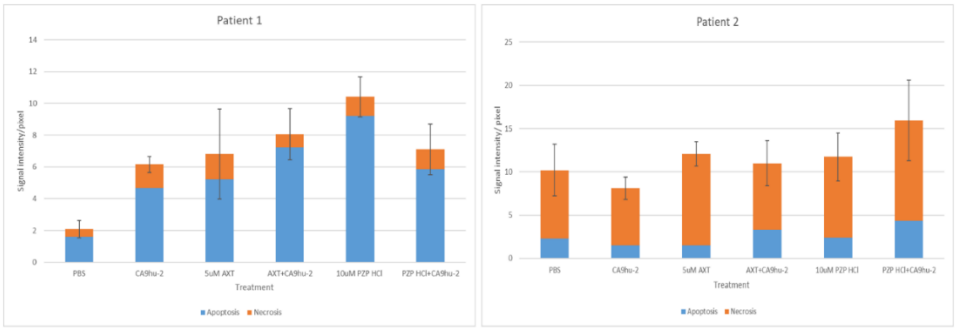

Fig. 4. Graphical evaluation of the levels of apoptosis and necrosis in patient-derived tumor organoids after treatment with Axitinib and Pazopanib, administered alone and in combination with CA9hu-2. PBS was used as a control.

Conclusion

In conclusion, there is a continuous need to improve experimental models to advance cancer research. Patient-derived organoids closely recapitulate the original tissue and represent one of the most physiologically relevant experimental systems, incorporating aspects of the tumor microenvironment. They provide a promising platform for testing new therapeutics and for personalized medicine approaches. Our results also suggest that CA IX is a promising therapeutic target in ccRCC.

Acknowledgements

This work was supported by the projects APVV-23-0496, VEGA 2/133/24, APP0629.

References

[1] Abbas ZN, Al-Saffar AZ, Jasim SM, Sulaiman GM. Comparative analysis between 2D and 3D colorectal cancer culture models for insights into cellular morphological and transcriptomic variations. Sci Rep. 2023;13(1):18380. Published 2023 Oct 26. doi:10.1038/s41598-023-45144-w

[2] Hirschhaeuser, F., Menne, H., Dittfeld, C., West, J., Mueller-Klieser, W., et al. (2010). Multicellular tumor spheroids: an underestimated tool is catching up again. Journal of biotechnology, 148(1), 3–15.

[3] Veninga, V., & Voest, E. E. (2021). Tumor organoids: Opportunities and challenges to guide precision medicine. Cancer cell, 39(9), 1190–1201.

[4] Pastorek, J., & Pastorekova, S. (2015). Hypoxia-induced carbonic anhydrase IX as a target for cancer therapy: from biology to clinical use. Seminars in cancer biology, 31, 52–64.

[5] Gnarra JR, Tory K, Weng Y, Schmidt, L., Wei, M. H., et al. Mutations of the VHL tumour suppressor gene in renal carcinoma. Nat Genet. 1994;7(1):85-90. doi:10.1038/ng0594-85

[6] Zatovicova M, Kajanova I, Takacova M, Jelenska, L., Sedlakova, O., et al. ADAM10 mediates shedding of carbonic anhydrase IX ectodomain non redundantly to ADAM17. Oncol Rep. 2023;49(2):27. doi:10.3892/or.2022.8464

ANTIBODY-DRUG CONJUGATES AS A NEW THERAPEUTIC OPTION IN CHEMO-RESISTANT GERM CELL TUMORS

Adriana Fekiacova[1,2], Natalia Udvorkova[1,2], Michal Mego[2], Lucia Kucerova[1,2]

[1]Department of Molecular Oncology, Cancer Research Institute, Biomedical Research Center, Slovak Academy of Sciences, Dubravska cesta 9, 845 05 Bratislava, Slovakia
[2]Translational Research Unit, 2nd Oncology Clinic of the Medical Faculty and the National Cancer Institute, Klenova 1, 833 10 Bratislava

Introduction

Over the past decades, cisplatin-based chemotherapy has remarkably ameliorated clinical outcomes of patients with germ cell tumors (GCTs). Despite this, a subset of these patients is burdened with recurrent or chemorefractory tumors and often has a dismal prognosis. Effective therapeutic approaches for the treatment of chemoresistant GCTs are currently lacking [1]. Antibody-drug conjugates (ADCs) offer a promising strategy that has already been employed with success in several types of solid tumors. Through a chemical linker, these molecules combine the specificity of monoclonal antibodies with the potent antitumor effect of cytotoxic payloads. ADCs work by recognizing and binding target antigens overexpressed on the tumor cell surface. Upon binding, the conjugate is internalized into the cell through the process of endocytosis. Inside, the linker is degraded and the cytotoxic drug is released. This conjugated agent usually acts as a disruptor to either DNA or microtubules, thereby impeding essential processes of the cancer cell and ultimately leading to cell death [2]. Therefore, ADCs enable targeted delivery of cytotoxic drugs to tumor cells while minimizing off-target toxicity towards non-malignant cells. The main scope of our work aims to identify the presence of suitable antigens in GCTs that can be targeted with ADCs currently used in clinical practice. In this study, we focused on two target antigens – folate receptor alpha (FRα) and human epidermal growth factor 2 (HER2). FRα is a receptor with a glycosylphosphatidylinositol anchor localized on the cell membrane, where it aids in the cellular uptake of folate. Its limited expression in normal tissues and overexpression in several types of cancer make it an ideal target for effective ADC therapy. This treatment strategy can be mediated by Mirvetuximab soravtansine (MIRV), an anti-FRα directed ADC, conjugated to a microtubule disruptor DM4. MIRV was recently approved for use in platinum-resistant ovarian, peritoneal and fallopian tube cancer. HER2, an EGFR membrane receptor that promotes cancer cell proliferation and invasion, is a target surface antigen for Trastuzumab deruxtecan (T-DXd), in which the conjugated payload, deruxtecan, inhibits topoisomerase I [3].

Material and methods

Cell lines

In our experiments, we used a panel of parental and derived cisplatin-resistant (CisR) isogenic variants of GCT cell lines, including the following histological subtypes: seminoma, embryonal carcinoma, choriocarcinoma, yolk sac tumor (testicular/ovarian), and teratoma/teratocarcinoma. Additionally, cell lines originating from other types of cancers (breast cancer or uterine cancer) and cell lines of non-malignant origin were used as control samples for gene expression assays.

Gene expression

We determined mRNA expression profiles of the encoding genes of target antigens (FOLR1 and ERBB2, respectively) by RT-qPCR, using SYBR® Green technology (Promega) for FOLR1 and TaqMan Gene Expression Assay (Thermo Fisher Scientific; Inc.) for ERBB2. RNA was isolated using NucleoSpin RNA Mini Kit (Macherey-Nagel) and QIAwave RNA Mini Kit (Qiagen) and purity and concentration were determined on NanoDrop™ 1000 Spectrophotometer (Thermo Fisher Scientific, Inc.). RNA was transcribed to cDNA using RevertAid First Strand cDNA Synthesis Kit (Thermo Fisher Scientific, Inc.).

Cell exposure

To establish the sensitivity of GCT cell lines to ADC-based treatments using MIRV and T-DXd, cells were seeded in a 96-well plate at a seeding density of $5x10^4$ cells per well. For spheroid cultures, an U-bottom 96-well plate was used and cells were seeded at a density of $1x10^5$ cells per well. At assay endpoints – day 3 after treatment for 2D cells and day 4 after treatment for 3D cells – cell viability was determined using luminescent cell viability assay CellTiter-Glo® (Promega) and measured with GloMax® Discover Microplate Reader (Promega).

Results

Prior to our experiments, we conducted a small in silico analysis of the public databases cBioPortal (https://www.cbioportal.org/) and GEPIA2 (http://gepia2.cancer-pku.cn/) to gain an insight into the gene expression of the encoding genes in testicular germ cell tumors (TGCTs). In the case of *FOLR1*, it was significantly upregulated in patient tumor tissue compared to healthy tissue. *ERBB2* did not show a significant upregulation in TGCTs in comparison to healthy samples, however, most of the patient samples had substantial levels of *ERBB2* expression.

Within our TGCT cell line panel, we confirmed high expression of *FOLR1* in several of the parental and cisplatin-resistant variants of GCT cell lines, especially in seminoma, choriocarcinoma and teratoma. Additionally, we confirmed that *FOLR1* is minimally expressed in non-malignant cells (Fig. 1A). At the same time, a moderate expression of *ERBB2* was identified in some of the cell lines (Fig. 1B). Interestingly, expression of both genes had a tendency to be upregulated in cisplatin-resistant variants of GCTs, with notable differences primarily in *ERBB2* (Fig. 1).

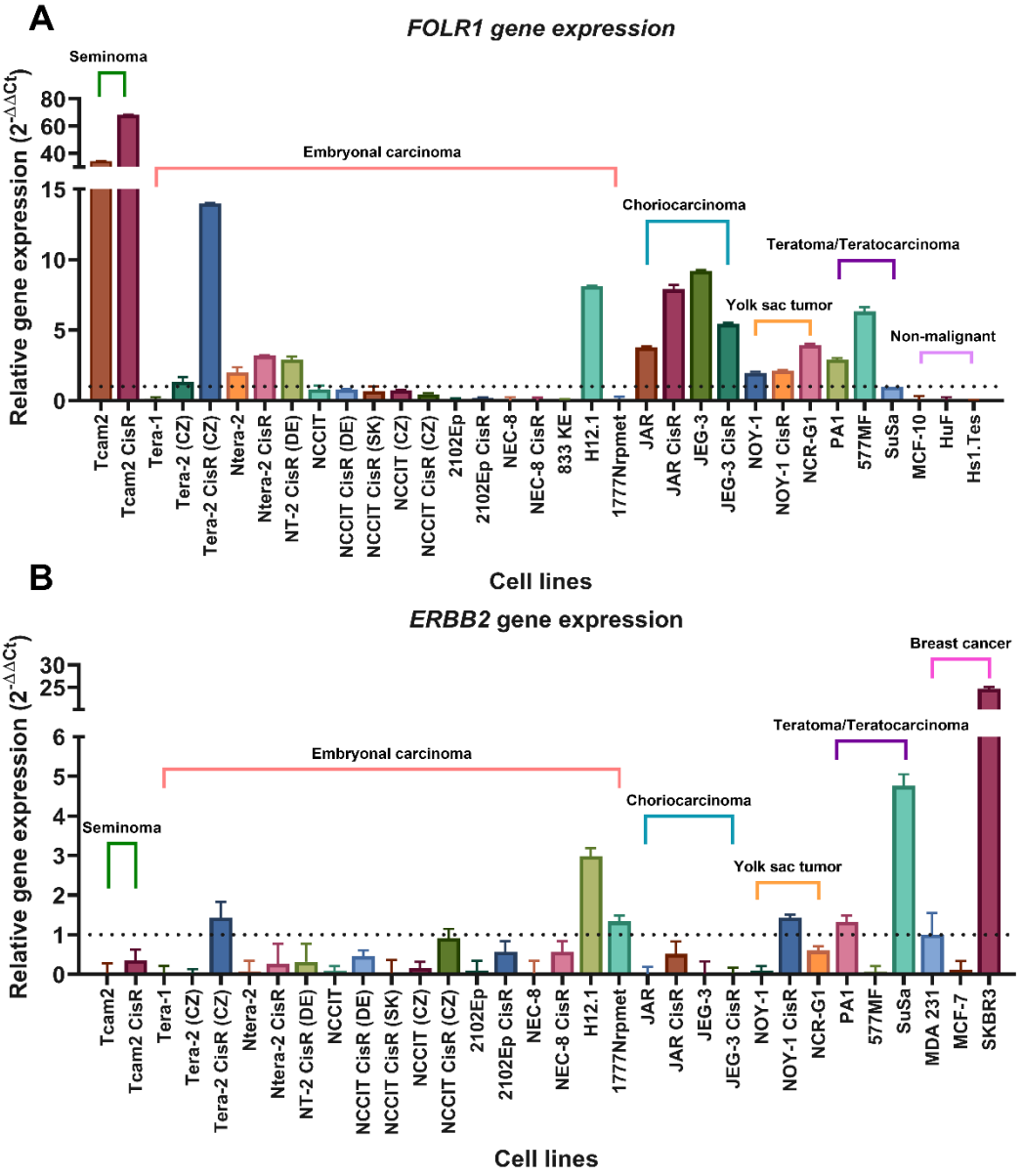

Figure 1: Relative gene expression of FOLR1 gene (A) and ERBB2 gene (B) evaluated in a panel of GCT cancer cell lines, other types of cancers or in non-malignant cells. Data are expressed as fold change in expression ± SD, evaluated with the 2-ΔΔCt method.

For initial analyses, we tested the efficacy of anti-FRα ADC compound MIRV only on resistant variants of the lines, as the primary aim is to treat refractory tumors. In adherent 2D cell cultures, we observed a significant decrease in proliferation in most lines even at lower concentrations (Fig. 2A). In contrast, in 3D spheroids, observable cell inhibition by MIRV was limited to only a few cell lines, namely chemoresistant embryonal carcinoma cell line, NT2 CisR, and choriocarcinoma cells JEG-3 CisR and JAR CisR (Fig. 2B), which correlated well with their higher *FOLR1* expression (Fig. 1A).

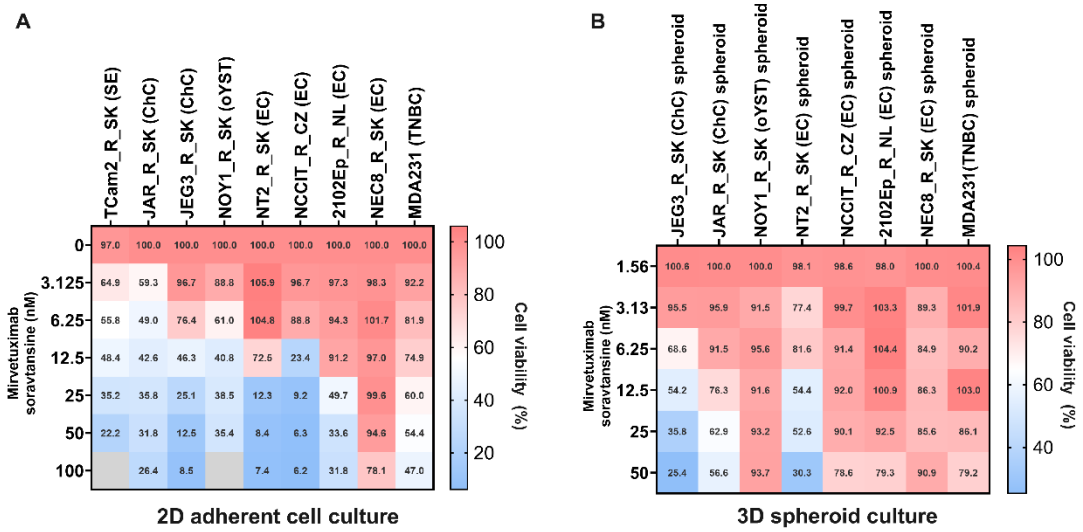

Figure 2: Antiproliferative effects of MIRV in (A) 2D adherent and (B) 3D spheroid cell cultures. Values were determined by luminescent viability assay and are reported as mean values ± SD of quadruplicates. EC – embryonal carcinoma, ChC – choriocarcinoma, oYST – ovarian yolk sac tumor, SE – seminoma, TNBC – triple negative breast cancer

In our preliminary experiments, T-DXd targeted towards HER2, demonstrated potent cytotoxicity in teratoma, represented by SuSa cell line as well as embryonal carcinomas NEC-8 or NT2 or male yolk sac tumor line NCR-G1 (Fig. 3).

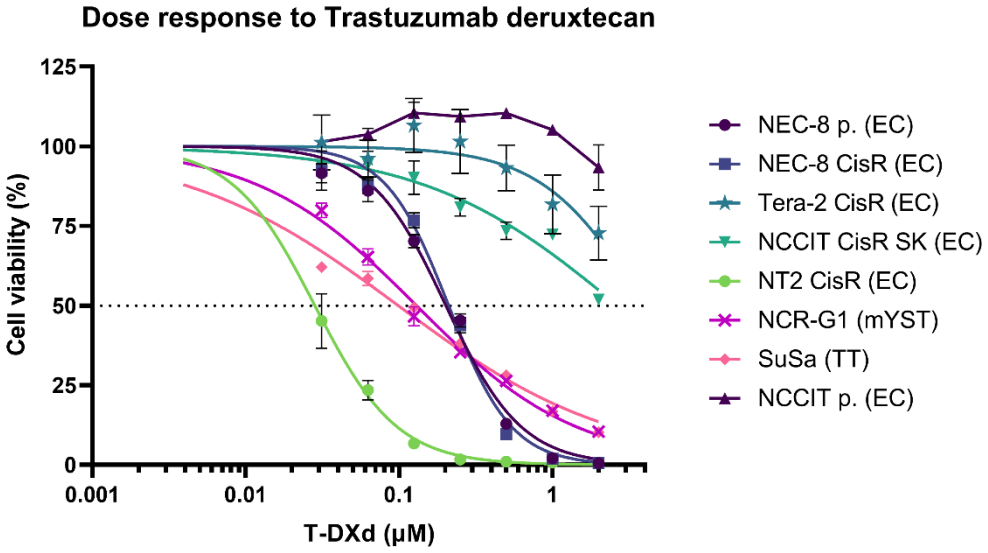

Figure 3: Antiproliferative effects of T-DXd. Values were determined by luminescent viability assay and are reported as mean values ± SD of triplicates.

Discussion

The exploration of various targets for ADCs in solid tumors, including TGCTs, is becoming more advantageous especially in light of increasing therapeutic resistance. Effective treatment in TGCTs following refractoriness to first-line therapy is a highly unmet medical need [4]. Expression levels of the cell surface markers that could be targeted with ADCs are largely unexplored in TGCTs. One of the recently explored tumor antigens in TGCTs is Claudin 6 (CLDN6), a tight junction protein overexpressed in several types of solid tumors and with minimal activity in healthy tissues. In patients with refractory tumors in a pan-cancer setting, a partial response was observed in one of the three testicular cancer patients with an ADC targeting CLDN6 in an ongoing clinical trial [5]. This highlights the rationale for use of ADCs in TGCTs, particularly in refractory disease. Previously, an ADC targeting the CD30 marker, brentuximab vedotin, was also evaluated in TGCT patients in two clinical trials with variable, albeit a few observable antitumor responses [6], warranting further research regarding CD30 as a target for ADCs in this disease. Another clinical trial investigating the efficacy of enfortumab vedotin, an ADC targeted at Nectin-4, is currently underway and will include testicular cancer patients [4]. In our study, detectable mRNA levels of encoding genes of both FRα and HER2 were measured in most TGCT cell lines, with considerable heterogeneity observed between different subtypes and different cell lineages (Fig. 1). Intertumoral heterogeneity as well as heterogeneity in expression levels between different histologies were also observed in patient samples accessed through cBioPortal (data not shown). At the same time, we noticed that cisplatin-resistant cells often showed higher mRNA levels of the encoding genes compared to parental variants, particularly in *ERRB2* (HER2) (Fig. 1B). This observation is in agreement with published literature, where cisplatin-resistant gastric and bladder cancer cells showed upregulation of ERBB2/HER2 at mRNA and protein levels compared to parental cells [7, 8]. We also observed a potent anti-tumor effect exerted by both MIRV and T-DXd in several cisplatin-resistant GCTs, highlighting the potential for their use in the refractory subset of patients. Recently, treatment with T-DXd was proven to be effective in pre-treated metastatic breast cancer patients even with low HER2 expression [9], which further potentiates the use of this ADC compound in low-expressing TGCT patients after treatment failure.

Conclusion

Our results indicate that ADC-mediated treatment targeting FRα and HER2 antigens could particularly provide clinical benefit to patients with chemorefractory TGCTs. Further validation of the suitability of the studied targets for ADC-mediated treatment in TGCTs is required, including flow cytometry to confirm surface expression of FRα and HER2 and in vivo confirmation of the efficacy of the aforementioned ADC compounds. Furthermore, determination of tumor sensitivity to the conjugated payload, deruxtecan, could provide additional information regarding cell sensitivity to T-DXd in TGCTs. Overall, our study supports the rationale for employing ADCs as an alternative to the current salvage chemotherapy in refractory TGCTs.

Acknowledgement

This work was supported by the Slovak Research and Development Agency under the Contract no. APVV-24-0168; the Scientific Grant Agency of the Ministry of Education and Science of the Slovak Republic – no. VEGA 2/0059/25; and the Cancer Research Foundation and the League against Cancer, Slovakia.

References

[1] Necchi A, Bratslavsky G, Corona RJ, Chung JH, Millis SZ, et al. Genomic Characterization of Testicular Germ Cell Tumors Relapsing After Chemotherapy. Eur Urol Focus. 2020; 6(1): 122-130. doi: 10.1016/j.euf.2018.07.013.

[2] Mansinho A, Albuquerque J, Barigazzi C, Calvo E. Antibody-drug conjugates in cancertreatment: from molecular design to clinical implementation. Lancet Reg Health Eur. 2026; 64: 101634. doi: 10.1016/j.lanepe.2026.101634.

[3] Wang R, Hu B, Pan Z, Mo C, Zhao X, et al. Antibody-Drug Conjugates (ADCs): current and future biopharmaceuticals. J Hematol Oncol. 2025; 18(1): 51. doi: 10.1186/s13045-025-01704-3.

[4] Chandran EBA, Atiq S, Simon N, Girardi D, Ley L, et al. E-VIRTUE: a study of enfortumab vedotin with or without pembrolizumab in rare genitourinary tumors-design and rationale. Future Oncol. 2025; 21(13): 1625-1630. doi: 10.1080/14796694.2025.2497719.

[5] Konecny GE, Wahner Hendrickson AE, Winterhoff B, Chander C, Bilic S et al. Initial results of dose finding in a first-in-human phase 1 study of a novel Claudin 6 (CLDN6) targeted antibody drug conjugate (ADC) TORL-1-23 in patients with advanced solid tumors. J. Clin. Oncol. 2023; 41(16_suppl): 3082–3082. doi: 10.1200/JCO.2023.41.16_suppl.3082

[6] Ghose A, Lapitan P, Apte V, Ghosh A, Kandala A, et al. Antibody Drug Conjugates in Urological Cancers: A Review of the Current Landscape. Curr Oncol Rep. 2024;26(6): 633-646. doi: 10.1007/s11912-024-01524-7.

[7] Huang D, Duan H, Huang H, Tong X, Han Y, et al. Cisplatin resistance in gastric cancer cells is associated with HER2 upregulation-induced epithelial-mesenchymal transition. Sci Rep. 2016; 6: 20502. doi: 10.1038/srep20502.

[8] Hayashi T, Seiler R, Oo HZ, Jäger W, Moskalev I, et al. Targeting HER2 with T-DM1, an Antibody Cytotoxic Drug Conjugate, is Effective in HER2 Over Expressing Bladder Cancer. J Urol. 2015; 194(4): 1120-31. doi: 10.1016/j.juro.2015.05.087.

[9] Modi S, Jacot W, Yamashita T, Sohn J, Vidal M, et al. Trastuzumab Deruxtecan in Previously Treated HER2-Low Advanced Breast Cancer. N Engl J Med. 2022; 387(1): 9-20. doi: 10.1056/NEJMoa2203690

LOW-DOSE HYPERFORIN ACTIVATES ADAPTIVE STRESS PATHWAYS IN HYPOXIC COLORECTAL CANCER CELLS

Lucia Hudakova[1], Martin Majernik[1], Zuzana Jendzelovska, Rastislav Jendzelovsky, Peter Fedorocko

Pavol Jozef Safarik University in Kosice, Faculty of Science, Institute of Biology and Ecology, Srobarova 2, 041 54 Kosice, Slovakia

Introduction

Solid tumours arise within a hostile microenvironment characterized by chronic hypoxia and extracellular acidosis, two closely interconnected stressors that profoundly shape tumour progression, metabolic plasticity and therapeutic resistance. In contrast to normal cells, tumour cells preserve a relatively alkaline intracellular pH despite the acidic extracellular milieu, thereby maintaining conditions favourable for proliferation, invasion, and survival. Because intracellular pH critically affects the activity of metabolic enzymes and signaling networks, maintenance of acid–base balance represents a fundamental adaptive mechanism in tumour cells. This adaptation is orchestrated through tightly interconnected pathways linking angiogenesis, metabolic reprogramming and pH regulation. A key regulator of these processes is HIF-1α, which controls the expression of genes associated with hypoxic adaptation, including vascular endothelial growth factor A (VEGF-A) and multiple mediators of metabolic and pH homeostasis [1].

Hyperforin (HF), a polyprenylated acylphloroglucinol derived from Hypericum perforatum L., has attracted considerable attention because of its pleiotropic anticancer effects. While higher HF concentrations (10–20 μM) exert anti-proliferative, pro-apoptotic and anti-angiogenic effects in multiple tumour models, lower subcytotoxic concentrations may induce distinct adaptive responses. In colorectal cancer cells, HF exposure at 1–5 μM has been associated with increased expression of VEGF-A and other pro-angiogenic factors [2]. Importantly, HF also acts as a protonophore capable of disrupting transmembrane proton gradients, suggesting a possible association with intracellular pH regulation and hypoxia-related cellular processes.

Despite these observations, the early molecular mechanisms underlying the cellular response to low-dose HF exposure under hypoxic conditions remain insufficiently understood. Therefore, the aim of this study was to investigate the early adaptive responses induced by subcytotoxic HF concentrations (1–5 μM) in HT-29 and

[1] These authors contributed equally to this work

HCT 116 colorectal cancer cells cultured under normoxic and hypoxic conditions, with particular emphasis on signaling pathways associated with hypoxic adaptation, intracellular pH regulation and tumour cell persistence.

Materials and methods

Reagents

Hyperforin dicyclohexylammonium salt (Hyperforin-DCHA; CAS No.: 238074-03-8; HPLC grade, Saint-Louis, Missouri, USA) was used in this study. A stock solution of HF was prepared in dimethyl sulfoxide (DMSO) at a concentration of 5 mM. The stock solution was stored long-term at −80 °C in the dark and diluted to the desired working concentrations immediately prior to application to the respective experimental groups. The final concentration of DMSO in all samples did not exceed 0.1%. Control cells were treated with serum-supplemented medium only.

Cell lines and culture conditions.

Human cancer cell lines HT-29 (colorectal adenocarcinoma) and HCT 116 (colorectal carcinoma) were used in this study. Cells were routinely maintained at 37 °C in a humidified incubator with 5% CO_2 in RPMI-1640 medium (HT-29; Sigma-Aldrich) or McCoy's 5A medium (HCT 116; PAN-Biotech GmbH, Aidenbach, Germany), supplemented with 10% fetal bovine serum (FBS) and antibiotics.

Cell exposure

Following seeding, cells were cultured for 24 h in a controlled atmosphere workstation (Coy Laboratory Products) under either hypoxic conditions (1% O_2, 5% CO_2, 37 °C) or normoxic conditions (20% O_2, 5% CO_2, 37 °C). Subsequently, HF was added at concentrations of 1 and 5 µM for Western blot analysis and 0.5–25 µM for the MTT assay (0.5, 0.75, 1, 2.5, 5, and 25 µM). Cells were then incubated in the dark for an additional 0.5, 2, or 24 h.

HF treatment, cell culture under HF exposure, and all subsequent processing steps were performed under strictly limited light conditions.

Cell metabolic activity (MTT assay)

MTT (3-(4,5-dimethylthiazol-2-yl)-2,5-diphenyltetrazolium bromide; 0.5 mg/mL), which is metabolized by viable cells into purple-colored crystalline formazan, was added to the cells at 24, 48, and 72 h following HF treatment. After a 4 h incubation, a 10% sodium dodecyl sulfate (SDS) solution was added to achieve a final concentration of 3.3%, thereby terminating MTT metabolism and solubilizing the formed formazan crystals. The absorbance of the dissolved formazan was measured the following day using a FluoStar Optima spectrofluorometer (BMG Labtech GmbH, Offenburg, Germany) at a wavelength of 585 nm.

Real-time monitoring of cell proliferation

To evaluate the effect of HF on cell proliferation, real-time analysis was performed using the IncuCyte™ ZOOM live-cell imaging system (IncuCyte™ ZOOM 2016B). The proliferation of HT-29 and HCT 116 cells was assessed by monitoring cell confluence following HF treatment. Images were acquired every 2 h over a total period of 72 h, and changes in proliferative kinetics were analyzed based on confluence measurements.

Western blot analysis

Cells were harvested by scraping on ice, washed with PBS, and lysed in lysis buffer (100 mM Tris-HCl, pH 7.4; 1% SDS; 10% glycerol) supplemented with protease and phosphatase inhibitors. Cell lysates were sonicated, and protein concentration was determined using the Lowry method. Samples (30 µg of protein per lane) were separated on a 10% SDS–polyacrylamide gel and transferred onto a PVDF membrane. After blocking, membranes were incubated overnight at 4 °C with primary antibodies against HIF-1α, phospho-Akt (Ser473), MCT4, and β-actin. Subsequently, appropriate horseradish peroxidase (HRP)-conjugated secondary antibodies were applied. Following washing, antibody reactivity was visualized using a chemiluminescent detection kit. Protein band intensities were quantified by densitometric analysis using Image Lab software (Bio-Rad).

Statistical Analysis

The results are expressed as the mean values ± standard deviation (SD) of at least two independent experiments. The data were analyzed using one-way ANOVA with Tukey's post-test. The groups treated with HF were compared with the untreated control (* $p < 0.05$, ** $p < 0.01$, *** $p < 0.001$).

Results and Discussion

Integrated *in vitro* analyses revealed a complex and context-dependent response of colorectal cancer cells to HF exposure. In our experimental setting, MTT analysis demonstrated a concentration-dependent reduction in metabolic activity in HT-29 and HCT 116 cells following 24 h HF exposure under normoxic conditions. More pronounced suppression was observed at intermediate HF concentrations, particularly in HCT 116 cells, indicating higher sensitivity of this cell line to HF treatment.

Under hypoxic conditions, prolonged HF exposure (24–72 h) progressively reduced metabolic activity at lower and intermediate concentrations in both cell lines. Interestingly, treatment with 25 µM HF induced partial restoration of metabolic activity , particularly after prolonged incubation and predominantly in HCT 116 cells, whereas HT-29 cells retained a comparatively more resistant phenotype throughout the experiment. Since MTT reduction primarily reflects mitochondrial and cellular redox activity rather than direct cell number, the partial restoration of metabolic activity detected at higher HF concentrations may indicate altered metabolic adaptation rather than improved cell survival.

These findings partially correspond with previously published observations by Majerník et al., who described time-dependent suppression of metabolic activity following prolonged HF exposure under normoxic conditions in HT-29, HCT 116 and CT26.WT colorectal cancer models. Their study further demonstrated substantially higher resistance of 3D spheroid cultures compared with conventional 2D models, highlighting the importance of tumour architecture and microenvironmental adaptation in determining cellular sensitivity to HF treatment [2]. Comparable HF-induced anti-tumour effects under normoxic conditions have also been reported in several other malignancies, including hepatocellular, bladder, and melanoma models. In HepG2 hepatocellular carcinoma cells, 48 h HF exposure resulted in an IC50 value of

approximately 19.87 µM [3], while TSGH-8301 bladder carcinoma cells responded to HF concentrations ranging between 10–30 µM following 24 h and 48 h treatment [4]. Notably, A375 melanoma cells appeared particularly sensitive to HF, exhibiting biological responses already at low micromolar concentrations with reported EC50 values ranging between 2–4 µM [5]. Together, these findings indicate that cellular sensitivity to HF is highly context-dependent and strongly influenced by tumour type, metabolic phenotype, and microenvironmental conditions.

Since MTT reduction does not necessarily directly reflect proliferative activity, the impact of HF on real-time growth dynamics was subsequently investigated using IncuCyte live-cell imaging analysis. Continuous real-time monitoring further revealed a pronounced anti-proliferative effect of HF under normoxic conditions, providing additional insight into the complex biological response induced by HF exposure. While lower HF concentrations exerted only modest effects on proliferative kinetics, treatment with 2.5–25 µM HF markedly suppressed cell confluence in both colorectal cancer cell lines throughout the entire 72 h monitoring period. In agreement with the MTT data, HCT 116 cells consistently displayed higher sensitivity to HF treatment compared with the more resistant HT-29 phenotype. Interestingly, proliferative behaviour did not fully correlate with the metabolic profiles observed in the MTT assay. Despite the partial restoration of MTT signal intensity detected following exposure to 25 µM HF, IncuCyte analysis demonstrated persistent suppression of cell proliferation at this concentration, suggesting that the elevated MTT signal more likely reflected altered mitochondrial and metabolic activity rather than enhanced proliferation or improved cell viability. These observations are in line with previously reported antiproliferative effects of HF in leukemia, murine colorectal carcinoma C-26, and HT-1080 fibrosarcoma models exposed to micromolar HF concentrations ranging approximately between 0.5 and 15 µM [6,7].

To further elucidate the molecular mechanisms underlying the complex cellular response induced by HF exposure, subsequent western blot analyses focused on proteins associated with hypoxic adaptation, stress-responsive signaling and regulation of tumour-associated pH homeostasis. Under hypoxic conditions, HF treatment increased Akt phosphorylation (Ser473) in both HT-29 and HCT 116 cells, suggesting activation of compensatory pro-survival signaling pathways in response to cellular stress (Figure 1). Interestingly, the kinetics of this response differed between the investigated cell lines. In HCT 116 cells, significantly increased Akt phosphorylation was detected already after 0.5 h exposure to 5 µM HF, whereas in HT-29 cells significant Akt activation became more pronounced after 2 h treatment. These findings suggest that Akt phosphorylation represents an early stress-associated response to HF exposure, with faster activation kinetics in HCT 116 cells. The biological effects of HF on Akt signaling appear to be strongly dependent on both cellular context and HF concentration. Similar increases in Akt phosphorylation have previously been observed following exposure to low micromolar HF concentrations in neuronal cellular systems. In PC12 cells, 1 µM HF activated Akt/GSK-3β signaling and exerted predominantly neuroprotective effects [10], supporting the possibility that subcytotoxic HF concentrations may induce adaptive rather than directly cytotoxic cellular responses.

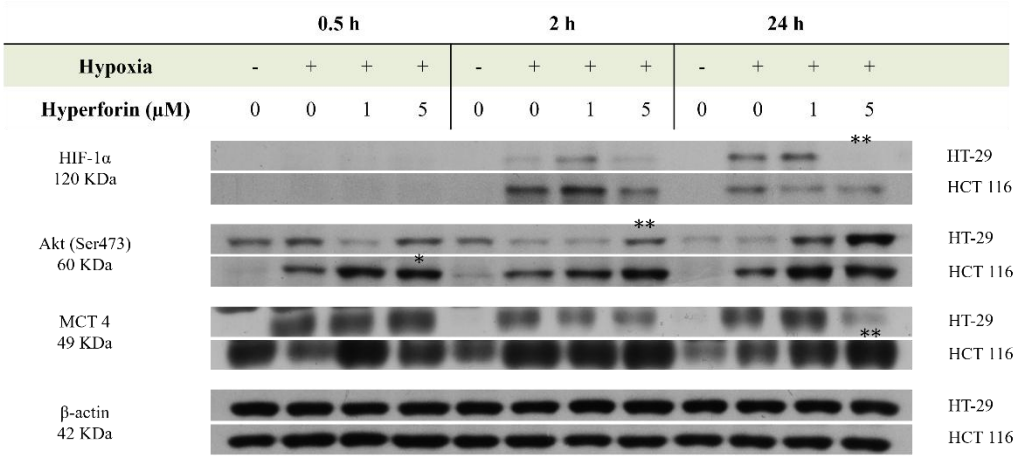

Figure 1. Effect of hyperforin (HF) on HIF-1α, phospho-Akt (Ser473) and MCT4 protein expression in HT-29 and HCT 116 colorectal cancer cells under hypoxic conditions. Cells were treated with 1 and 5 μM HF for 0.5, 2 and 24 h under hypoxia (1% O_2). Protein expression was analyzed by western blotting. β-actin was used as a loading control. Representative blots are shown. The groups treated with HF were compared with the untreated hypoxic control (* $p < 0.05$, ** $p < 0.01$, *** $p < 0.001$).

Conversely, higher micromolar HF doses have been associated with opposite effects on Akt signaling in several tumour models. In acute myeloid leukemia cells, exposure to approximately 2.5–15 μM HF suppressed PI3K/Akt signaling while simultaneously promoting mitochondrial dysfunction and activation of apoptotic pathways [8].

Similar effects were observed in colorectal cancer models, where HF treatment at concentrations 5-20 μM suppressed Akt, ERK1/2 and STAT3 phosphorylation while reducing migratory and invasive capacity and promoting apoptotic cell death [9].

Thus, the present findings indicate that under metabolically stressful hypoxic conditions, lower subcytotoxic HF concentrations may preferentially activate adaptive stress-associated pathways rather than directly inducing cytotoxic responses. Interestingly, prolonged HF exposure resulted in substantially different responses between the investigated colorectal cancer cell lines. Under hypoxic conditions, HCT 116 cells exhibited significantly increased MCT4 expression following 24 h exposure to 5 μM HF together with sustained Akt activation.

In contrast, HT-29 cells displayed a distinct temporal pattern, with significantly reduced HIF-1α protein levels after 24 h of HF exposure, whereas MCT4 expression tended to decrease but did not reach statistical significance. Importantly, no parallel increase in MCT4 expression was observed in HT-29 cells, in contrast to the response detected in HCT 116 cells. These findings indicate a cell line-dependent pattern of HF-induced adaptation and suggest that MCT4 regulation may not uniformly follow canonical HIF-1α-dependent control in colorectal cancer cells. Interestingly, reduced HIF-1α expression has previously been described predominantly for hypericin, another biologically active secondary metabolite of Hypericum perforatum L., whereas comparable effects of HF remain insufficiently characterized. The present findings

therefore suggest that HF may also alter hypoxia-associated pathways, potentially through indirect metabolic and pH-related mechanisms.

Persistent Akt activation together with delayed MCT4 upregulation in HCT 116 cells may therefore represent compensatory mechanisms attempting to preserve intracellular pH homeostasis and metabolic stability following prolonged HF-induced protonophoric stress. In contrast, the absence of significant MCT4 induction accompanied by reduced HIF-1α protein levels in HT-29 cells may indicate a less efficient adaptive response to prolonged metabolic stress induced by HF exposure.

Conclusion

Altogether, the present findings suggest that under hypoxic conditions, subcytotoxic HF concentrations may trigger adaptive rather than directly cytotoxic responses in colorectal cancer cells. The observed interplay between Akt activation, MCT4 regulation and altered hypoxia-associated signaling highlights the potential involvement of HF in modulation of metabolic and pH-associated adaptation pathways. These effects appear to be strongly dependent on tumour cell phenotype and microenvironmental context, emphasizing the complexity of HF-mediated responses in colorectal cancer cells. Better understanding of these context-dependent mechanisms may provide further insight into the potential therapeutic relevance of HF in modulation of tumour adaptation to hypoxic and metabolic stress.

Acknowledgement

This work was funded by the EU NextGenerationEU through the Recovery and Resilience Plan for Slovakia under the project No. 09I03-03-V05-00008

References

[1] Bakleh MZ, Al Haj Zen A. The distinct role of HIF-1α and HIF-2α in hypoxia and angiogenesis. Cells 2025; 14: 673. doi: 10.3390/cells14090673.

[2] Majerník M, Jendželovský R, Babinčák M, Košuth J, Ševc J. et al. Novel Insights into the effect of Hyperforin and Photodynamic Therapy with Hypericin on Chosen Angiogenic Factors in Colorectal Micro-Tumors Created on Chorioallantoic Membrane. Int J Mol Sci. 2019; 20: 3004. doi: 10.3390/ijms20123004.

[3] Imreova P, Feruszova J, Kyzek S, Bodnarova K, Zduriencikova M et al. Hyperforin Exhibits Antigenotoxic Activity on Human and Bacterial Cells. Molecules 2017; 22: 167. doi: 10.3390/molecules22010167.

[4] Liu YC, Lin KH, Hsieh JH, Chung JG, Tan ZL et al. Hyperforin Induces Apoptosis Through Extrinsic/Intrinsic Pathways and Inhibits NF-κB-modulated Survival and Invasion Potential in Bladder Cancer. In Vivo 2019; 33: 1865-1877. doi: 10.21873/invivo.11680.

[5] Cardile A, Zanrè V, Campagnari R, Asson F, Addo SS et al. Hyperforin Elicits Cytostatic/Cytotoxic Activity in Human Melanoma Cell Lines, Inhibiting Pro-Survival NF-κB, STAT3, AP1 Transcription Factors and the Expression of Functional Proteins Involved in Mitochondrial and Cytosolic Metabolism. Int J Mol Sci 2023; 24: 1263. doi: 10.3390/ijms24021263.

[6] Hostanska K, Reichling J, Bommer S, Weber M, Saller R. Hyperforin, a constituent of St John's wort (Hypericum perforatum L.) extract, induces apoptosis by triggering activation of caspases and with hypericin synergistically exerts cytotoxicity towards human malignant

cell lines. Eur J Pharm Biopharm 2003; 56: 121-132. doi: 10.1016/S0939-6411(03)00046-8.

[7] Donà M, Dell'Aica I, Pezzato E, Sartor L, Calabrese F et al. Hyperforin inhibits cancer invasion and metastasis. Cancer Res 2004; 64: 6225-6232. doi: 10.1158/0008-5472.CAN-04-0280.

[8] Merhi F, Tang R, Piedfer M, Mathieu J, Bombarda I et al. Hyperforin inhibits Akt1 kinase activity and promotes caspase-mediated apoptosis involving Bad and Noxa activation in human myeloid tumor cells. PLoS One 2011; 6: e25963. doi: 10.1371/journal.pone.0025963.

[9] Hsu LC, Kuo CY, Hsu FT, Chang HF, Ou JJ. Hyperforin Suppresses Oncogenic Kinases and Induces Apoptosis in Colorectal Cancer Cells. In Vivo 2023; 37: 182-189. doi: 10.21873/invivo.13067.

[10] Huang W, Cheng P, Yu K, Han Y, Song M et al. Hyperforin attenuates aluminum-induced Aβ production and Tau phosphorylation via regulating Akt/GSK-3β signaling pathway in PC12 cells. Biomed Pharmacother 2017; 96: 1-6. doi: 10.1016/j.biopha.2017.09.114.

ADCC ACTIVITY OF ELOTUZUMAB IN CHRONIC LYMPHOCYTIC LEUKEMIA CELL LINES

Dominik Kloc[1], Bianca Dubikova[1], Slavomir Kurhajec[2], Jan Sykora[3], Marek Sarissky[1]

[1]Department of Pharmacology, Faculty of Medicine, Pavol Jozef Safarik University in Kosice, Trieda SNP 1, 04011 Kosice, Slovakia
[2]Department of Pharmaceutical Technology, Pharmacognosy, and Botany, University of Veterinary Medicine and Pharmacy in Košice, Komenskeho 73, 04181 Kosice, Slovakia
[3]Department of Haematology and Oncohaematology, Faculty of Medicine, Pavol Jozef Safarik University in Kosice and Louis Pasteur University Hospital Kosice, Trieda SNP 1, 04011 Kosice, Slovakia

Introduction

Chronic lymphocytic leukemia (CLL) is one of the most common hematological malignancies in adults in Western countries. Despite the continuously expanding therapeutic options, CLL remains an incurable disease, highlighting the need to identify novel therapeutic targets [1]. One of potential therapeutic targets may be the SLAMF (signaling lymphocytic activation molecule family) receptors. The SLAMF family consists of nine surface receptors predominantly expressed on hematopoietic cells. These receptors are involved in the regulation of immune cell activation, cytotoxicity, and intercellular communication. Aberrant expression of SLAMF receptors in hematological malignancies suggests their role in disease pathogenesis as well as their potential therapeutic applicability [3,5]. Elotuzumab is a humanized anti-SLAMF7 monoclonal antibody approved for the treatment of multiple myeloma, whose principal mechanism of action involves the activation of NK cells and the induction of antibody-dependent cellular cytotoxicity (ADCC). The aim of this study was to evaluate the ability of elotuzumab to induce antibody-dependent cellular cytotoxicity (ADCC) in CLL cell lines.

Materials and methods

The study included six CLL cell lines: MEC-1, MEC-2, CI, HG-3, PGA-1, and WA-OSEL. The cell lines were first immunophenotypically characterized, and the expression of SLAMF receptors was quantitatively determined using the stain index (SI). ADCC was evaluated using a flow cytometry–based assay employing CFSE staining of target cells and detection of dead cells with 7-AAD. Peripheral blood mononuclear cells

(PBMCs), isolated from the peripheral blood of healthy volunteers by density gradient centrifugation, or immunomagnetically isolated unstimulated NK cells were used as effector cells. Effector and target cells were co-cultured at an effector-to-target ratio of 8:1 in the presence of elotuzumab (100 μg/mL), rituximab (100 μg/mL), or their combination for 4 hours. The percentage of ADCC was calculated as the difference between the proportion of CFSE+/7-AAD+ target cells in the presence of the antibody and spontaneous cell death in the absence of the antibody. For statistical analyses, SPSS software was used, and statistical significance was evaluated using the Mann–Whitney U test and paired Student's t-test.

Results

Immunophenotypic analysis confirmed that all analyzed cell lines reproduced the typical immunophenotypic features of CLL. The expression of SLAMF receptors was heterogeneous among the individual cell lines. The highest SLAMF7 expression was observed in the MEC-1 and MEC-2 cell lines, whereas the CI, HG-3, PGA-1, and WA-OSEL cell lines exhibited approx. 3-times lower levels of expression in terms of SI (Figure 1).

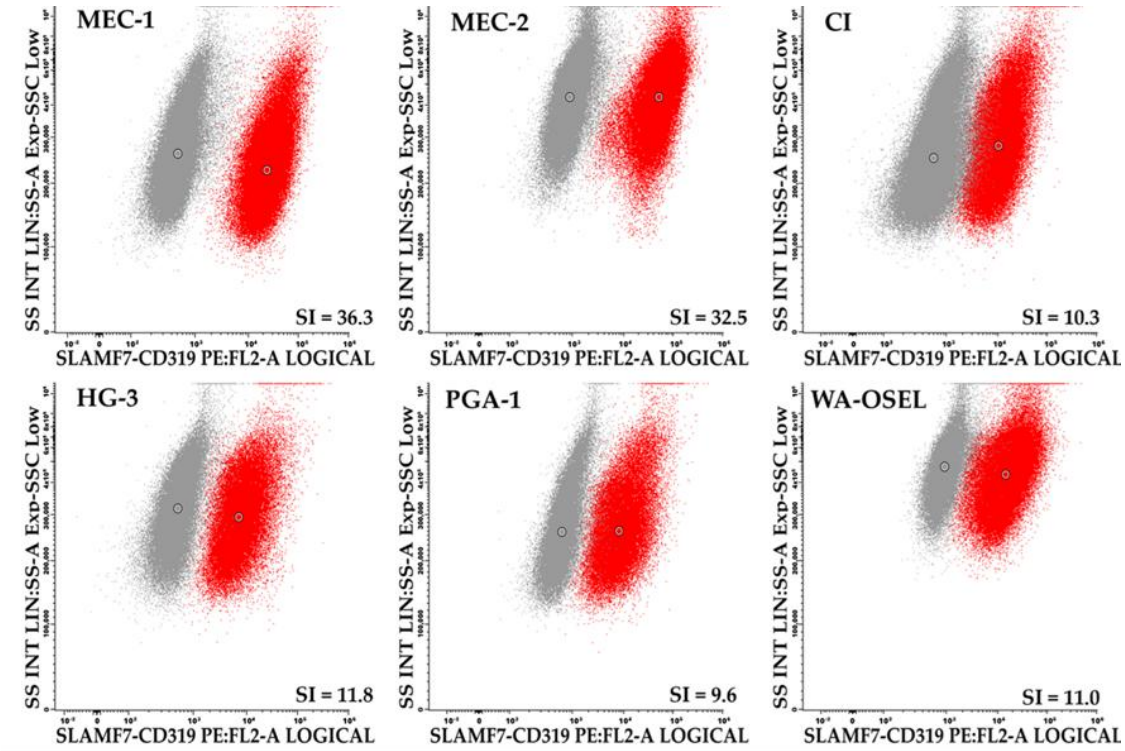

Figure 1: Expression of the SLAMF7 receptor in CLL cell lines. Grey dots: control unstained; red dots: cells stained with an anti-human SLAMF7-PE antibody

When PBMCs were used as effector cells, elotuzumab induced statistically significant ADCC in the MEC-1, MEC-2, HG-3, and WA-OSEL cell lines. The highest activity was observed in MEC-1 (14.6 ± 8.1%) and MEC-2 (10.5 ± 7.0%) cells. In contrast, the CI and PGA-1 cell lines exhibited minimal sensitivity to elotuzumab. Rituximab induced higher cytotoxicity in all analyzed cell lines except MEC-1, with ADCC values ranging from 9.2% to 18.0%. The combination of elotuzumab and rituximab did not result in a significant increase in cytotoxicity. When unstimulated NK cells were used as effector cells, a higher intensity of ADCC was observed compared with PBMCs. Elotuzumab achieved the highest activity in MEC-1 (27.3 ± 4.7%) and CI (17.2 ± 8.6%). Rituximab induced marked cytotoxicity particularly in the MEC-1, MEC-2, CI and HG-3 cell lines, where ADCC values exceeded 20%. Overall, NK cells proved to be more stronger effector cells for the induction of ADCC. The results of the ADCC analysis are summarized in Table 1.

Table 1: ADCC induced by elotuzumab, rituximab, and their combinations in CLL cell lines

Cell line	PBMC			NK cells		
	E	R	E + R	E	R	E + R
MEC-1	14.6 ± 8.1 $p < 0.01$	12.1 ± 7.2 $p < 0.01$	6.7 ± 5.4 $p < 0.05$	27.3 ± 4.7 $p = 0.01$	22.5 ± 14.0 NS	26.8 ± 9.2 $p < 0.05$
MEC-2	10.5 ± 7.0 $p < 0.05$	15.4 ± 9.1 $p < 0.05$	14.7 ± 12.2 NS	13.7 ± 5.5 $p < 0.05$	22.6 ± 6.9 $p < 0.01$	25.9 ± 12.9 $p < 0.05$
CI	1.8 ± 2.2 NS	14.1 ± 8.9 $p < 0.05$	5.1 ± 2.0 $p < 0.05$	17.2 ± 8.6 $p < 0.05$	27.5 ± 13.6 $p < 0.05$	29.0 ± 16.2 $p < 0.05$
HG-3	4.2 ± 2.5 $p < 0.05$	18.0 ± 6.9 $p < 0.01$	9.6 ± 3.9 $p < 0.05$	12.2 ± 8.5 NS	24.6 ± 7.2 $p < 0.01$	24.2 ± 12.3 $p < 0.05$
PGA-1	1.3 ± 1.2 NS	9.2 ± 4.6 $p < 0.01$	7.6 ± 3.9 $p < 0.05$	1.8 ± 3.7 NS	5.1 ± 4.3 NS	11.4 ± 9.5 NS
WA-OSEL	9.9 ± 2.7 $p < 0.001$	16.6 ± 9.4 $p < 0.05$	11.8 ± 7.0 $p < 0.05$	8.8 ± 10.4 NS	18.4 ± 5.1 $p < 0.01$	16. 4 ± 8.6 $p < 0.05$

Results are expressed as mean % ADCC ± SD. E, elotuzumab; R, rituximab; E + R, the combination of elotuzumab with rituximab. Statistically significant differences in the number of dead cells between control (target cells + effector cells) vs. treatment (target cells + effector cells + antibody/ies): $p < 0.001$; $p < 0.01$; $p < 0.05$; NS, non-significant.

Cell lines with higher SLAMF7 expression (MEC-1, MEC-2) showed stronger ADCC effect then cell lines with lower expression. In addition, cell lines carrying

chromosome 17p deletion (MEC-1, MEC-2, WA-OSEL) exhibited higher SLAMF7 expression compared with cell lines lacking this chromosome abnormality (Figure 2). However, a direct association between the 17p deletion and the intensity of ADCC was not observed. These findings suggest that the expression of the target antigen represents an important factor influencing the efficacy of elotuzumab.

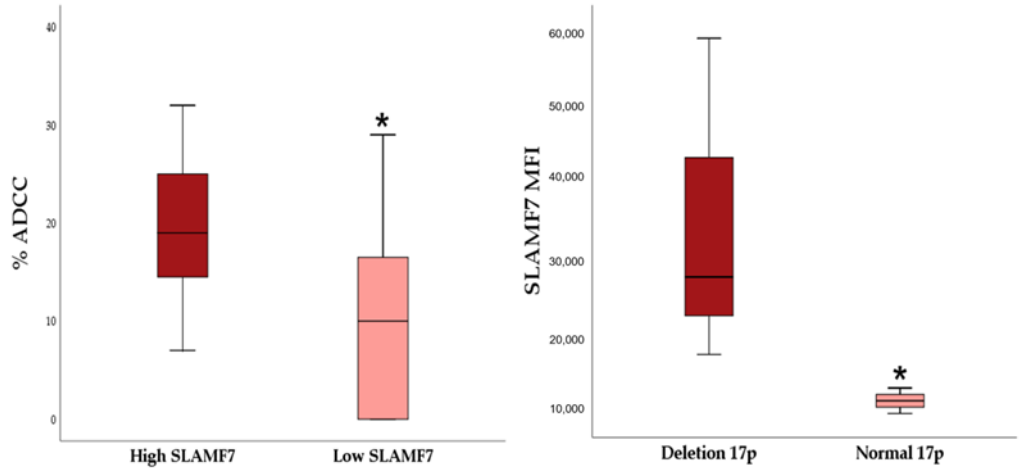

Figure 2: Relationships observed between SLAMF7 expression and % ADCC and the presence of 17p deletion

Discussion

In this study, we analyzed the ability of elotuzumab to induce ADCC against CLL cell lines. First, we comprehensively characterized all six cell lines in terms of their immunophenotype and SLAMF receptor expression. The expression of the imunophenotypic markers typical of CLL was generally consistent with previously published findings [1,2]. The immunophenotype of all six cell lines was generally compatible with the typical CLL phenotype. Compared with our previous results obtained in patients with CLL [3], the cell lines exhibited stronger expression of SLAMF1 and SLAMF7 and weaker expression of SLAMF5. An interesting finding was also the weak expression of SLAMF9 in the MEC-1, MEC-2, and WA-OSEL cell lines, which has not yet been described in the literature. Moderate to strong SLAMF7 expression provided the rationale for testing elotuzumab as a potential therapeutic agent in CLL. To evaluate ADCC, we employed a flow cytometry–based assay using PBMCs or immunomagnetically isolated unstimulated NK cells as effector cells. Elotuzumab induced significant ADCC against 5 out of 6 CLL cell lines (4.2–27.3% depending on the type of effector cells). The extent of ADCC was comparable to results reported in multiple myeloma models [4,5], although the maximal values were lower than those observed in MM cells with very high SLAMF7 expression. The MEC-1 and MEC-2 cell lines, which exhibited higher receptor expression, were more sensitive to elotuzumab-mediated ADCC than the CI, HG-3, PGA-1, and WA-OSEL cell lines with lower expression levels. A similar relationship between target antigen expression and the

efficacy of monoclonal antibodies has also been described for CD20 and rituximab [6,7]. In contrast, the expression of the adaptor proteins SAP and EAT-2 did not correlate with the intensity of ADCC. Another interesting observation was that cell lines carrying the 17p deletion exhibited higher SLAMF7/CD319 expression, which may suggest a role of p53 dysregulation in the regulation of SLAMF7 expression. Despite the lower expression of SLAMF receptors on CLL cells compared with MM cells, ADCC was still observed. This effect may be explained by another mechanisms of action of elotuzumab independent of CD16. Collins et al. [4] demonstrated that elotuzumab is capable of directly activating NK cells through binding to SLAMF7 receptors on their surface while simultaneously promoting interactions between NK cells and tumor cells. Generally, NK cells were stronger ADCC inducers than PBMCs, which is consistent with the findings of Beum et al. [8], who confirmed that NK cells represent the principal effector cells mediating ADCC within the PBMC population. The higher cytotoxicity of isolated NK cells is therefore likely related to their higher proportion among effector cells, whereas NK cells represent only a minor subset within PBMC populations when the same total number of effector cells is used.

The higher cytotoxicity of isolated NK cells is therefore likely related to the absence of other cellular populations present within PBMCs.

Conclusion

Elotuzumab induced ADCC in the majority of the tested CLL cell lines, with the intensity of the effect depending on SLAMF7 receptor expression and the type of effector cells used. NK cells exhibited higher cytotoxic activity than PBMCs. Although the effect of elotuzumab was generally weaker than that of rituximab, the results support the hypothesis that SLAMF7 may represent a potential therapeutic target in CLL.

References

[1] Mulligan SP, Tarn CS. Chronic lymphocytic leukemia: Diagnosis and clinical staging. Adv Treat B-Cell Chronic Lymphocytic Leukemia 2012: 7–15. doi:10.2217/EBO.11.280

[2] Detre C, Keszei M, Romero X, Tsokos GC, Terhorst C. SLAM family receptors and the SLAM-associated protein (SAP) modulate T cell functions. Semin Immunopathol 2010; 32: 157–171. doi:10.1007/s00281-009-0193-0

[3] Coma M, Tothova E, Guman T, Hajikova M, Giertlova M et al. Altered expression pattern of SLAM family receptors on pathological B cells of patients with chronic lymphocytic leukemia. Leuk Lymphoma 2017; 58: 1726–1729. doi:10.1080/10428194.2016.1251593

[4] Stacchini A, Aragno M, Vallario A, Alfarano A, Circosta P et al. MEC1 and MEC2: Two new cell lines derived from B-chronic lymphocytic leukaemia in prolymphocytoid transformation. Leuk Res 1999; 23: 127–136. doi:10.1016/S0145-2126(98)00154-4

[5] Lanemo Myhrinder A, Hellqvist E, Bergh AC, Jansson M, Nilsson K et al. Molecular characterization of neoplastic and normal “sister” lymphoblastoid B-cell lines from chronic lymphocytic leukemia. Leuk Lymphoma 2013; 54: 1769–1779. doi:10.3109/10428194.2013.764418

[6] Collins SM, Bakan CE, Swartzel GD, Hofmeister CC, Efebera YA et al. Elotuzumab directly enhances NK cell cytotoxicity against myeloma via CS1 ligation: Evidence for augmented NK cell function complementing ADCC. Cancer Immunol Immunother 2013; 62: 1841–1849. doi:10.1007/s00262-013-1493-8

[7] Pazina T, James AM, Colby KB, Yang Y, Gale A et al. Enhanced SLAMF7 homotypic interactions by elotuzumab improves NK cell killing of multiple myeloma. Cancer Immunol Res 2019; 7: 1633. doi:10.1158/2326-6066.CIR-18-0579

[8] Van Meerten T, Van Rijn RS, Hol S, Hagenbeek A, Ebeling SB. Complement-induced cell death by rituximab depends on CD20 expression level and acts complementary to antibody-dependent cellular cytotoxicity. Clin Cancer Res 2006; 12: 4027–4035. doi:10.1158/1078-0432.CCR-06-0066

[9] Golay J, Lazzari M, Facchinetti V, Bernasconi S, Borleri G et al. CD20 levels determine the in vitro susceptibility to rituximab and complement of B-cell chronic lymphocytic leukemia: further regulation by CD55 and CD59. Blood 2001; 98: 3383–3389. doi:10.1182/BLOOD.V98.12.3383

[10] Beum PV, Lindorfer MA, Taylor RP. Within peripheral blood mononuclear cells, antibody-dependent cellular cytotoxicity of rituximab-opsonized Daudi cells is promoted by NK cells and inhibited by monocytes due to shaving. J Immunol 2008; 181: 2916–2924. doi:10.4049/JIMMUNOL.181.4.2916

CHROMOGRANIN A AND ITS ROLE IN THE EPITHELIAL-MESENCHYMAL TRANSITION IN EARLY BREAST CANCER

Boris Lukac[1,2], Michal Mego[1,3], Lucia Kucerova[1,2]

[1]*Translational Research Unit, II. oncology clinic of LFUK and NCI, Bratislava, Slovak Republic*
[2]*Cancer Research Institute, Biomedical Research Center, Slovak Academy of Sciences, Bratislava, Slovak Republic*
[3]*II. oncology clinic of LFUK and NCI, Bratislava, Slovak republic*

Introduction

According to the International Agency on Cancer (IARC), in year 2020 breast cancer was the most commonly diagnosed type of cancer with 2,26 million cases worldwide; in 2022 the number of diagnosed cases rose to 2,31 million. Despite crucial breakthroughs in prevention, diagnostics and therapeutics of breast cancer, 5 15% of patients present with metastases at initial diagnosis, while 20-30% develop metastases along the course of the disease [1]. To execute invasive- metastatic cascade, epithelial cells need to detach from the primary tumor, invade the local tissue, intravasate into the peripheral circulation, survive during the hematogenous transit, extravasate at distant tissues and create micrometastatic colonies which eventually grow into new metastatic lesions [2]. Multiple types of cancer cells undergo the process of epithelial-mesenchymal transfer, in which the epithelial cells upregulate gene patterns typical for a mesenchymal phenotype, while downregulating genes typically associated with an epithelial phenotype. According to a study by Mego et al., 2019 which included 427 patients with primary breast cancer, disease free survival was significantly longer in patients without detectable CTC EMTs in peripheral blood based on an RT-qPCR expression analysis of EMT transcription factors [3]. Based on these findings, the occurrence of CTCs with an EMT phenotype was identified as a marker with prognostic value in early breast cancer. Furthermore, the study conducted by Zhang et al. in 2019 exploring the role of chromogranin A in neuroblastoma development concluded that striking alterations were observed after chromogranin A depletion in vitro with a marked phenotypic shift towards a mesenchymal phenotype and upregulation of mesenchymal markers (VIM and α-SMA) as well as ECM markers (FN and COL4A1) in neuroblastoma [4]. These findings further substantiate our hypothesis, which claims that there is a mechanistic link between chromogranin A and the epithelial-mesenchymal transfer (EMT) in breast cancer. The connection between CHGA and cancer was investigated in other types of cancer as well. Safarpour et al., 2024 used a holistic approach to finding connections between chromogranin A and colorectal carcinoma (CRC). Trough transcriptome and differential gene expression analyses several

candidate genes were identified, with downregulated CHGA being highlighted as notable in CRC development. A resultant RT-qPCR analysis confirmed CHGA downregulation in CRC tissues, matching the differential analysis findings and strengthening the hypothesis of its role in CRC development and aggressiveness. In the concluding remarks of this study, CHGA was described as a key gene in CRC development, describing it not only as a potential diagnostic marker, but also a hopeful therapeutic target [5].

Materials and Methods

For this study, we have a unique cohort of early breast cancer patient samples with complete clinical and pathological annotations in the biobank of the Translational Research Unit. The median monitoring time of these samples is 100 months. We utilized a diverse cell line panel for this study, consisting of the following lines; JIMT-1 (DSMZ id: ACC 589), BT20 (ATCC id: HTB-19), SK-BR-3 (ATCC id: HTB-30), T47-D (ATCC id: HTB-133), SUM149PT (CVCL id: 3422), MDA-MB-231 (ATCC id: HTB-26), MCF-7 (ATCC id: HTB 22) and MDA-MB-469 (ATCC id: HTB-132). The panel also includes circulating tumor cell lines CTC3 and LMC3 with an increased migration potential and altered gene expression profiles, derived from a triple-negative breast cancer cell line MDA-MB-231 [6]. Detection of biomarker gene expression was carried out using quantitative real-time PCR (RT-qPCR) using gene-specific TaqMan probes (TaqMan™ Gene Expression Assay, ThermoFisher Scientific, NY, USA; cat #4331182). The expression of CHGA was inhibited using short hairpin RNA (shRNA). shRNA was inserted into the cells trough lentiviral transduction using Chr-A shRNA (h) Lentiviral Particles: sc-37212-V (Santa Cruz Biotechnology, TX, USA). As a control of this reaction, we used Control shRNA Lentiviral Particles-A: sc-108080 (Santa Cruz Biotechnology, TX, USA) containing an shRNA sequence which doesn't lead to any known specific mRNA sequence degradation. Cells were transduced, expanded and selected by puromycin.

Results and Discussion

To validate our hypothesis, we started by selecting cell lines suitable for gene silencing based on their CHGA expression. Based on the RT-qPCR cell line screen we selected BT20, MCF-7 and SK-BR-3 for further experiments. Consequently, gene silencing was performed using lentiviral shRNA-mediated RNA interference, creating CHGA knock-down cell lines. The knock-down was validated using RT-qPCR at gene expression level and western blot at protein level. In order to test the effect of CHGA knock-down on EMT, we assessed the expression of EMT-associated transcription factors (TWIST1, SNAI2) and genes (CDH1, CDH2, VIM) using RT-qPCR and comparing expression results to control shRNA transduced cells. The results support our hypothesis, as mesenchymal markers (VIM, CDH2) were upregulated in all tested cell lines, while CDH1 as an epithelial marker was consistently downregulated. Transcription factors were deregulated on a somewhat non-consistent basis, which is a common occurrence in EMT, as transcription factors are redundant and interchangeable [7] Differences between knock-down cells and controls were also seen on a morphological level (Figure 1).

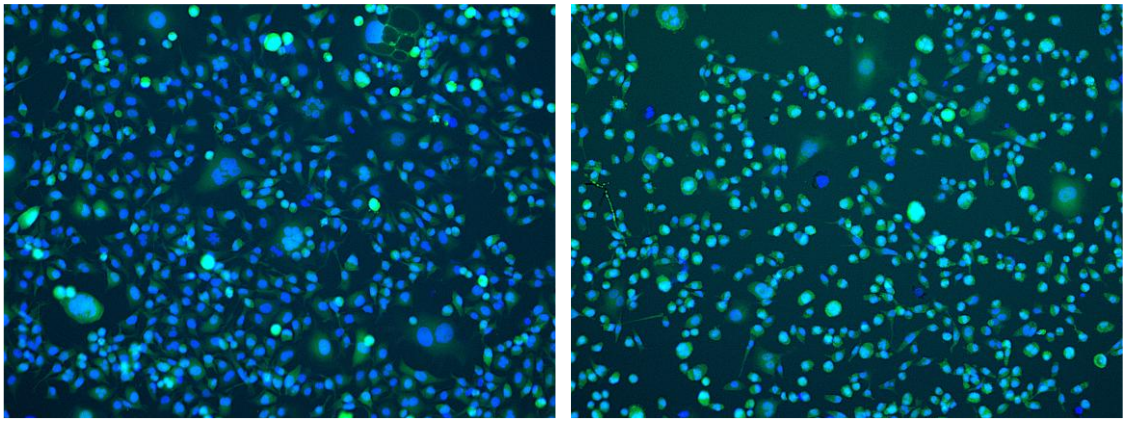

Figure 1. Morphology of knock-down BT20 cells (left) compared to control BT20 cells (right).

We then created an initial immunocompromised orthotopic mouse model using knock-down cells, in which tumor growth in the knock-down group significantly outperformed the control wild-type cell group (Figure 2). The bone marrow extracted from the models contained tumor cells, which also differed in morphology between the knock-down and control cells (Figure 3).

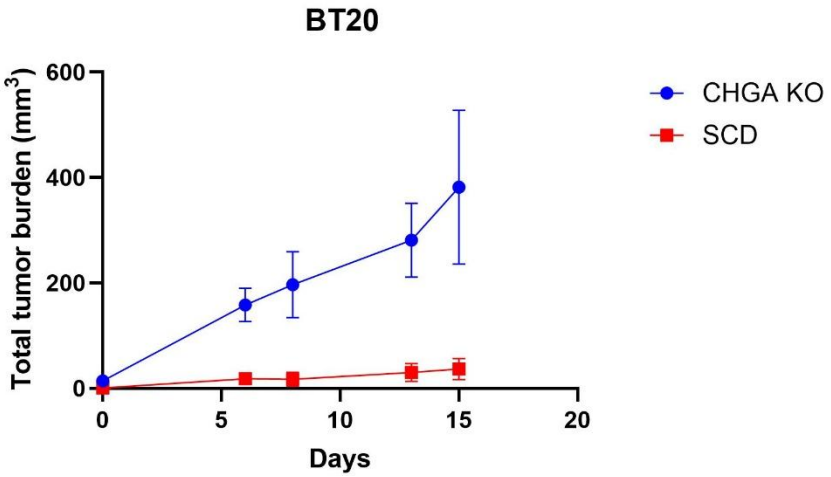

Figure 2. Total tumor burden of tested immunocompromised models.

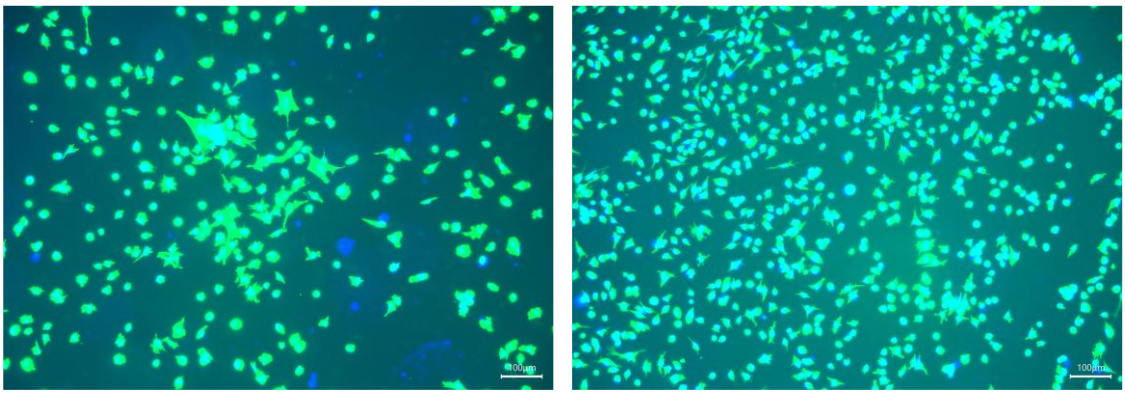

Figure 3. Cells extracted from the bone marrow of immunocompromised models. BT20 knock-down cells (left) exhibit a different morphology compared to the controls (right).

Conclusion

In conclusion, our experiments show that CHGA inhibition in breast cancer cell lines leads to a shift in cell morphology towards a mesenchymal phenotype. These findings suggest a role for CHGA in complex EMT regulation, although further experimental validation is required to support these claims.

Acknowledgement

This work was supported by the Slovak Research and Development Agency grant APVV-24-0333; Comenius University grant UK/1160/2025; Cancer Research Foundation, Bratislava and League Against Cancer, Bratislava.

References

[1] DeSantis, C. E., Fedewa, S. A., Goding Sauer, A., Kramer, J. L., Smith, R. A., & Jemal, A. (2016). Breast cancer statistics, 2015: Convergence of incidence rates between black and white women. CA: a cancer journal for clinicians, 66(1), 31-42.

[2] Fidler, I. J. (1970). Metastasis: quantitative analysis of distribution and fate of tumor emboli labeled with 125I-5-iodo-2′-deoxyuridine. Journal of the National Cancer Institute, 45(4), 773 782.

[3] Mego, M., Karaba, M., Minarik, G., Benca, J., Silvia, J., Sedlackova, T., ... & Mardiak, J. (2019). Circulating tumor cells with epithelial–to–mesenchymal transition phenotypes associated with inferior outcomes in primary breast cancer. Anticancer research, 39(4), 1829 1837.

[4] Zhang, D., Babayan, L., Ho, H., & Heaney, A. P. (2019). Chromogranin A regulates neuroblastoma proliferation and phenotype. Biology open, 8(3), bio036566.

[5] Safarpour, H., Ranjbaran, J., Erfanian, N., Nomiri, S., Derakhshani, A., Gerarduzzi, C., ... & Silvestris, N. (2024). Holistic exploration of CHGA and hsa-miR-137 in colorectal cancer via multi-omic data Integration. Heliyon, 10(5).

[6] Plava, J., Trnkova, L., Makovicky, P., Mego, M., Miklikova, S., & Kucerova, L. (2023). Novel model of triple-negative breast cancer produces viable circulating tumor cells and rapid lung metastasis for functional testing in vivo. Neoplasma, 70(4).

[7] Allgayer, Heike, et al. "Epithelial-to-mesenchymal transition (EMT) and cancer metastasis: the status quo of methods and experimental models 2025." Molecular Cancer 24.1 (2025): 167.

EGCG AS A POTENTIAL EPIGENETIC REGULATOR OF ALDH1 EXPRESSION AND REDOX HOMEOSTASIS IN COLORECTAL CANCER

Nikoleta Mojzesova, Zuzana Kozovska, Silvia Tyciakova, Martina Poturnajova, Katarina Kozics, Viera Horvathova Kajabova, Bozena Smolkova, Miroslava Matuskova

Cancer Research Institute, Biomedical Research Center of Slovak Academy of Sciences, Dubravska cesta 9, 845 05, Bratislava, Slovak Republic

Introduction

Colorectal cancer (CRC) is the second most common cancer worldwide [1]. Beyond the challenges of current treatments, there is a critical need to identify novel biomarkers to predict disease onset, progression, and therapeutic response. Our team has long been focused on the aldehyde dehydrogenase 1 (ALDH1) family, especially on 1A1 and 1A3 isoforms, a group of enzymes involved in several key cellular processes, including retinoic acid metabolism, aldehyde detoxification, and stem cell maintenance [2]. Derivation of the chemoresistant HT-29/EGP/FUR line from HT-29 resulted in a switch in the expression of ALDH1A1/1A3 isoforms, with ALDH1A3 being linked with increased chemoresistance and metastasis formation [3]. Next, we observed that ALDH1A1-knockout is associated with increased invasive capacity and metastatic potential [4].

Epigallocatechin 3-gallate (EGCG) is a natural compound found in green tea leaves, characterised by high accessibility, a favourable safety profile, and a long history of dietary exposure [5]. EGCG exerts antitumour effects through multiple mechanisms, including modulation of oxidative stress, induction of apoptosis, as well as regulation of signalling and epigenetic pathways [6]. For instance, it can influence DNA methylation, leading to global or locus-specific DNA hypomethylation [7].

In this study, we aimed to elucidate the role of EGCG in regulating ALDH1 expression and its impact on redox homeostasis, stem cell-like properties, and therapeutic sensitivity in CRC cells. The partial objectives of the work were to characterise the effect of EGCG on ALDH1 expression in CRC cells, to analyse the potential epigenetic mechanisms of ALDH1A3 regulation after EGCG exposure, to evaluate the anti- and pro-oxidant effects of EGCG in relation to ALDH1A3 expression, and to elucidate the potential role of ALDH1A3 in the response to EGCG.

Materials and methods

Cell lines and treatment

Cell lines pts80 [4] and HT-29 were used to monitor *ALDH1A1* expression after EGCG treatment. *ALDH1A3* expression was analysed in HCT 116, HT-29/EGFP/FUR [3] (referred to as FUR), and SW480 cell lines. To investigate the biological role of *ALDH1A3* in antioxidant mechanisms and in the cellular response to EGCG, an *ALDH1A3* knockout cell line (FUR/1A3-KO) was used. The cell line transduced with the empty vector (FUR/EV) served as a control. Cell cultures were treated with low doses (2 and 5 µg/ml) of Epicatechin gallate (EGCG, Sigma-Aldrich, Germany).

Methods.

The non-toxic concentrations of EGCG were determined by CellTiter-Glo® Luminescent Cell Viability Assay (Promega Corporation, USA). The antioxidant capacity of EGCG was assessed using a 2,2-Diphenyl-1-picrylhydrazyl (DPPH) assay. The expression of *ALDH1A1*, *ALDH1A3* and genes involved in DNA methylation was analysed by RT-qPCR Bio-Rad CFX96 real-time PCR detection system (Bio-Rad, USA), and the expression of ALDH1A3 at the protein level was detected by Western blot. To assess changes in DNA methylation, genome-wide methylation profiling was performed using the Infinium™ MethylationEPIC v2.0 BeadChip (Illumina, USA). Subsequently, methylation of the *ALDH1A3* promoter region was analysed by pyrosequencing. The antioxidant status of the cells was assessed using the Total Antioxidant Status (TAS) test (Randox, Antrim, United Kingdom) and by measuring reactive oxygen species (ROS) levels with the ROS-Glo™ H_2O_2 Assay (Promega Corporation, USA). Statistical analysis was performed by using GraphPad Prism. Data are represented as mean ± SD.

Results

First, we determined sub-toxic concentrations of EGCG and measured its antioxidant activity. Low concentrations of EGCG (2 and 5 µg/ml) were selected for subsequent experiments. Treatment with low-dose EGCG does not affect *ALDH1A1* expression (Figure 1A1, 1A2). In contrast, a transient increase in *ALDH1A3* mRNA (Figure 1B1, 1B2) and protein (Figure 1C) expression was detected, followed by a gradual decrease over time.

Based on these findings, we aimed to investigate the epigenetic mechanisms that may regulate ALDH1A3 expression following EGCG treatment. Genome-wide methylation profiling confirmed the global hypomethylating activity of EGCG and identified approximately 5% hypomethylation within the *ALDH1A3* promoter region (Figure 2A, 2B). Next, we further analysed the expression of genes associated with methylation (DNA methyltransferases, DNMTs) and DNA demethylation (Ten-eleven translocases, TETs). Results showed variable responses in the analysed cell lines. In parallel, analysis of *ALDH1A3* promoter methylation also did not show significant methylation alterations (Figure 2C).

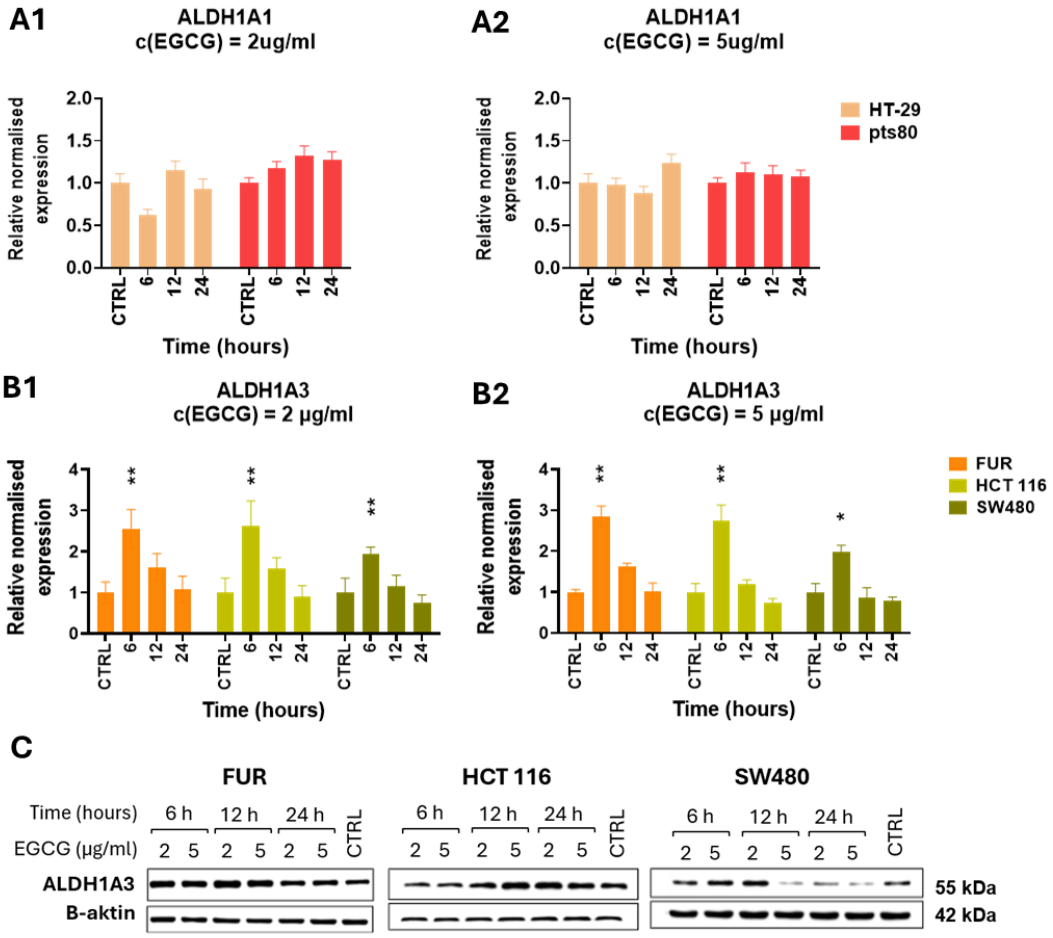

Figure 1: Effect of EGCG on the expression of A1: ALDH1A1, c(EGCG) = 2 (µg/ml) A2: ALDH1A1, c(EGCG) = 5 (µg/ml) and B1: ALDH1A3, c(EGCG) = 2 (µg/ml); B2: ALDH1A3, c(EGCG) = 5 (µg/ml) in CRC cells. Y-axis: Relative normalised expression; X-axis: Time (hours). C: ALDH1A3 protein expression after EGCG treatment.

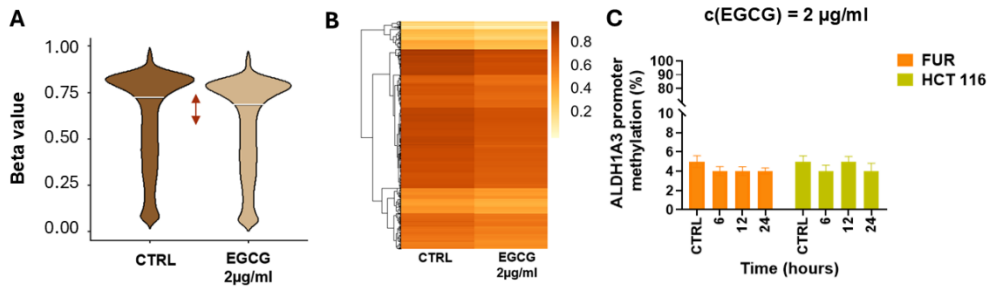

Figure 2: A: Violin plots illustrating β values of differently methylated probes (DMPs; adjusted p-value < 0.05). Y axis: β values; X axis: EGCG-treated vs control FUR cells, B: Heatmap illustrating global methylation patterns EGCG-treated versus control FUR cell line (CpGs with $|\Delta\beta| > 0.05$ and adjusted $p < 0.05$, excluding those located in open sea regions). C: ALDH1A3 promoter methylation in FUR and HCT 116 cells (control vs EGCG-treated). Y-axis: ALDH1A3 promoter methylation (%); X-axis: Time (hours).

To further investigate the role of *ALDH1A3* in cellular responses to EGCG, we evaluated its antioxidant effect in cells with high *ALDH1A3* expression compared to their *ALDH1A3* knockout counterparts. EGCG treatment did not influence total antioxidant activity in both parental and ALDH1A3-deficient cells (Figure 3A). However, cells lacking ALDH1A3 showed significantly reduced total antioxidant activity (Figure 3A). Following EGCG treatment, increased production of ROS was observed predominantly in *ALDH1A3* knockout cells, whereas parental cells did not exhibit ROS accumulation (Figure 3B).

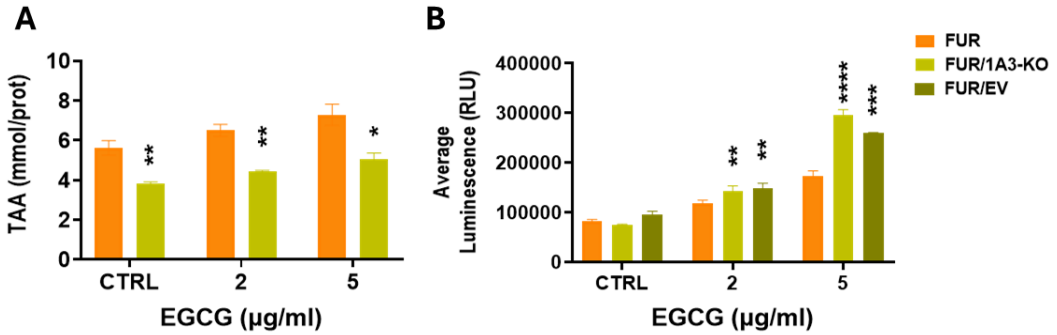

Figure 3: A: Total antioxidant activity of FUR parental and ALDH1A3 knockout cells. Y-axis: Total antioxidant activity (TAA) (mmol/prot); X-axis: EGCG (µg/ml). B: Intracellular ROS production after EGCG treatment. Y-axis: Average relative luminescence (RLU); X-axis: EGCG (µg/ml).

Discussion

The present study focused on the role and regulation of *ALDH1A3* in the context of EGCG treatment, with particular emphasis on epigenetic and antioxidant-related mechanisms. Our findings demonstrated that pharmacologically achievable low concentrations of EGCG [8] selectively modulated *ALDH1A3* expression, whereas *ALDH1A1* remained unaffected, suggesting that they are regulated by distinct mechanisms. Based on these observations, we hypothesised that EGCG may modulate *ALDH1A3* expression indirectly through epigenetic mechanisms. EGCG is known as a DNA demethylation agent [7]. We aimed to investigate whether this effect could be related to the altered *ALDH1A3* expression. Genome-wide methylation analysis confirmed a 5% global hypomethylation effect of EGCG, consistent with its previously published epigenetic activity [9]. Since increased gene expression can be associated with reduced methylation of promoter regions, we hypothesised that upregulation of *ALDH1A3* might be associated with hypomethylation of its promoter. However, subsequent analysis of gene expression associated with DNA methylation and demethylation yields heterogeneous results across individual cell lines. In parallel, pyrosequencing analysis of *ALDH1A3* promoter methylation did not detect significant changes after EGCG exposure. Our findings suggest that EGCG-mediated regulation of *ALDH1A3* expression is unlikely to occur through direct hypomethylation. However, the possibility of indirect epigenetic regulation remains, as EGCG is known to be a competitive inhibitor of DNMT enzymes [7,9], and its epigenetic effects may also be

mediated by other pathways. Further studies are needed to clarify the molecular mechanisms responsible for EGCG-mediated regulation of *ALDH1A3*.

Interesting results were observed in the analysis of antioxidant mechanisms. *ALDH1A3* knockout cells showed significantly reduced total antioxidant activity compared to parental cells. At the same time, low EGCG concentrations in these cells led to increased ROS production. EGCG can act as a pro-oxidant by generating ROS through auto-oxidation [10]. These observations suggest that *ALDH1A3* plays an important role in maintaining redox homeostasis and protecting tumour cells against oxidative stress. Based on this, we suggest that cells expressing *ALDH1A3* eliminate ROS more effectively, whereas cells deficient in *ALDH1A3* have impaired antioxidant defense mechanisms. Overall, these observations indicate that high *ALDH1A3* expression may be associated with reduced sensitivity of CRC cells to EGCG.

Conclusion

The aim of this study was to determine whether EGCG, a natural bioactive compound, can regulate *ALDH1A3* expression by epigenetic mechanisms, particularly DNA methylation. We revealed that EGCG modulates *ALDH1A3* expression in a time-dependent manner and induces global DNA hypomethylation. We showed that EGCG acts as a pro-oxidant in *ALDH1A3* knockout cells. In summary, this study highlights the possible role of *ALDH1A3* in the cellular response to EGCG treatment and also supports the therapeutic potential of natural compounds, which are generally cost-accessible and exhibit low toxicity toward non-tumour cells, where they primarily act as antioxidants.

Acknowledgement

This work was supported by the Slovak Research and Development Agency under the contract APVV-21 0296, by VEGA 2/0171/26, VEGA 2/0024/26, and by the Slovak Academy of Sciences through the DoktoGrant APP0447.

References

[1] Morgan E, Arnold M, Gini A, Lorenzoni V, Cabasag CJ, et al. Global burden of colorectal cancer in 2020 and 2040: incidence and mortality estimates from GLOBOCAN. Gut 2023; 72:338–344. doi:10.1136/gutjnl-2022-327736.

[2] Poturnajova M, Kozovska Z, Matuskova M. Aldehyde dehydrogenase 1A1 and 1A3 isoforms – mechanism of activation and regulation in cancer. Cell Signal 2021; 87:110120. doi:10.1016/j.cellsig.2021.110120.

[3] Durinikova E, Kozovska Z, Poturnajova M, Plava J, Cierna Z, et al. ALDH1A3 upregulation and spontaneous metastasis formation is associated with acquired chemoresistance in colorectal cancer cells. BMC Cancer 2018; 18:848. doi:10.1186/s12885-018-4758-y.

[4] Poturnajova M, Kozovska Z, Pos O, Pavlov K, et al. Genetic attenuation of ALDH1A1 increases metastatic potential and aggressiveness in colorectal cancer. Mol Oncol 2026. doi:10.1002/1878-0261.70215.

[5] Radeva-Ilieva M, Stoeva S, Hvarchanova N, Georgiev KD. Green tea: current knowledge and issues. Foods 2025; 14:745. doi:10.3390/foods14050745.

[6] Capasso L, De Masi L, Sirignano C, Maresca V, Basile A, et al. Epigallocatechin gallate (EGCG): pharmacological properties, biological activities and therapeutic potential. Molecules 2025; 30:654. doi:10.3390/molecules30030654.
[7] Li F, Qasim S, Li D, Dou QP. Updated review on green tea polyphenol epigallocatechin-3-gallate as a cancer epigenetic regulator. Semin Cancer Biol 2022; 83:335–352. doi:10.1016/j.semcancer.2020.11.018.
[8] Ullmann U, Haller J, Decourt JP, Girault N, Girault J, et al. A single ascending dose study of epigallocatechin gallate in healthy volunteers. J Int Med Res 2003; 31:88–101. doi:10.1177/147323000303100205.
[9] Agarwal A, Kansal V, Farooqi H, Prasad R, Singh VK. Epigallocatechin gallate (EGCG), an active phenolic compound of green tea, inhibits tumor growth of head and neck cancer cells by targeting DNA hypermethylation. Biomedicines 2023; 11:789. doi:10.3390/biomedicines11030789.
[10] Ouyang J, Zhu K, Liu Z, Huang J. Prooxidant effects of epigallocatechin-3-gallate in health benefits and potential adverse effect. Oxid Med Cell Longev 2020; 2020:9723686. doi:10.1155/2020/9723686.

A NOVEL CAIX–P-SELECTIN INTERACTION ENHANCES METASTATIC POTENTIAL VIA PLATELET COATING OF CTCS

Katarina Scasna[1], Lubor Borsig[2], Magdalena Baratova[1], Lucia Skvarkova[1], Eliska Svastova[1]

[1]*Institute of Virology, Biomedical Research Center, Slovak Academy of Sciences, Slovakia*
[2]*Institute of Physiology, University of Zurich, Switzerland*

Introduction

Hypoxic tumor cells frequently rely on glycolytic metabolism, resulting in the accumulation of acidic intracellular metabolites. In response to hypoxia, the expression of carbonic anhydrase IX (CAIX) is induced to maintain intracellular pH homeostasis [1]. Elevated CAIX expression is localized at the invadopodia of invasive tumor cells, thereby promoting intravasation during the metastatic cascade [2]. Through permeable and unstable neovasculature, tumor cells can enter the bloodstream either as single cells or heterogeneous clusters originating from hypoxic tumor regions [3]. These circulating tumor cells (CTCs) are associated with poor patient prognosis, and CAIX expression has been detected in CTCs derived from patients with renal and breast cancer [4-5].

We hypothesized that P-selectin may represent a novel interaction partner for CAIX due to its unique proteoglycan-like domain. Interaction of CAIX-positive CTCs with platelet P-selectin may promote their survival in the bloodstream.

Materials and methods

In silico analysis

A dataset consisting of 67 highly expressed surface proteins of human platelets was compiled [6]. Predicted three-dimensional structures of these proteins were obtained from the AlphaFold Protein Structure Database [7]. Protein structural models were subsequently modified using UCSF Chimera (University of California, San Francisco), and only the extracellular domains of the proteins were included in the simulations. The modified structural models of platelet proteins were subsequently uploaded to the HDOCK Server [8], where blind docking simulations were performed. The software evaluated potential interaction sites between the modified structural models of platelet proteins and the structural model of human CAIX without predefined binding sites.

Cell Culture

The tumor cell lines C33 (derived from cervical carcinoma) and HCT116 (derived from colorectal carcinoma), as well as the CA9-stably transfected cell lines C33-FLCAIX,

C33-dPG, C33-dCA, and HCT116-FLCAIX, were used in this study. Tumor cell lines were cultured in dishes containing Dulbecco's Modified Eagle Medium (DMEM) supplemented with 10% fetal calf serum (FCS) and 0.1% gentamicin under standard culture conditions (21% O_2, 5% CO_2, 37 °C).

Flow Cytometry

To assess the presence of selectin ligands on tumor cells, chimeric P-selectin fused to the Fc region of human IgG was used (provided by Dr. Borsig). Pre-complexes of selectin chimera were prepared by pre-incubating P-selectin chimera (10 µg/mL) with goat anti-human antibody conjugated with Alexa Fluor™ 488 (Thermo Fisher Scientific) to a final concentration of 15 µg/mL in 1% BSA in Hanks' balanced salt solution (HBSS) for 1 h at 4 °C on a rotator before addition to the cell suspension. C33 tumor cells in suspension were counted, kept on ice, and incubated with pre-complexed selectin chimeras for 1 h at 4 °C on a rotator. Following incubation, cells were washed with HBSS and subsequently stained for 15 min at 4 °C with primary anti-CAIX antibodies (M75 and Ab10) diluted 1:1000 in HBSS containing 1% BSA. Cells were then washed with HBSS and incubated with donkey anti-mouse antibody conjugated with Alexa Fluor™ 647 for 15 min at 4 °C (1:1000 dilution in HBSS containing 1% BSA). After the final wash with HBSS, labeled samples were analyzed using a NovoCyte Advanteon flow cytometer (Agilent Technologies).

Immunofluorescence and Confocal Microscopy

C33 cells grown on glass coverslips were fixed in 4% PFA solution at 20 °C for 10 min. Nonspecific binding was blocked with PBS containing 3% BSA for 30 min at 37 °C. Cells were subsequently incubated for 1 h with pre-complexes prepared in the same manner as for flow cytometry using P-selectin chimera (10 µg/mL). The cells were then washed three times with HBSS. Alexa Fluor™ 647-conjugated anti-CAIX antibody Ab10 diluted in 1% BSA-HBSS was subsequently added and incubated for 1 h at 37 °C. After three 10 min washes with HBSS, nuclei were stained with DAPI (1:1000 in PBS), followed by three additional washes with PBS. Finally, the samples were mounted onto slides using Fluorescent Mounting Medium and analyzed by confocal microscopy using the Zeiss LSM 900.

Results and discussion

For the in silico analysis pipeline, a total of 67 highly expressed platelet surface proteins were selected. Their corresponding structures were downloaded in PDB format and processed to retain only the extracellular domains. These prepared protein structures were subsequently used for CAIX interaction simulations performed using the HDOCK server (Fig. 1A). For each analyzed protein, the HDOCK server generated the top 10 interaction models ranked according to the HDOCK score, which estimates the theoretical binding affinity between two proteins. For comparison, 25 proteins with representative HDOCK scores were selected and visualized in a heatmap. Proteins such as integrin α2, integrin β1, and integrin α2b achieved HDOCK scores ranging from −250 to −300, indicating a predicted strong to very strong binding affinity (Fig. 1B). Since interactions between these proteins and CAIX have already been experimentally validated, they are considered established biological interaction partners of CAIX [9].

The presence of these proteins in the dataset, therefore, served as an internal validation of the simulation approach. Based on HDOCK score results remaining proteins, P-selectin was selected for further analysis because its predicted interaction models reached HDOCK scores comparable to those observed for integrins α2 and β1.

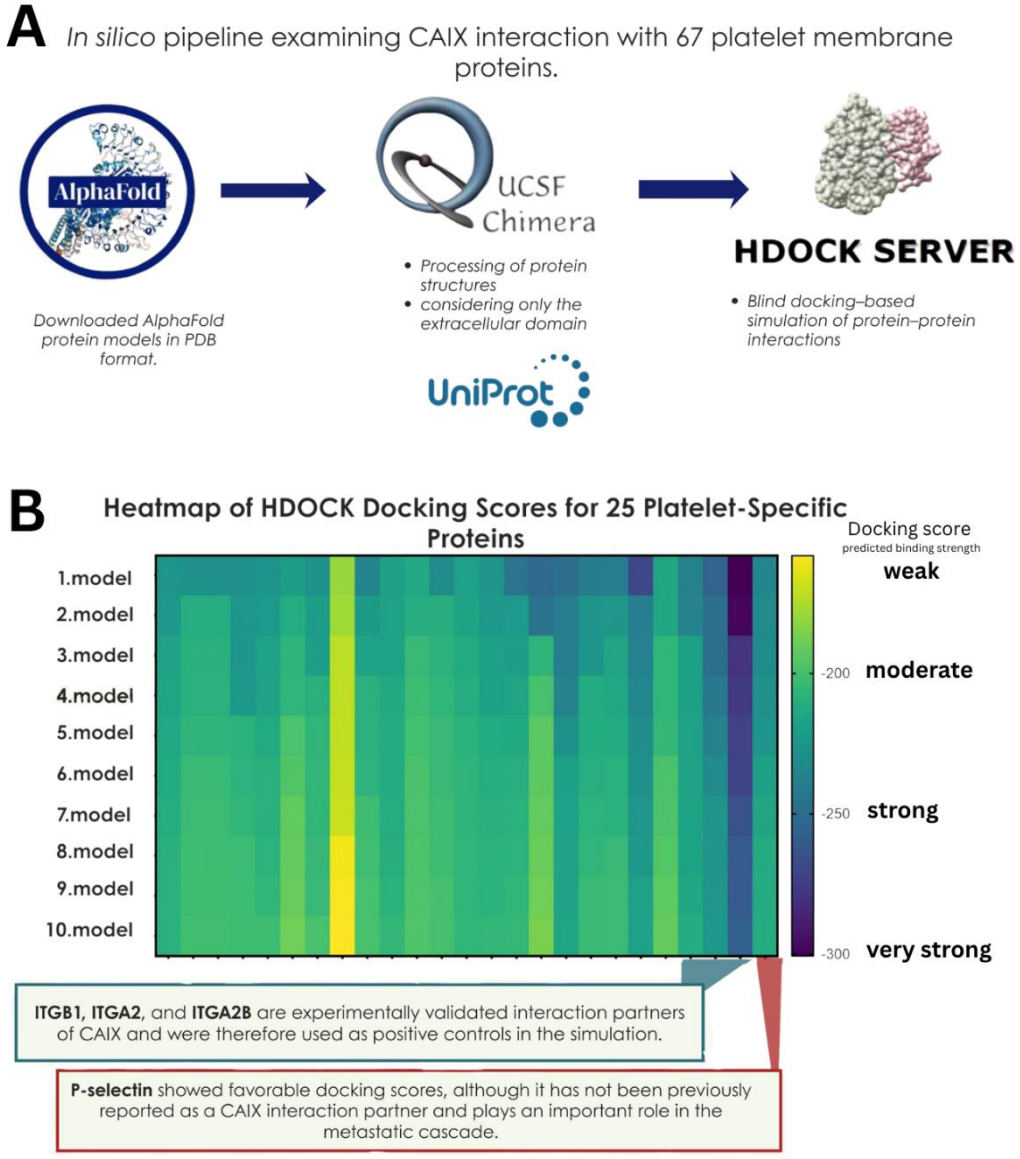

Figure 1 A) In silico workflow for prediction of CAIX interactions with platelet membrane proteins. B) Heatmap of docking score values for 25 selected platelet surface proteins following simulated interaction with the CA9 protein. The HDOCK server selected the 10 best interaction models ranked according to the lowest docking score values. Proteins with docking scores ranging from approximately −250 (dark green color) to −300 (dark blue color) demonstrated predicted strong to very strong binding potential toward the CA9 protein.

The ability of P-selectin to bind CAIX-positive tumor cells was evaluated using chimeric P-selectin precomplexes. C33-FLCAIX cells preferentially bound higher

amounts of P-selectin precomplexes compared to C33-neo cells lacking CAIX expression. Colocalization of both fluorescent signals was observed and is represented by the yellow signal in (Fig. 2A).

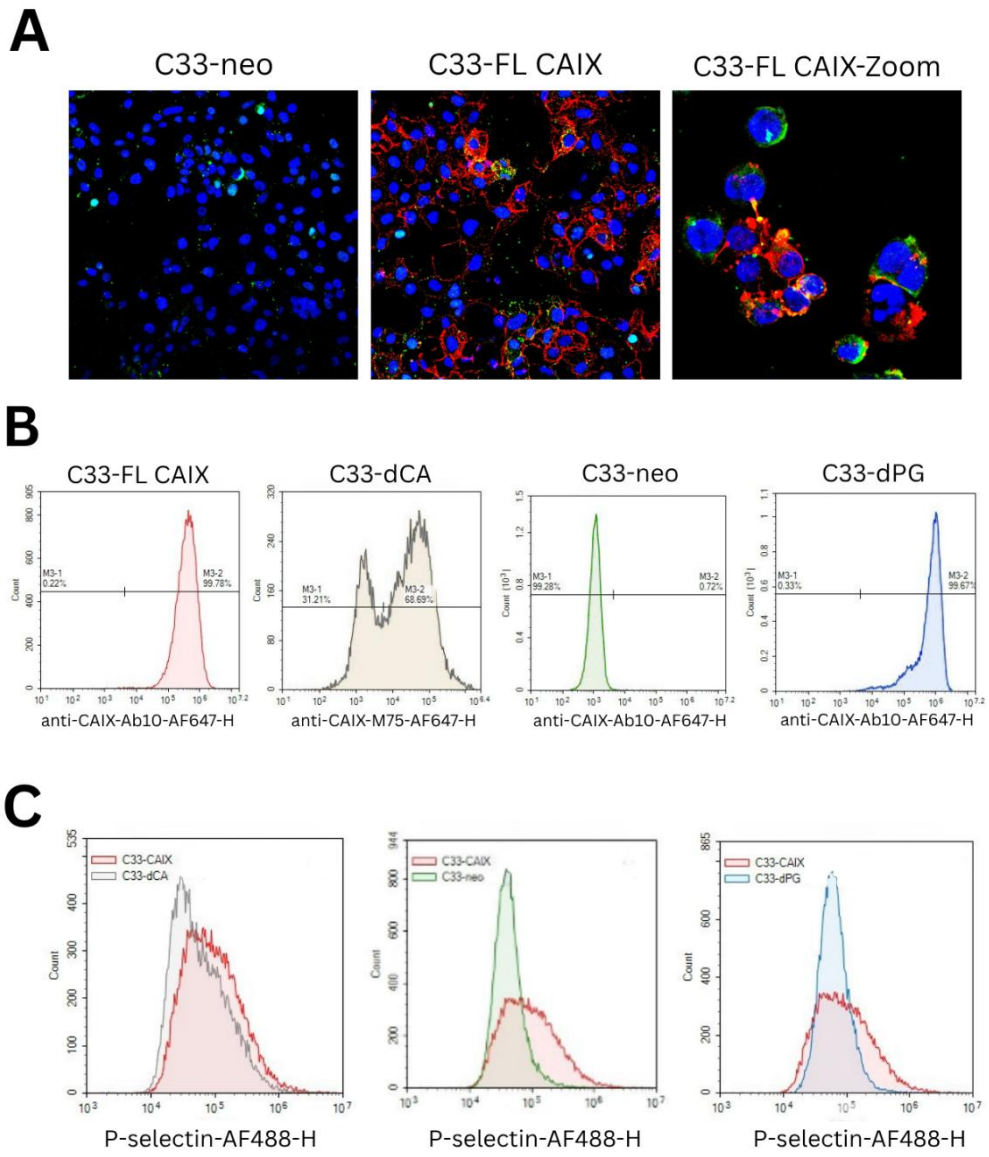

Figure 2 A) Preferential binding of P-selectins to C33-CAIX cells and identified colocalization of fluorescent signals. CAIX fluorescence (red) and P-selectin precomplex fluorescence (green) were detected in C33 cells. Increased binding of P-selectin was observed in C33-CAIX cells compared to C33-neo cells. In the C33-CAIX-Zoom images, colocalization of CAIX and P-selectin precomplex fluorescent signals was identified. Images were acquired using confocal microscopy (Zeiss LSM 900) with a 40x objective. **B) The histogram shows the proportion of CAIX-positive cells within the C33 cell population. C) Histograms illustrate the proportion of tumor cells positive for P-selectin across C33 cell variants (neo, CAIX, dPG, and dCA).** C33-CAIX cells (red) exhibited the highest proportion of P-selectin–positive cells, whereas ΔPG cells showed minimal positivity, similar to neo cells.

To identify the CAIX domain potentially responsible for this interaction, C33-dPG cells lacking the proteoglycan (PG) domain and C33-dCA cells lacking the catalytic

domain were generated. While C33-neo cells were negative for CAIX expression, both C33-dPG and C33-FLCAIX cells exhibited high CAIX positivity approaching 100% of cells. In contrast, the C33-dCA mutant showed a reduced proportion of CAIX-positive cells, with only 68.69% positivity (Fig. 2B). Enhanced P-selectin binding was observed in both FLCAIX and dCA-C33 cells, which displayed similar histogram distributions. In contrast, histograms of neo and C33-dPG cells displayed a shift toward lower fluorescence intensities, corresponding to reduced P-selectin binding compared to C33-FLCAIX cells (Fig. 2C). Based on these findings, we hypothesize that the P-selectin binding site is localized within the PG domain of CAIX. This region may undergo O-glycosylation and subsequent modification by sialyl Lewis antigens, which can be recognized by the C-type lectin domain of selectins. Selectins are known to interact with tumor cells through their C-type lectin domain by recognizing glycosylated mucin-like ligands [10].

Conclusion

In silico analysis demonstrated that CAIX is theoretically capable of interacting with multiple platelet adhesion proteins involved in platelet activation and interactions with vascular endothelial cells. Among the identified candidates, the interaction between CAIX and P-selectin was further supported by experiments using a chimeric P-selectin construct. The fluorescent signal of the P-selectin chimera colocalized with CAIX and showed enhanced binding to CAIX-positive cells compared to neo control cells. In addition, deletion of the PG domain markedly reduced the P-selectin-positive cell population, suggesting that the interaction site is likely localized within the PG domain of CAIX. Collectively, our findings suggest that CAIX-expressing CTCs may possess a selective advantage over CAIX-negative CTCs due to their enhanced ability to interact with platelets, potentially promoting their survival in the bloodstream and increasing their metastatic potential.

Acknowledgement

Funded by the EU NextGenerationEU through the Recovery and Resilience Plan for Slovakia under the project 09I03-03-V04-00444

References

[1] Benej M, Svastova E, Banova R, Kopacek J, Gibadulinova A, et al. CA IX stabilizes intracellular pH to maintain metabolic reprogramming and proliferation in hypoxia. Front Oncol 2020; 10: 1462-1462. doi: 10.3389/fonc.2020.01462.

[2] Svastova E, Witarski W, Csaderova L, Kosik I, Skvarkova L, et al. Carbonic anhydrase IX interacts with bicarbonate transporters in lamellipodia and increases cell migration via its catalytic domain. J Biol Chem 2012; 287: 3392-3402. doi: 10.1074/jbc.M111.286062.

[3] Aceto N, Bardia A, Miyamoto DT, Donaldson MC, Wittner BS, et al. Circulating tumor cell clusters are oligoclonal precursors of breast cancer metastasis. Cell 2014; 158: 1110-1122. doi: 10.1016/j.cell.2014.07.013.

[4] Takacova M, Bartosova M, Skvarkova L, Zatovicova M, Vidlickova I, et al. Carbonic anhydrase IX is a clinically significant tissue and serum biomarker associated with renal cell carcinoma. Oncol Lett 2013; 5: 191-197. doi: 10.3892/ol.2012.1001.

[5] Twomey JD, Zhang B. Exploring the role of hypoxia-inducible carbonic anhydrase IX (CAIX) in circulating tumor cells (CTCs) of breast cancer. Biomedicines 2023; 11: 934-934. doi: 10.3390/biomedicines11030934.
[6] PlateletWeb, Platelet protein expression database. https://plateletweb.bioapps.biozentrum.uni-wuerzburg.de/plateletweb.php, 2025 (accessed January 2026).
[7] AlphaFold Protein Structure Database. https://alphafold.ebi.ac.uk/, 2025 (accessed January 2026).
[8] HDOCK Server for Protein-Protein and Protein-DNA/RNA Docking. http://hdock.phys.hust.edu.cn/, 2025 (accessed January 2026).
[9] Swayampakula M, McDonald PC, Vallejo M, Coyaud E, Chafe SC, et al. The interactome of metabolic enzyme carbonic anhydrase IX reveals novel roles in tumor cell migration and invadopodia/MMP14-mediated invasion. Oncogene 2017; 36: 6244–6261. doi: 10.1038/onc.2017.219.
[10] Borsig L, Wong R, Hynes RO, Varki NM, Varki A. Synergistic effects of L- and P-selectin in facilitating tumor metastasis can involve non-mucin ligands and implicate leukocytes as enhancers of metastasis. Proc Natl Acad Sci U S A 2002; 99: 2193-2198. doi: 10.1073/pnas.261704098.

THE SPECIFICITY OF CONDITIONAL MEDIUM EXOSOMES PRODUCED FROM DIFFERENT TYPES OF MESENCHYMAL STEM CELLS THAT HAVE BEEN TRANSDUCED WITH SUICIDE GENES FOR GASTROINTESTINAL CANCERS

Dajana Vanova[1,2], Ursula Altanerova[2], Michal Andrezal[2], Miroslava Matuskova[1], Cestmir Altaner[1,2]

[1]*Cancer Research Institute, Biomedical Research Center, Slovak Academy of Sciences, Bratislava, Slovakia*
[2]*Stem Cell Preparation Department, St. Elisabeth Cancer Institute, Bratislava, Slovakia*

Introduction

Mesenchymal stem cell (MSC) are pluripotent stem cells characterized by their ability to proliferate, self-renew, migrate to target tissues, and exhibit low immunogenicity. They can be obtained from multiple tissue sources such as bone marrow, adipose tissue, dental pulp, umbilical cord, and placenta. Owing to these properties, MSCs have become attractive candidates for applications in regenerative medicine and gene-based cancer therapies. Nearly all cell types release exosomes, which are small membrane-bound extracellular vesicles composed of specific proteins, lipids, nucleic acids, and glycoconjugates. In recent years, exosomes have attracted considerable attention due to their high biocompatibility, stability, low immunogenicity, and ability to cross biological barriers. These characteristics make them promising natural nanocarriers for targeted drug and gene delivery in cancer treatment [1-3].

Gastrointestinal cancer is among the most common malignancies, characterized by a high tendency to metastasize and has a significant impact on mortality rates. Unfortunately, these tumors are often not diagnosed until they have reached an advanced stage, at which point metastases may already be present, and standard treatment is of limited effectiveness in such cases. In particular, systemic administration of chemotherapeutic agents is associated with considerable toxicity and lack of tumor selectivity [4]. Suicide gene therapy, also known as gene-directed enzyme prodrug therapy (GDEPT), offers a strategy to overcome these limitations. This approach is based on the introduction of a gene encoding a specific enzyme into tumor-targeting cells, enabling the local conversion of a non-toxic prodrug into a cytotoxic compound directly within the tumor microenvironment. One of the most extensively studied systems is the cytosine deaminase/5-fluorocytosine (CD/5-FC) system, in which the enzyme converts 5-fluorocytosine (5-FC) into the cytotoxic drug 5-fluorouracil (5-FU), generating a strong bystander effect that enhances tumor cell killing [5].

Although MSC-based delivery of suicide genes and the therapeutic potential of exosomes have been investigated separately, the use of MSC-derived exosomes carrying

a suicide gene system for targeted therapy of gastrointestinal cancers has not yet been sufficiently explored.

In this study, we evaluated the tumor type specificity of suicide gene exosomes found in the conditioned media (CM) of five types of *yCD::UPRT* gene transduced stromal cells. The tumor cell killing efficacy of CMs obtained from the following cell types: *yCD::UPRT*-DP-MSCs, *yCD::UPRT*-UC-MSCs, *yCD::UPRT*-AT-MSCs, *yCD::UPRT*-Plac-MSCs, and *yCD::UPRT*-BM-MSCs was analyzed. The targeting specificity of these conditioned media was tested in gastrointestinal cell lines MIA PaCa-2 (pancreatic adenocarcinoma), AGS (gastric adenocarcinoma), and Caco-2 (colorectal adenocarcinoma) in a dose-dependent manner. The data obtained indicate a high universal therapeutic effectiveness of *yCD::UPRT*-MSC-CM, irrespective of the types of cancer. The tissue origin of MSCs influences the therapeutic potency of their secreted exosomes. The exosomes from the suicide gene possess potential for preventing metastasis [6].

Materials and methods

Isolation and culture of mesenchymal stromal cells (MSCs)

Mesenchymal stromal cells were isolated from dental pulp (DP), umbilical cord (UC), adipose tissue (AT), placenta (Plac), and bone marrow (BM). The isolated cells were cultured in low-glucose DMEM (LG DMEM) (Gibco, Thermo Fisher Scientific) supplemented with 5% platelet lysate (PL). Cultivation took place in an incubator at 37 °C, 95% humidity, and 5% CO_2. Upon reaching the desired confluence, the cells were passaged and replated into culture dishes at a density of 5×10^5 cells per dish. The culture medium was changed every three days.

Retroviral transduction of MSCs

MSCs derived from DP, UC, AT, Plac, and BM were transduced with a yeast retroviral vector carrying the *yCD::UPRT* fusion gene. The cells were infected three times with replication-defective retrovirus with mixed amphotropic and ecotropic envelope glycoproteins in the presence of protamine sulfate (100 μg/mL). The recombinant retrovirus possessing the *yCD::UPRT* gene was prepared as described in details previously [7]. The antibiotic G418 (400 μg/mL) was used to select a homogeneous population of transduced cells. Conditioned medium was obtained from this cell population by harvesting the culture medium (LG DMEM) without the addition of PL.

Cultivation of tumor cell lines

The effect of conditioned media was tested on three human tumor cell lines: MIA PaCa-2, AGS, and Caco-2. The cells were cultured in high-glucose (HG DMEM) supplemented with 5 % fetal bovine serum (FBS; Biosera) at 37 °C, 95% humidity, and 5% CO_2. Once high confluence was reached, the cells were passaged and seeded into 96-well microtiter plates at a density of 3×10^3 cells per well.

Application of conditioned medium and viability assessment

On the second day after seeding, conditioned medium from transduced MSCs (DP, UC, AT, Plac, BM) was added to individual cell lines in volumes of 100, 50, 25, and 12.5 μL, both in the presence and absence of the prodrug 5-FC. Cell viability was assessed on day 4 using the MTT assay. All donors of adipose tissue, bone marrow, and other

tissue specimens used for isolation and propagation of MSCs were informed about the nature of the study, and provided their written informed consent. The Ethical committee of the St. Elisabeth Cancer Institute approved all experimental protocols involving cells of human subjects (No. 4-2019/EK OUSA).

Results

The efficacy of conditioned medium from *yCD::UPRT*-DP, *yCD::UPRT*-UC, *yCD::UPRT*-AT, *yCD::UPRT*-Plac, and *yCD::UPRT*-BM was evaluated in three gastrointestinal cell lines: MIA PaCa-2, AGS, and Caco-2. Cells were exposed to various concentrations of CM for 4 days. Cell viability was determined using the MTT assay. Samples with the addition of the prodrug 5-FC are indicated by pink bars in the graphs, while samples without 5-FC are indicated by green bars. All values were compared to the control (LG DMEM). Statistical significance was assessed using the LSD ANOVA test ($p < 0.05$). In the MIA PaCa-2 cell line, a dose-dependent decrease in cell viability was observed following the application of CM in combination with 5-FC. A statistically significant the most cytotoxic effect was observed with CM from *yCD::UPRT*-DP, *yCD::UPRT*-UC, *yCD::UPRT*-AT, and *yCD::UPRT*-Plac (highlighted). With CM from *yCD::UPRT*-BM, higher cell viability was observed as the CM dose decreased. Samples without the addition of 5-FC showed higher viability in all cases compared to samples with 5-FC (Fig. 1).

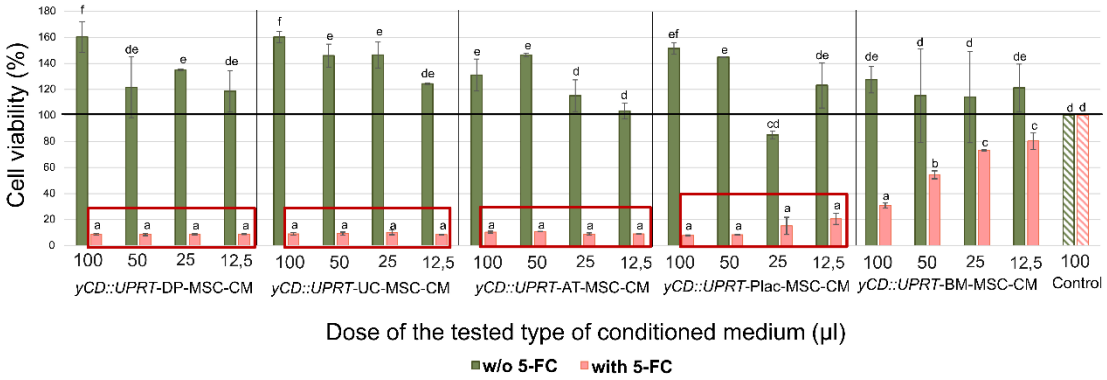

Figure 1. Types of *yCD:UPRT* conditioned medium tested on cell line derived from pancreatic ductal adenocarcinoma. Cell viability was determined using the MTT test after exposure for 4 days. *yCD::UPRT*-DP-MSC-CM, *yCD::UPRT*-UC-MSC-CM, *yCD::UPRT*-Plac-MSC-CM, *yCD::UPRT*-BM-MSC-CM. Control – tested cancer cells grown in the DMEM culture medium. The statistical significance was determined using the LSD ANOVA statistical test ($P < 0.05$). Columns marked with different letters indicate statistically significant differences, while columns sharing the same letter are not significantly different.

A similar trend was observed in the AGS cell line. Cells exposed to CM from *yCD::UPRT*-DP, *yCD::UPRT*-UC, *yCD::UPRT*-AT, *yCD::UPRT*-Plac in the presence of 5-FC exhibited statistically significantly lower viability compared to samples without 5-FC. The effect was dose-dependent and CM-type-dependent. The most pronounced cytotoxic effect was observed with CM from *yCD::UPRT*-AT (highlighted). The highest cell viability was observed in samples treated with CM from *yCD::UPRT*-BM (Fig. 2).

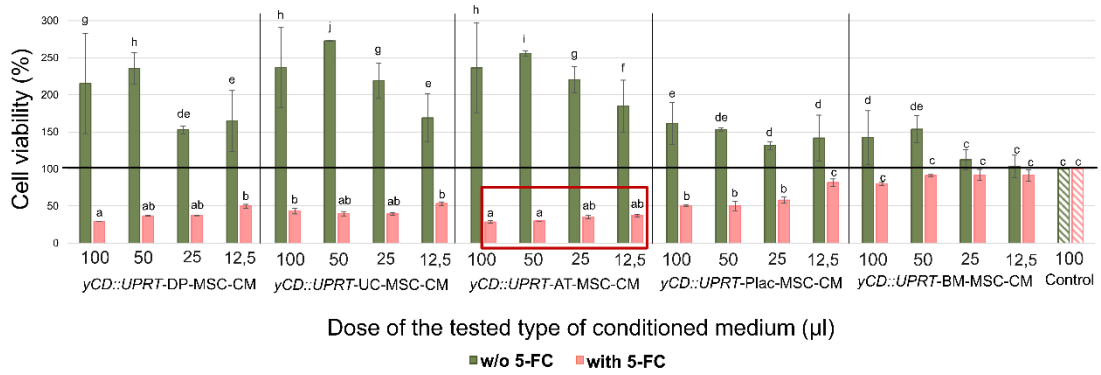

Figure 2. Types of *yCD:UPRT* conditioned medium tested on cell line derived from gastric adenocarcinoma. Cell viability was determined using the MTT test after exposure for 4 days. *yCD::UPRT*-DP-MSC-CM, *yCD::UPRT*-UC-MSC-CM, *yCD::UPRT*-Plac-MSC-CM, *yCD::UPRT*-BM-MSC-CM. Controls – tested cancer cells grown in the DMEM culture medium. The statistical significance was determined using the LSD ANOVA statistical test ($P < 0.05$). Columns marked with different letters indicate statistically significant differences, while columns sharing the same letter are not significantly different.

A decrease in cell viability was also confirmed in the Caco-2 cell line following the application of CM in combination with 5-FC, compared to samples in the absence of 5-FC. All tested CMs exhibited an inhibitory effect on the cells, with the most pronounced cytotoxic effect observed from *yCD::UPRT*-DP-MSC-CM, *yCD::UPRT*-UC-MSC-CM, and *yCD::UPRT*-AT-MSC-CM (highlighted). The observed trend was consistent with the results obtained in the MIA PaCa-2 and AGS cell lines (Fig. 3).

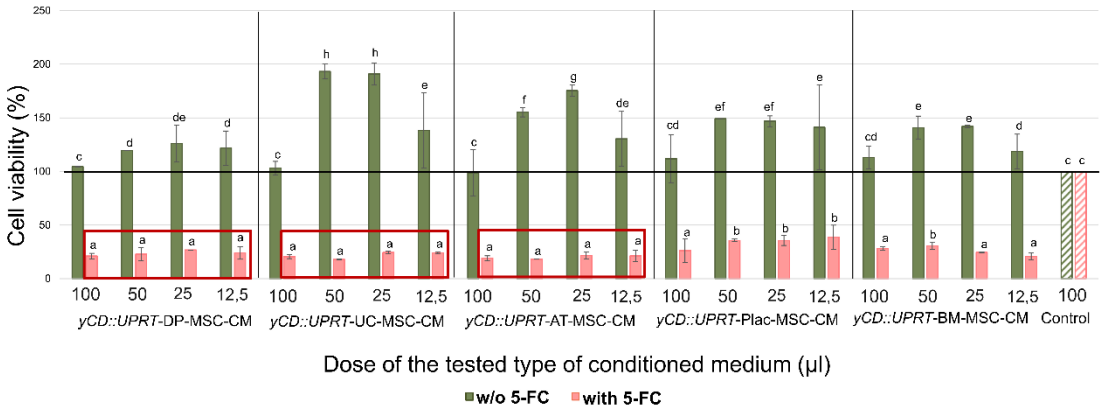

Figure 3. Types of *yCD:UPRT* conditioned medium tested on cell line derived from colorectal adenocarcinoma. Cell viability was determined using the MTT test after exposure for 4 days. *yCD::UPRT*-DP-MSC-CM, *yCD::UPRT*-UC-MSC-CM, *yCD::UPRT*-Plac-MSC-CM, *yCD::UPRT*-BM-MSC-CM. Controls – tested cancer cells grown in the DMEM culture medium. The statistical significance was determined using the LSD ANOVA statistical test ($P < 0.05$). Columns marked with different letters indicate statistically significant differences, while columns sharing the same letter are not significantly different.

Discussion

Gastrointestinal cancers remain among the most prevalent malignancies worldwide and are frequently diagnosed at advanced stages, when metastatic spread is already present, and therapeutic options become limited. In such cases, conventional treatment strategies often reach their limits, particularly due to tumor resistance to standard chemotherapy. These challenges highlight the need for innovative therapeutic approaches that specifically target tumor cells and the tumor microenvironment while minimizing systemic toxicity.

In the present study, we focused on suicide gene therapy mediated by exosomes released from genetically modified MSCs expressing the *yCD::UPRT* fusion gene. These exosomes are capable of homing to tumor cells, entering the intracellular space, and, in the presence of the prodrug 5-fluorocytosine, converting it into the cytotoxic agent 5-fluorouracil. This intracellular conversion subsequently induces programmed tumor cell death. Such an approach represents a targeted therapeutic strategy with the potential to overcome limitations associated with systemic administration of chemotherapeutics.

Our results demonstrated a high efficacy of this suicide gene therapy approach in three gastrointestinal cancer cell lines: MIA PaCa-2, AGS, and Caco-2. In all tested cell lines, the addition of 5-FC in combination with CM derived from *yCD::UPRT*-MSCs resulted in a decrease in tumor cell viability. These findings indicate that this therapeutic strategy is effective across multiple types of gastrointestinal tumor cells. Interestingly, CM derived from *yCD::UPRT*-BM MSCs showed a dose-dependent trend in the MIA PaCa-2 cell line, where decreasing CM concentration was associated with increased tumor cell viability. However, this dose-response relationship was not observed in the Caco-2 cell line, suggesting that the efficacy of different CM preparations may vary depending on the specific tumor cell type. Among all tested samples, CM derived from *yCD::UPRT*-DP, *yCD::UPRT*-UC, and *yCD::UPRT*-AT MSCs exhibited the strongest cytotoxic effect, indicating that the tissue origin of MSCs may influence the therapeutic potency of their secreted exosomes.

Our findings are consistent with previous studies investigating the *CD::UPRT*/5-FC suicide gene system. For example, Richard with coworkers demonstrated that adenoviral vectors carrying the *CD::UPRT* gene induced strong cytotoxicity in tumor cells derived from ascites and pleural effusions of patients with metastatic cancer, including cells resistant to 5-FU [8]. Similarly, it was reported that the *CD::UPRT*/5-FC system effectively induced apoptosis in eight metastatic human melanoma cell lines in a dose-dependent manner and was capable of eliminating long-term surviving tumor cells, highlighting the potency of this suicide gene strategy against aggressive cancers [9].

Despite these promising results, our study has several limitations. The experiments were performed on a limited number of 2D cell culture models, which do not fully replicate the complexity of the tumor microenvironment. Future studies should therefore include more advanced models such as spheroids, organoids, and *in vivo* animal models to better evaluate the therapeutic potential of *yCD::UPRT*-MSC-derived exosomes. Additionally, expanding the range of tested conditioned media from different MSC

sources could provide further insight into how MSC origin influences therapeutic efficacy.

Conclusion

Conditioned media from *yCD::UPRT*-transduced MSCs significantly reduced viability across all tested gastrointestinal cancer cell lines in the presence of 5-fluorocytosine. These findings support MSC-derived exosome–mediated suicide gene therapy as a promising targeted strategy for difficult-to-treat and metastatic cancers.

Acknowledgements

I would like to express my sincere gratitude to my PhD. thesis supervisor RNDr. Miroslava Matúšková, PhD and to all my colleagues especially doc. Ing. Čestmír Altaner, DrSc from the Stem Cell Preparation Department at the St. Elizabeth Cancer Institute in Bratislava. This project was supported by the APVV-20-0143 grant, the VEGA grant 1/0483/23 and 1/0489/20 from the Grant Agency of the Ministry of Education, Science, Research and Sport of the Slovak Republic.

References

[1] Naji A, Eitoku M, Favier B, Deschaseaux F, Rouas-Freiss N, et al. Biological functions of mesenchymal stem cells and clinical implications. Cell Mol Life Sci 2019; 76(17):3323–48. doi:10.1007/s00018-019-03125-1

[2] Altanerova U, Jakubechova J, Benejova K, Priscakova P, Pesta M, et al. Prodrug suicide gene therapy for cancer targeted intracellular by mesenchymal stem cell exosomes. Int J Cancer 2019; 144(4):897-908. doi: 10.1002/ijc.31792

[3] Wang Y, Wang H, Tan J, Cao Z, Wang Q, et al. Therapeutic effect of mesenchymal stem cells and their derived exosomes in diseases. Mol Biomed. 2025; 6(1):34. doi:10.1186/s43556-025-00277-4

[4] Zhong D, Wang Z, Ye Z, Wang Y, Cai X. Cancer-derived exosomes as novel biomarkers in metastatic gastrointestinal cancer. Mol Cancer 2024; 23(1):67. doi: 10.1186/s12943-024-01948-6

[5] Kucerova L, Altanerova V, Matuskova M, Tyciakova S, Altaner C. Adipose tissue-derived human mesenchymal stem cells mediated prodrug cancer gene therapy. Cancer Res 2007; 67(13):6304-13

[6] Vanova D, Andrezal M, Altanerova U, Matuskova M, Altaner C. Stem cells-derived suicide gene exosomes: a promising platform for innovative cancer therapy. Neoplasma 2026; 73(1):1-9. doi: 10.4149/neo_2025_251119N487

[7] Altaner C, Altanerova U. Mesenchymal Stem Cell Exosome-Mediated Prodrug Gene Therapy for Cancer. Methods Mol Biol 2019;1895:75-85. doi: 10.1007/978-1-4939-8922-5_6

[8] Richard C, Duivenvoorden W, Bourbeau D, Massie B, Roa W, et al. Sensitivity of 5-fluorouracil-resistant cancer cells to adenovirus suicide gene therapy. Cancer Gene Ther 2007;14(1):57-65. doi: 10.1038/sj.cgt.7700980

[9] Bernabei-Cornejo SG, Glikin GC, Finocchiaro LME. The Suicide Gene System Cytosine Deaminase::Uracylphosphoribosyltransferase/5-fluorocytosine Displays a Strong Cytotoxic Effect on Human Melanoma Cells. Curr Pharm Biotechnol 2026;27(2):212-227. doi: 10.2174/0113892010319891241121115002

ELECTROCHEMICAL DETECTION OF *BRAF* V600E MUTATION IN A LIQUID BIOPSY FORMAT

Ludmila Moranova[1], Johana Strmiskova[1,2], Katerina Ondraskova[1], Miroslav Bardelcik[1], Matous Cwik[3], Igor Kiss[3], Roman Hrstka[1], Martin Bartosik[1]

[1]Research Centre for Applied Molecular Oncology, Masaryk Memorial Cancer Institute, Brno, Czech Republic
[2] National Centre for Biomolecular Research, Faculty of Science, Masaryk University, Brno, Czech Republic
[3]Department of Comprehensive Cancer Care and Faculty of Medicine, Masaryk Memorial Cancer Institute and Masaryk University, Brno, Czech Republic

Introduction

The *BRAF* proto-oncogene encodes a serine/threonine protein kinase, and its mutations lead to ligand-independent activation of the MAPK pathway via phosphorylation of downstream MEK and ERK, ultimately promoting cancer development and progression. The most common alteration in the *BRAF* gene, accounting for approximately 90 % of cases, is the *BRAF* V600E mutation, resulting from a single nucleotide polymorphism (SNP) at codon 600 (replacement of valine with glutamic acid). The *BRAF* V600E substitution, predominantly found in melanoma and metastatic colorectal cancer (mCRC), is associated with aggressive traits and poor prognosis. Molecular testing of *BRAF* mutational status is crucial for guiding therapeutic decisions, driving the need for rapid diagnostic technologies [1,2]

Materials and methods

In this study, a new methodology was developed by combining SNP-specific primers for loop-mediated isothermal amplification (LAMP) with sensitive electrochemical (EC) detection.
The isolated DNA was introduced into the LAMP mixture containing six specific primers targeting V600E mutation, LAMP mastermix (Saphir Bst Turbo GreenMaster), and biotin-dUTP. Amplified products are generated only in a presence of the mutation. This assay enriches mutated DNA in an excess of unmutated (wild-type) DNA, making it highly suitable for mutation detection from liquid biopsy, where natural DNA yields are very low. The LAMP reaction was performed for 30 min at 62 °C.
Amplicons containing biotin labels were briefly denatured (95 °C, 10 min) and hybridized (Figure 1) on specific capture probes immobilized on the surface of magnetic

beads (MBs) (15 min, 40 °C). The final labeling step consisted of incubating the MBs with streptavidin-peroxidase polymer (15 min, RT).
In the last step, MBs were transferred onto the surface of an 8-electrode chip made of screen-printed carbon electrodes, and the peroxidase reaction was measured in the presence of hydroquinone/hydrogen peroxide substrate (amperometry, −0.3V, 60 s).

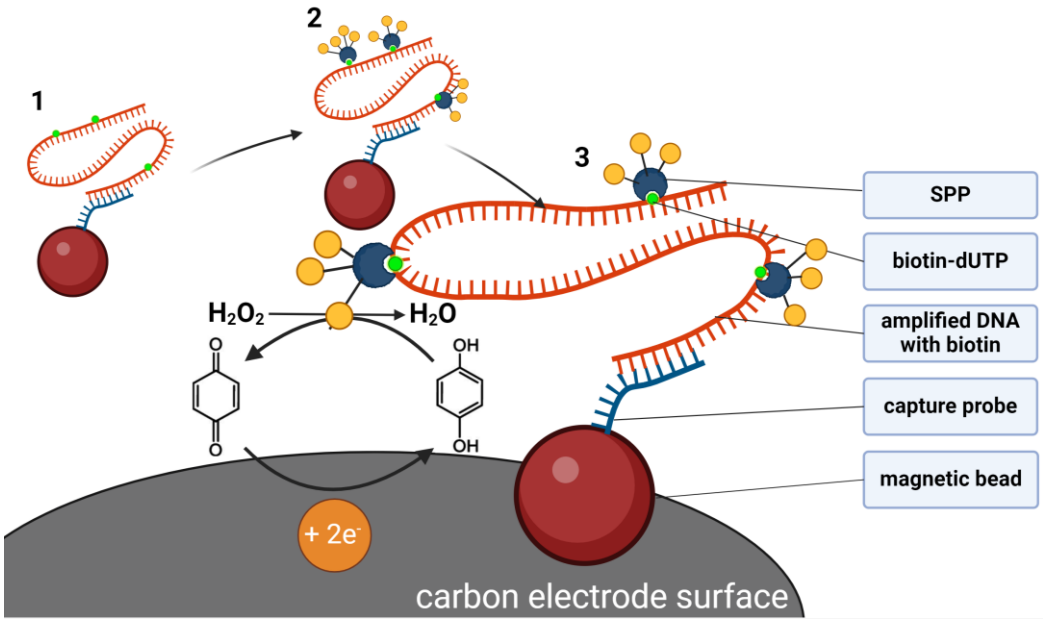

Figure 1: Scheme of the bioassay. 1) Amplified LAMP products with incorporated biotin-dUTP hybridize with capture probes on magnetic beads, 2) followed by SPP labeling, which binds to biotin moieties within the LAMP product, and 3) amperometric measurement of the SPP-catalyzed reaction involving the hydroquinone and hydrogen peroxide couple and a carbon electrode chip consisting of 8 working electrodes. Adapted from Ref [3] under a Creative Commons Attribution license CC BY 4.0.

The method was developed using cell lines, specifically A375 (V600E/V600E homozygous), HT 29 (V600E/wt heterozygous), Caco2 (wt/wt), SW620 (wt/wt), LAPC4 (wt/wt), and PANC1 (wt/wt) cells.
The final measurements were performed on 31 tissue samples and 27 serum samples from patients with colorectal cancer or melanoma. Samples were collected prior to surgery, all patients signed informed consent, and the study was approved by the Ethical Committee of Masaryk Memorial Cancer Institute (2020/1496/MOU).

Results

The SNP-LAMP assay was developed on cancer cell lines with high specificity (Figure 2). To avoid false-negative results, we included the detection of the ACTB gene. Negative results for ACTB show insufficient DNA input or poor quality of DNA after isolation.

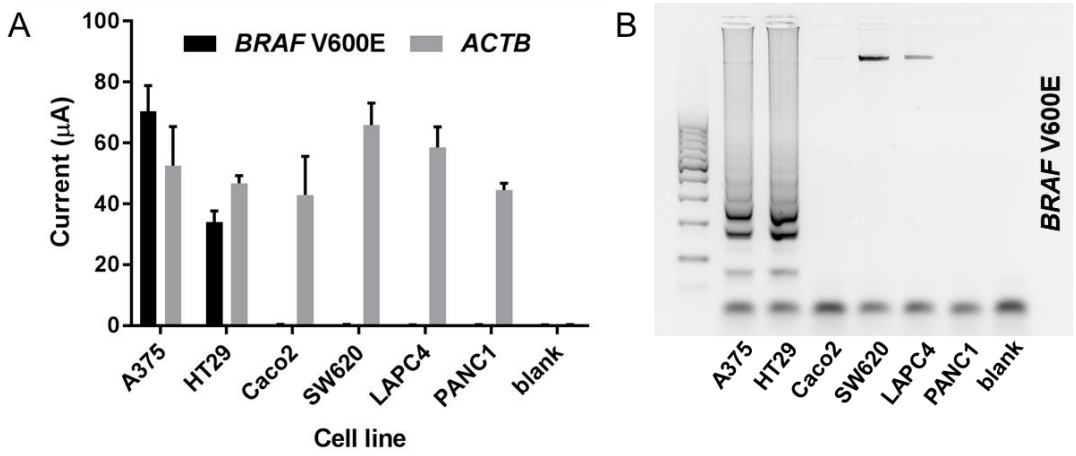

Figure 2: Selectivity assay. A: Electrochemical analysis of DNA from cancer cell lines using BRAF V600E and ACTB primers for the LAMP reaction. B: Visualization of LAMP products on agarose gel using the BRAF V600E primer set. Adapted from Ref [3] under a Creative Commons Attribution license CC BY 4.0.

After the sensitivity assay was performed (not shown), clinical sample analysis was performed. A total of 31 samples of DNA isolated from FFPE tissue (Figure 3A) and 27 samples of DNA isolated from serum (Figure 3C) were analyzed for the presence of BRAF V600E and ACTB. Based on ACTB levels under the cut-off value, 4 tissue and 1 serum samples were excluded from the data presented in Figure 3. Based on our experience, we recommend repeating measurements with ACTB signals under 10 μA and, if possible, increasing the DNA input into the reaction (for both biomarkers) to ensure the validity of the results. The results of the tissue samples were compared with those of the NGS analysis performed in the clinical laboratory (Figure 3B). Serum sample results were compared with ddPCR analysis (Figure 3D).

To mitigate potential discrepancies arising from differences between tissue and serum as sample sources, we compared our EC data from tissue samples with the NGS methodology (performed with the same tissue samples), and EC data from serum samples were compared with ddPCR (performed with the same serum samples). With this approach, a perfect accuracy of our test was obtained, reaching 100% sensitivity, specificity, and predictive values when compared with standard techniques.

Conclusion

Our results indicate that this simple and rapid EC-bioassay can detect the BRAF V600E mutation with high selectivity and sensitivity. To our knowledge, we report here for the first time a LAMP-based strategy for ctDNA analysis in the blood serum of cancer patients without any spiking, along with a positive ACTB control to check sample quality. Moreover, our LAMP primers are extremely selective and amplify only the V600E sequence, not the wild-type. Hence, there was no need to use any blocker or

clamping probe to suppress wt amplification or any detection probe in subsequent steps. Our data also emphasize the importance of internal quality control provided by measuring ACTB presence. Although routinely used in standard techniques such as real-time PCR, it is not often exploited in biosensor studies. Indeed, three of our tissue samples and one serum sample yielded low ACTB signals, reflecting their low quality (confirmed by ddPCR). Without this quality control, the samples were evaluated as having wild-type DNA.

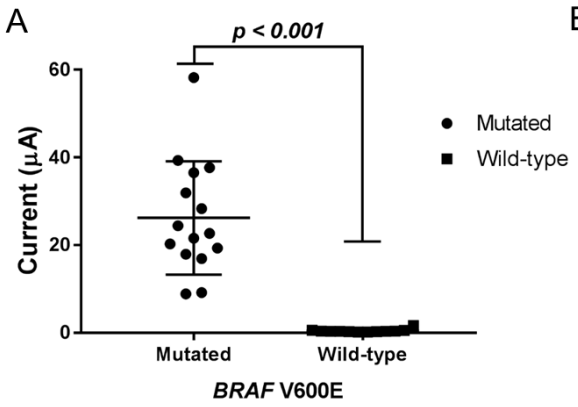

B

	Min	Max	Mean	SD	SEM
Mutated, N=15, µA	8.864	58.2	26.21	12.92	3.336
Wild-type, N=12, µA	0.159	1.611	0.439	0.387	0.112
Mutated *BRAF/ACTB*	0.135	2.126	0.789	0.473	0.122
Wild-type *BRAF/ACTB*	0.005	0.067	0.025	0.022	0.006

Comparison to NGS

BRAF V600E	%	95% Confidence interval
Sensitivity	100	0.7961 – 1
Specificity	100	0.7575 – 1
Positive predictive value	100	0.7961 – 1
Negative predictive value	100	0.7575 – 1

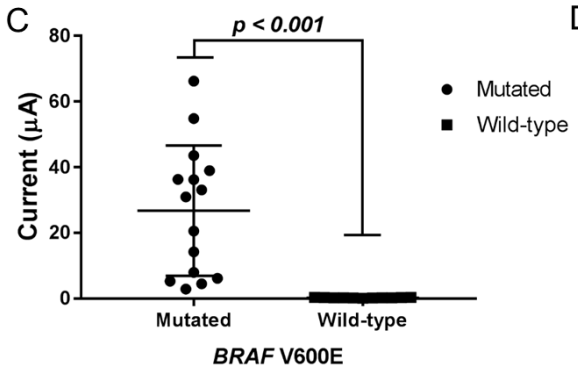

D

	Min	Max	Mean	SD	SEM
Mutated, N=15, µA	2.908	66.25	26.78	19.85	5.125
Wild-type, N=11, µA	0.118	3.355	0.247	0.075	0.022
Mutated *BRAF/ACTB*	0.101	1.319	0.535	0.361	0.093
Wild-type *BRAF/ACTB*	0.003	0.027	0.013	0.007	0.002

Comparison to ddPCR

BRAF V600E	%	95% Confidence interval
Sensitivity	100	0.7961 – 1
Specificity	100	0.7412 – 1
Positive predictive value	100	0.7961 – 1
Negative predictive value	100	0.7412 – 1

Figure 3: EC data from patient samples. A: Dot plot of tissue samples amplified using BRAF V600E primers. The samples were divided into two groups (mutated, wild-type) based on NGS data. Each dot represents the mean value of duplicate measurements. The difference between the two groups was highly significant ($p < 0.001$). B: Statistical data from EC measurements. Sensitivity and specificity were calculated using the chi-squared test and compared with NGS. C: Dot plot of serum samples amplified using BRAF V600E primers. The samples were divided into two groups (mutated, wild-type) based on ddPCR data. Each dot represents the mean value of duplicate measurements. The difference between these two groups was highly significant ($p < 0.001$). D: Statistical data from EC measurements. Sensitivity and specificity were calculated using the chi-squared test and compared with ddPCR. Adapted from Ref [3] under a Creative Commons Attribution license CC BY 4.0.

This EC-based bioassay shows clear discrimination between the mutated and wild-type sequences, in perfect agreement with either NGS or ddPCR, reaching a sensitivity of 0.5 ng/µL. The bioassay offers a simple, rapid, and efficient alternative to traditional

PCR methods for point-of-care diagnostics, particularly in settings with limited equipment and resource availability.

Acknowledgement

This work was supported by MH CZ - DRO (MMCI, 00209805), GAČR (25-15990S), BBMRI.CZ (no. LM2023033) and SALVAGE (OP JAC; reg. no. CZ.02.01.01/00/22_008/0004644) co-funded by the European Union and by the State Budget of the Czech Republic.

References

[1] Ascierto PA, Kirkwood JM, Grob J-J, Simeone E, Grimaldi AM, Maio M, Palmieri G, Testori A, Marincola FM, Mozzillo N. The role of BRAF V600 mutation in melanoma. J Transl Med 2012; 10 (1): 85. doi: 10.1186/1479-5876-10-85.

[2] Braune J, Keller L, Schiller F, Graf E, Rafei-Shamsabadi D, Wehrle J, Follo M, Philipp U, Hussung S, Pfeifer D, Mix M, Duyster J, Fritsch R, Bubnoff Dv, Meiss F, Bubnoff Nv. Circulating Tumor DNA Allows Early Treatment Monitoring in BRAF- and NRAS-Mutant Malignant Melanoma. JCO Precis Oncol 2020; (4): 20-31. doi: 10.1200/po.19.00174.

[3] Moranova L, Strmiskova J, Ondraskova K, Bardelcik M, Cwik M, Kiss I, Hrstka R, Bartosik M. Electrochemical Detection of BRAF V600E Mutation in a Liquid Biopsy Format: LAMPing the Way to an Improved Diagnostics and Treatment. Adv Mat Technol 2025; 10 (7): 2401404. doi: 10.1002/admt.202401404.

AURORA KINASE A INHIBITION AS A SYNTHETIC LETHALITY STRATEGY IN *ARID1A*-MUTATED GASTROENTEROPANCREATIC NEUROENDOCRINE CARCINOMA

Maria Pacalajova[1], Fabrice Viol[2,3], Laura Ruiz-Cañas[4,5], Efthymios Koniaris[6], Rihards Saksis[7], Sandra Batres-Ramos[4,5], Julie Earl[4], Agapi Kataki[8], Verona Buocikova[1], Monika Burikova[1], Marina Cihova1, Lucia Rojikova[1], Peter Makovicky[1], Miroslava Matuskova[1], Yvonne Kohl[9], Andrea Riedmayer[9], Marianna Makova[10,11], Ladislav Baciak[10], Daniel Gogola[11], Olesja Rogoza[7], Vita Rovite[7], Bruno Sainz Jr.[4,5], Bozena Smolkova[1], Joerg Schrader[2]

[1]*Biomedical Research Center, Slovak Academy of Sciences, Slovakia*
[2]*Medical Department, University Medical Center Hamburg-Eppendorf, Germany*
[3]*Mildred Scheel Cancer Career Center HaTriCS4, University Medical Center Hamburg Eppendorf, Germany*
[4]*Ramón y Cajal Health Research Institute (IRYCIS), Ramón y Cajal University Hospital. Ctra. Colmenar Viejo, Spain*
[5]*Department of Cancer, Instituto de Investigaciones Biomedicas Sols-Morreale (IIBM), CSIC-UAM, Spain*
[6]*Department of Pathology, Hippokration General, Hospital of Athens, Greece*
[7]*Latvian Biomedical Research and Study Centre, Ratsupites Str 1-k1, Latvia*
[8]*First Department of Propaedeutic Surgery, Hippokration General Hospital of Athens, Greece*
[9]*Department Bioprocessing & Bioanalytics, Fraunhofer Institute for Biomedical Engineering IBMT, Germany*
[10]*Faculty of Chemical and Food Technology, Slovak University of Technology, Slovakia*
[11]*Institute of Measurement Science, Slovak Academy of Sciences, Slovakia*

Introduction

Gastroenteropancreatic neuroendocrine neoplasms (GEP-NENs) are a heterogeneous group of malignancies arising from neuroendocrine cells of the gastroenteropancreatic tract, with clinical behaviour ranging from low-grade to highly aggressive [1]. Among them, gastroenteropancreatic neuroendocrine carcinomas (GEP-NECs) represent a rare but particularly aggressive subgroup, characterised by high-grade pathology, high mitotic rate, extensive necrosis, rapid progression and poor prognosis [2]. Their aggressive phenotype is compounded by the limited efficacy of conventional therapies and a strong predisposition for early metastatic spread [3, 4]. The standard treatment of cisplatin (CIS) combined with etoposide (ETO) achieves high initial response rates but is limited by treatment-related toxicity and acquired resistance.

In our previous panel-sequencing study of GEP-NEN cell lines, we identified a loss-of-function mutation in *ARID1A*, together with alterations in other genes, in the GEP-NEC-derived NT-38 cell line [5]. *ARID1A* mutations have been reported in

approximately 10–35 % of GEP-NENs, with frequencies influenced by tumour site, grade and molecular subtype [6–8]. ARID1A is a key subunit of the SWI/SNF chromatin-remodelling complex, regulating DNA accessibility and contributing to the DNA damage response and replication fidelity. Its loss causes genomic instability and renders cells dependent on compensatory pathways such as the Aurora kinase A (AURKA)-mediated spindle checkpoint [9]. AURKA inhibition therefore, exhibits a synthetic lethal interaction with *ARID1A* loss [10]. Alisertib (ALI) is the most clinically advanced AURKA inhibitor [11, 12], which binds the ATP-binding site of AURKA, and triggers G2/M arrest, mitotic slippage and apoptosis [13]. Exploiting synthetic lethality can selectively eliminate *ARID1A*-mutated cells while sparing normal tissues [14–16].

Materials and methods

Cell line

The patient-derived neuroendocrine cell line NT-38 was derived from a duodenal small-cell NEC of a 78-year-old female patient and was confirmed *ARID1A*-deficient. The cell line was synaptophysin (SYP)-positive, chromogranin A (CgA)-negative, with Ki-67 of 70 %. Cells were cultured on Collagen IV-coated dishes in RPMI media with 10 % FBS, penicillin-streptomycin, L-glutamine, 20 ng/ml EGF and 10 ng/ml FGF2, at 37 °C and 5 % CO2.

The orthotopic xenograft study

The *in vivo* study was performed under ethical approvals Ro-290-3/2020-220 and Ro-3508/2023-220 in an authorised facility (licence SK UCH 02022). For the orthotopic xenograft study, the NT-38 cells (8×10^5 in 50 µl of high-glucose DMEM/extracellular matrix, 1:1) were injected into the pancreas of NSG mice (10–12 weeks, both sexes). Mice were randomised into four groups: six per vehicle group and eight per treatment group. Based on a pilot testing, dose of 30 mg/kg ALI was selected for the main experiment.

Treatment

Treatment started 14 days after injection of cells, when tumours reached ~30 mm³ on magnetic resonance imaging (MRI). ALI was delivered by daily oral gavage for 21 days, and the ALI-vehicle group received equal volumes of saline-based vehicle. The standard-of-care control goup received intraperitoneal CIS (4 mg/kg) plus three consecutive daily intraperitoneal doses of ETO (8 mg/kg), repeated after two weeks. Mice were sacrificed one week after the last dose. Tumour growth was monitored weekly by MRI in a subset of four mice (Fig. 1).

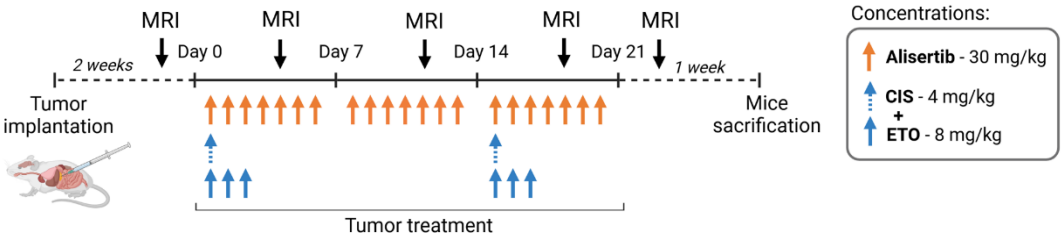

Figure 1. Therapeutic regimen of the orthotopic NT-38 xenograft model.

Flow cytometry

Flow cytometry was used to assess cell cycle distribution and apoptosis in NT-38 cells following ALI treatment. Apoptosis/necrosis was assessed with the Annexin V assay after 48-h treatment with 25 or 50 nM ALI, using PE-Annexin V and DAPI on a BD FACSCanto II. Cell-cycle distribution was analysed after 48-h ALI treatment (25 or 50 nM) by RNase A digestion and propidium iodide staining on a CytoFlex S.

Results

Both ALI and CIS + ETO significantly reduced tumour volume and final tumour weight compared to vehicle controls, with comparable efficacy between the two treatments (Fig. 2A-D). Mouse body weight change diverged significantly between groups, as CIS + ETO treatment resulted in significant post-treatment weight loss (Fig. 2E) accompanied by abdominal fluid accumulation in 4 of 8 animals (50 %), whereas the ALI group showed only a transient early dip that stabilised after day 10 and remained at baseline until the end of the experiment. This divergence suggests that, while both regimens achieved similar tumour control, ALI was substantially better tolerated systemically.

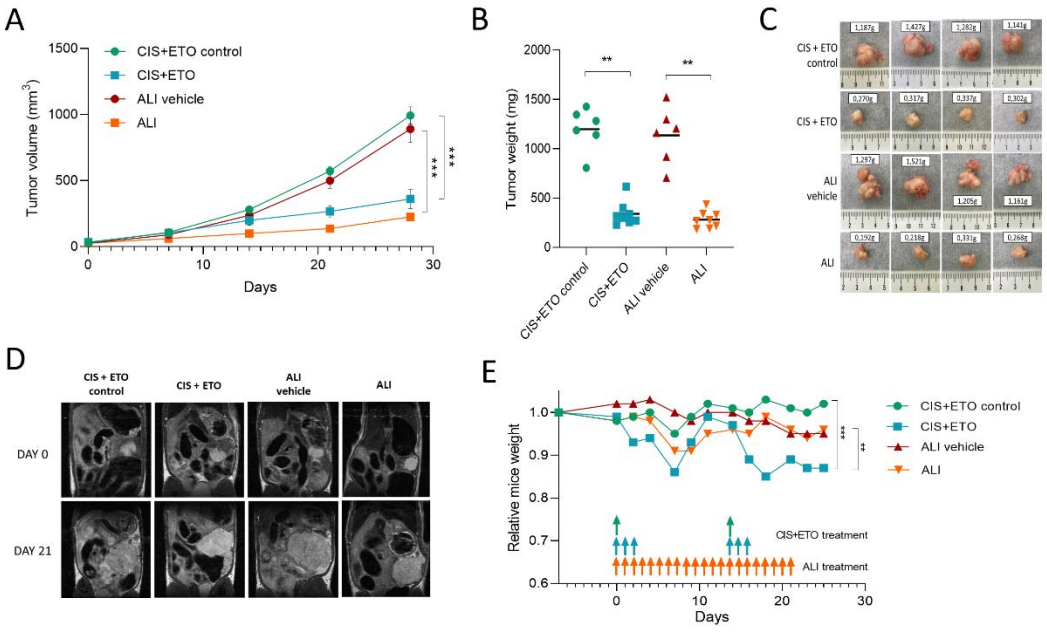

Figure 2. Therapeutic efficacy of alisertib (ALI) and standard-of-care cisplatin + etoposide (CIS + ETO) in the orthotopic NT-38 xenograft model. (A) Tumour volume over time (mean ± SEM). (B) Individual tumour weights at the therapeutic endpoint (mean ± SD). (C) Representative macroscopic images of excised tumours with individual weights indicated. (D) Representative MRI scans tracking tumour growth during treatment. (E) Relative mouse body weight over time, normalised to pre-treatment weight (day 0). ** $p<0.01$; *** $p<0.001$

To capture the acute cellular response to AURKA inhibition, flow cytometry was performed on NT-38 cells treated for 48 h with 25 or 50 nM ALI. Annexin V / DAPI staining revealed a dose-dependent, statistically significant increase in Annexin V-positive cells, consistent with early apoptosis induction (Fig. 3). In parallel, propidium iodide-based cell-cycle analysis showed a marked G2/M accumulation at both 25 and 50 nM ALI. These cytometric readouts captured effects that were no longer detectable at the *in vivo* endpoint, sampled one week after the last dose.

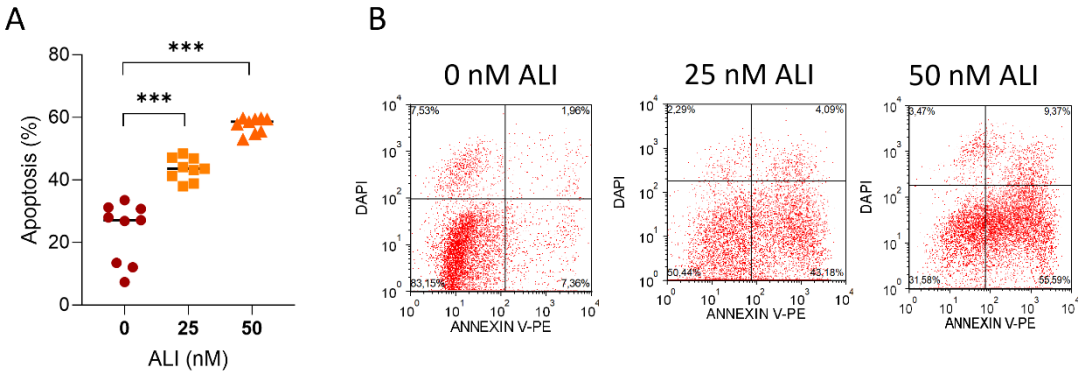

Figure 3. Alisertib (ALI)-induced apoptosis in NT-38 cells analysed by flow cytometry. (A) Proportion of apoptotic cells after treatment for 48 h with 0 nM, 25 nM or 100 nM ALI. (B) Representative Annexin V/DAPI flow cytometry plots of NT-38 cells showing a dose-dependent increase in Annexin V-positive apoptotic cells. *** $p<0.001$

Discussion

This study evaluated ALI as a synthetic lethality strategy in NT-38-derived orthotopic in vivo model. ALI achieved anti-tumor efficacy comparable to CIS + ETO chemotherapy but with a markedly better tolerability profile, as no significant weight loss, no abdominal fluid accumulation and no organ-level toxicity on histopathology was detected. Therefore, ALI represents a plausible alternative for *ARID1A*-mutant GEP-NEC patients who do not tolerate platinum-based regimens well [4]. Comparable efficacy combined with favourable tolerability has been reported in preclinical colorectal cancer xenograft models, where single-agent ALI produced sustained tumor growth inhibition without the weight loss observed with cytotoxic comparators [17].

The mechanistic picture is consistent with prior reports that ALI acts through mitotic disruption and cell-cycle modulation [18]. Acute flow-cytometry readouts at 48 h showed clear apoptosis induction and G2/M arrest in NT-38 cells, while *in vivo* endpoint tissue harvested one week after the last dose showed only modest apoptosis signals, with unchanged Ki-67. This is consistent with Neel et al., who observed early Ki-67 changes within hours but not at 28 days [19], and with Wang-Bishop et al., who documented Ki-67 decrease in gastrointestinal xenografts at day 7 [20], and with reports that combination therapies suppress Ki-67 more reliably than ALI monotherapy [21].

One limitation of this study is that duodenal NT-38 cells had to be implanted into the mouse pancreas for orthotopic modelling, as the establishment of true duodenopancreatic orthotopic models in mice remains technically challenging. Then,

use of a single patient-derived cell line cannot capture the full heterogeneity of GEP-NECs, and neuroendocrine tumour behaviour varies considerably across anatomical sites, therefore broader validation across NEN subtypes is needed.

Conclusion

In conclusion, AURKA inhibition with ALI is selectively effective against *ARID1A*-deficient GEP-NEC. Its anti-tumor efficacy was demonstrated in the orthotopic NT-38 xenograft, and flow cytometry identified apoptosis and G2/M arrest as the underlying acute mechanism. Integrating *ARID1A* mutation status into patient stratification could refine the use of AURKA inhibitors in this setting, and combination strategies targeting complementary vulnerabilities offer a clear path for further development.

Acknowledgement

The research was supported by the European Regional Development Fund (NExT-0711), COST action CA21116, funding from the Slovak Academy of Sciences (APVV-20-0143, APVV-21-0197), and the VISION project (H2020 – No. 857381).
The presented results were previously published as part of the study entitled "Aurora kinase A inhibition as a synthetic lethality strategy in ARID1A-mutated gastroenteropancreatic neuroendocrine carcinoma" [22].

References

[1] Cives M, Strosberg JR. Gastroenteropancreatic neuroendocrine tumors. CA Cancer J Clin 2018; 68: 471–487. doi: 10.3322/caac.21493.

[2] Sorbye H, Strosberg J, Baudin E, Klimstra DS, Yao JC. Gastroenteropancreatic high-grade neuroendocrine carcinoma. Cancer 2014; 120(18): 2814–2823. doi: 10.1002/cncr.28721.

[3] Sorbye H, Baudin E, Borbath I, Caplin M, Chen J, Cwikla JB, et al. Unmet needs in high-grade gastroenteropancreatic neuroendocrine neoplasms (WHO G3). Neuroendocrinology 2019; 108(1): 54–62. doi: 10.1159/000493318.

[4] Ooki A, Osumi H, Fukuda K, Yamaguchi K. Potent molecular-targeted therapies for gastro-entero-pancreatic neuroendocrine carcinoma. Cancer Metastasis Rev 2023; 42(4): 1021–1054. doi: 10.1007/s10555-023-10121-2.

[5] Viol F, Sipos B, Fahl M, Clauditz TS, Amin T, Kriegs M, et al. Novel preclinical gastroenteropancreatic neuroendocrine neoplasia models demonstrate the feasibility of mutation-based targeted therapy. Cell Oncol 2022; 45(6): 1401–1419. doi: 10.1007/s13402-022-00727-z.

[6] Wu H, Yu Z, Liu Y, Guo L, Teng L, Guo L, et al. Genomic characterization reveals distinct mutation landscapes and therapeutic implications in neuroendocrine carcinomas of the gastrointestinal tract. Cancer Commun 2022; 42(12): 1367–1386. doi: 10.1002/cac2.12378.

[7] Venizelos A, Elvebakken H, Perren A, Nikolaienko O, Deng W, Lothe IMB, et al. The molecular characteristics of high-grade gastroenteropancreatic neuroendocrine neoplasms. Endocr Relat Cancer 2021; 29(1): 1–14. doi: 10.1530/ERC-21-0152.

[8] Puccini A, Poorman K, Salem ME, Soldato D, Seeber A, Goldberg RM, et al. Comprehensive genomic profiling of gastroenteropancreatic neuroendocrine neoplasms

(GEP-NENs). Clin Cancer Res 2020; 26(22): 5943–5951. doi: 10.1158/1078-0432.CCR-20-1804.
[9] Mandal J, Mandal P, Wang TL, Shih IM. Treating ARID1A mutated cancers by harnessing synthetic lethality and DNA damage response. J Biomed Sci 2022; 29(1): 71. doi: 10.1186/s12929-022-00856-5.
[10] Du R, Huang C, Liu K, Li X, Dong Z. Targeting AURKA in cancer: molecular mechanisms and opportunities for cancer therapy. Mol Cancer 2021; 20(1): 15. doi: 10.1186/s12943-020-01305-3.
[11] Durlacher CT, Li ZL, Chen XW, He ZX, Zhou SF. An update on the pharmacokinetics and pharmacodynamics of alisertib, a selective Aurora kinase A inhibitor. Clin Exp Pharmacol Physiol 2016; 43(6): 585–601. doi: 10.1111/1440-1681.12571.
[12] Qin RS, Li CT, Chen F, Luo S, Wang C, Li J, et al. AURKA inhibition shows promise as a therapeutic strategy for ARID1A-mutant colorectal cancer. Discov Oncol 2024; 15(1): 556. doi: 10.1007/s12672-024-01433-y.
[13] Hein KZ, Stephen B, Fu S. Therapeutic role of synthetic lethality in ARID1A-deficient malignancies. J Immunother Precis Oncol 2024; 7(1): 41–52. doi: 10.36401/JIPO-23-10.
[14] Mullen J, Kato S, Sicklick JK, Kurzrock R. Targeting ARID1A mutations in cancer. Cancer Treat Rev 2021; 100: 102287. doi: 10.1016/j.ctrv.2021.102287.
[15] Wu C, Lyu J, Yang EJ, Liu Y, Zhang B, Shim JS. Targeting AURKA-CDC25C axis to induce synthetic lethality in ARID1A-deficient colorectal cancer cells. Nat Commun 2018; 9(1): 3212. doi: 10.1038/s41467-018-05694-4.
[16] Pitts TM, Bradshaw-Pierce EL, Bagby SM, Hyatt SL, Selby HM, Spreafico A, et al. Antitumor activity of the aurora a selective kinase inhibitor, alisertib, against preclinical models of colorectal cancer. Oncotarget 2016; 7(32): 50290–50301. doi: 10.18632/oncotarget.10366.
[17] Sehdev V, Katsha A, Ecsedy J, Zaika A, Belkhiri A, El-Rifai W. The combination of alisertib, an investigational Aurora kinase A inhibitor, and docetaxel promotes cell death and reduces tumor growth in preclinical cell models of upper gastrointestinal adenocarcinomas. Cancer 2013; 119(4): 904–914. doi: 10.1002/cncr.27801.
[18] Tan J, Xu W, Lei L, Liu H, Wang H, Cao X, et al. Inhibition of Aurora kinase A by alisertib reduces cell proliferation and induces apoptosis and autophagy in HuH-6 human hepatoblastoma cells. Onco Targets Ther 2020; 13: 3953–3963. doi: 10.2147/OTT.S246346.
[19] Neel NF, Stratford JK, Shinde V, Ecsedy JA, Martin TD, Der CJ, et al. Response to MLN8237 in pancreatic cancer is not dependent on RalA phosphorylation. Mol Cancer Ther 2014; 13(1): 122–133. doi: 10.1158/1535-7163.MCT-12-1232.
[20] Wang-Bishop L, Chen Z, Gomaa A, Lockhart AC, Salaria S, Wang J, et al. Inhibition of AURKA reduces proliferation and survival of gastrointestinal cancer cells with activated KRAS by preventing activation of RPS6KB1. Gastroenterology 2019; 156(3): 662–675.e7. doi: 10.1053/j.gastro.2018.10.030.
[21] Davis SL, Ionkina AA, Bagby SM, Orth JD, Gittleman B, Marcus JM, et al. Preclinical and dose-finding phase I trial results of combined treatment with a TORC1/2 inhibitor (TAK-

228) and Aurora A kinase inhibitor (alisertib) in solid tumors. Clin Cancer Res 2020; 26(17): 4633–4642. doi: 10.1158/1078-0432.CCR-19-3498.

[22] Urbanova M, Viol F, Ruiz-Cañas L, Koniaris E, Saksis R, Batres-Ramos S, et al. Aurora kinase A inhibition as a synthetic lethality strategy in ARID1A-mutated gastroenteropancreatic neuroendocrine carcinoma. Cancer Letters 2025; 634: 218033. doi: 10.1016/j.canlet.2025.218033.

ANALYSIS OF THE RELATIVE EXPRESSION OF *SIRT1* AND *SIRT7* IN PATIENTS WITH BREAST CANCER

Daniela Szaboova[1,2], Zdenka Hertelyova[2], Zuzana Gulasova[2], Jozef Radonak[3], Roman Benacka[1]

[1]*Department of Pathological Physiology, Pavol Jozef Šafárik University in Košice*
[2]*Center of Clinical and Preclinical Research MEDIPARK, Pavol Jozef Šafárik University in Košice*
[3] *1st Department of Surgery, Pavol Jozef Šafárik University in Košice*

Introduction

Breast cancer is a phenotypically and genotypically heterogeneous malignant disease arising from the neoplastic transformation of epithelial cells of the ducts or lobules. Breast cancer is currently the most commonly diagnosed cancer in women, as well as being the leading cause of cancer-related death [1]. Sirtuins (SIRTs – silent information regulators) represent a family of nicotinamide adenine dinucleotide (NAD+)-dependent histone deacetylases classified as class III. SIRT1 plays an important role in cell proliferation, cell cycle, apoptosis, energy metabolism and DNA repair. It is responsible for chromatin remodeling beneficial for tumor progression [2]. In the context of carcinogenesis and apoptosis regulation, the most important non-histone targets of SIRT 1 include p53, Ku70, E2F1, and FOXO3a [3]. SIRT7 interacts with RNA polymerase I, thereby positively regulating the transcription of rRNA genes and ribosome formation. Complete absence of SIRT7 leads to the arrest of cell proliferation and the induction of apoptosis [4]. Currently, several studies report conflicting results on the gene expression of SIRT1 and SIRT7 in breast cancer [5]. and thus the function of these genes in carcinogenesis is still not yet completely clear.

Materials and methods

Blood collection

Peripheral blood was collected from 63 female patients with non-metastatic ER+PR+HER2- tumors and 33 healthy female blood donors after an overnight fast at the 1st Department of Surgery at the Faculty of Medicine of Pavol Jozef Šafárik University in Košice as part of the ongoing project VEGA No. 1/0622/20 - Study of the molecular and metabolomic profile of breast cancer (principal investigator Prof. MUDr.

Jozef Radoňak, CSc., MPH). Exclusion criteria were previous oncological disease or oncological treatment.

RNA isolation and RT-qPCR analysis

The NucleoSpin RNA blood kit (Macherey-Nagel) was used to isolate RNA from whole blood. The final volume of RNA obtained from blood was 35 µl. The isolated total RNA was used to determine the concentration. The Qubit RNA BR Assay kit (Invitrogen) was used to determine the concentration of isolated RNA from individual samples. The concentrations themselves were measured on a Qubit 3 Fluorometer (Invitrogen), with the concentration value given in ng/µl with an optimal purity of 1.8–2.0 for RNA. Aliquots of RNA with a given concentration and adequate purity were used in the real-time PCR reaction.

Primers were designed for the purpose of analyzing the transcriptional activity of mRNA expression of *SIRT1*, *SIRT7,* and *GAPDH* (reference gene) genes, as well as for determining the number of copies of these genes. The design of primers was based on a specific chromosomal localization - for mRNA after splicing and for DNA sequences of the relevant genes. The specificity and suitability of the primers were confirmed by reverse transcription Transcriptor First Strand cDNA Synthesis Kit (Roche, Dubai, UAE). The analysis of the relative gene expressions of the *SIRT1*, *SIRT7*, and *GAPDH* (reference gene) was performed in a LightCycler® 480 Instrument II thermocycler (Roche, Dubai, UAE) using LightCycler® EvoScript RNA SYBR® Green I Master.

Analysis of isolated mRNA samples from the whole blood of patients and controls was performed in triplicates. Results were expressed as relative change in gene expression compared to the healthy control group, and the Livak $2^{-\Delta\Delta CT}$ method was used to calculate the relative expression change [21]. Values were normalized to the expression of a reference gene *GAPDH*. Data are expressed as log2(fold-change) and in the form of a mean ± standard deviation.

Statistical analysis

Due to the non-normal distribution of the data (Shapiro-Wilk test, $p<0,001$), the Mann-Whitney U test was used for the group comparison analysis (patients vs controls). For the individual analysis of the relative expression change in each patient, one-sample t-test was used to compare the average relative change in gene expression of each sample against the reference value of 0. Statistical processing of data obtained by the molecular method RT-qPCR was per-formed in the GraphPad Prism version 8 program (GraphPad Software by Dotmatics, La Jolla, California, USA). Values with * $p< 0.05$; ** $p< 0.01$; *** $p< 0.001$ were considered sta-tistically significant.

Results

RT-qPCR analysis and subsequent statistical evaluation of the *SIRT1* gene expression comparison between breast cancer patients and healthy controls revealed a statistically significant downregulation of the *SIRT1* gene in whole peripheral blood of breast cancer patients ($p<0.001$) (Figure 1A). Individual analysis using a One-sample t-test showed that 62% of patients had a statistically significant downregulation of *SIRT1* compared to the reference level of the control group (log2 FC = 0). The ability of relative *SIRT1* expression to discriminate between the patient group and healthy controls was

assessed using ROC analysis. The resulting area under the curve (AUC) reached a value of 0.715 (95% CI: 0.615–0.815; $p < 0.001$), indicating a moderate diagnostic potential of this parameter as a potential biomarker. Based on our results, we determined a relative expression of -0.12 (log2 FC) as the optimal cut-off for discrimination between patients and controls based on the Youden index (Figure 1B). At this value, the test achieved a sensitivity of 65.1% and a specificity of 66.7%.

Analysis by RT-qPCR and subsequent statistical evaluation of the comparison of *SIRT7* gene expression in the group of patients with breast cancer and healthy controls did not show any statistically significant difference ($p = 0.1102$) (Figure 1C). The relative expression of *SIRT7* did not show significant differences between the group of patients and healthy controls. While for *SIRT1* we observed a uniform downward trend in most subjects, individual analysis using a One-sample t-test for *SIRT7* revealed significant inter-individual variability without a clear predominance of downregulation or upregulation, which correlates with the non-significant result of the group and ROC analysis. Unlike *SIRT1*, ROC analysis for the *SIRT7* gene did not show diagnostic significance (AUC = 0.600; 95% CI: 0.476 – 0.724; $p = 0.11$) (Figure 1D).

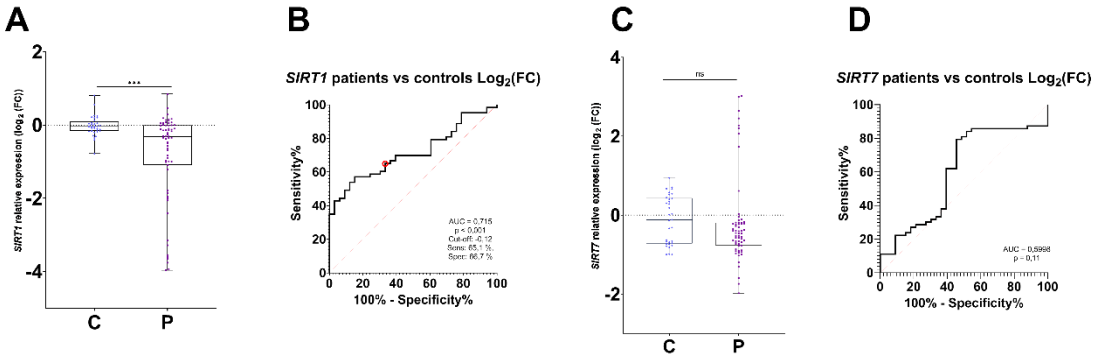

Figure 1 Analysis of relative SIRT1 gene expression in breast cancer patients. A) Comparison of relative SIRT1 mRNA levels (log2 FC) in whole peripheral blood of healthy controls (C; n = 33) and patients (P; n = 63). Horizontal lines in the box plot represent the median and interquartile range; individual points represent individual subjects. Statistical significance was assessed by the Mann-Whitney test (***$p<0.001$). B) ROC curve evaluating the diagnostic accuracy of relative SIRT1 expression in discriminating between patients and controls. The area under the curve (AUC) reached 0.715 ($p<0.001$). The red circle indicates the optimal cut-off point (-0.12) determined using the Youden index, at which the test achieved a sensitivity of 65.1% and a specificity of 66.7%. C) Comparison of relative SIRT7 mRNA levels (log2 FC) in whole peripheral blood in a healthy control group (C; n = 33) and a patient group (P; n = 63). The horizontal lines in the box plot represent the median and interquartile range. The statistical comparison did not show a significant difference between the studied groups (ns=not significant, p=0.11; Mann-Whitney test). D) ROC curve for relative SIRT7 expression. The area under the curve (AUC=0.5998; p=0.11) con-firms that this parameter does not have sufficient diagnostic power to distinguish diseased subjects from healthy controls in this patient cohort.

Discussion

We analyzed the relative expression of *SIRT1* and *SIRT7* genes in peripheral blood of breast cancer patients and healthy controls using RT-qPCR. We found significant interindividual variability, likely related to disease heterogeneity, with *SIRT1*

expression significantly downregulated in patients and showing moderate diagnostic value. *SIRT1* is involved in DNA repair and regulation of key cellular processes (e.g., via p53, FOXO, NF-κB), thereby influencing apoptosis, metabolism, and the cell cycle [6]. *SIRT7* regulates rRNA transcription, genome stability, and cell proliferation, but its role in tumor progression is ambiguous and context-dependent [7]. In contrast to studies focused mainly on tumor tissue or serum, the aim of this work was to verify whether the differences in expression are also reflected in peripheral blood.

Available results point to an inconsistent role of both genes in carcinogenesis. *SIRT1* can act as both a tumor suppressor and an oncogene depending on the environment – its reduced expression is associated with tumor progression, while increased expression can promote aggressiveness and resistance to treatment [8]. A similar discrepancy has been observed for *SIRT7*, where it has been associated with both prognosis and metastasis [9]. PBMC analyses suggest stable expression of *SIRT1* and more variable expression of *SIRT7* without clear discriminatory ability between groups [10], which is also supported by our results – a decrease in both genes, statistically significant only for *SIRT1*, and high variability especially for *SIRT7*. Overall, peripheral blood expression of these genes appears to have limited diagnostic potential, with their biological role being context-dependent. The results also highlight the need for further analyses with emphasis on molecular tumor subtypes and clinical characteristics of patients.

Conclusion

In conclusion, our analysis demonstrates a significant differential expression of *SIRT1* and *SIRT7* in the peripheral blood of breast cancer patients. While *SIRT1* was downregulated and showed a fair diagnostic potential to distinguish patients from healthy controls, *SIRT7* exhibited high inter-individual variability and lacked statistical significance as a biomarker. Consequently, *SIRT1* mRNA levels could serve as a valuable component of a non-invasive multi-marker diagnostic panel, potentially improving the accuracy of screening for the disease.

Acknowledgement

This research was funded by MŠVVaŠ SR - VEGA n. 1/0607/25 (principal investigator: Prof. MUDr. Jozef Radoňak, CSc., MPH).

References

[1] Bray F, Laversanne M, Sung H, Ferlay J, Siegel RL, et al. Global Cancer Statistics 2022: GLOBOCAN Estimates of Incidence and Mortality Worldwide for 36 Cancers in 185 Countries. CA. Cancer J Clin 2024; 74: 229–263, doi:10.3322/caac.21834.

[2] Houtkooper RH, Pirinen E, Auwerx J. Sirtuins as Regulators of Metabolism and Health-span. Nat Rev Mol Cell Biol 2012; 13: 225–238, doi:10.1038/nrm3293.

[3] Wu QJ, Zhang TN, Chen HH, Yu XF, Lv JL, et al. The sirtuin family in health and disease. Signal Transduct Target Ther 2022; 7: 402. doi: 10.1038/s41392-022-01257-8.

[4] Tang M, Tang H, Tu B, Zhu WG. SIRT7: a sentinel of genome stability. Open Biol 2021; 11: 210047. doi: 10.1098/rsob.210047.

[5] Ashraf N, Zino S, Macintyre A, Kingsmore D, Payne AP, et al. Altered Sirtuin Expression Is Associated with Node-Positive Breast Cancer. Br J Cancer 2006; 95: 1056–1061, doi: 10.1038/sj.bjc.6603384.
[6] Ding J, Ye MT, Zhang, S. The Roles of Sirt1 in Breast and Gynecologic Malignancies. Biology (Basel) 2025, 14: 1510. doi: 10.3390/biology14111510.
[7] Huo Q, Chen S, Zhuang J, Quan C, Wang Y, et al. SIRT7 downregulation promotes breast cancer metastasis via LAP2α-induced chromosomal instability. Int J Biol Sci 2023; 19: 1528-1542. doi: 10.7150/ijbs.75340.
[8] Jin X, Wei Y, Xu F, Zhao M, Dai K, et al. SIRT1 Promotes Formation of Breast Cancer through Modulating Akt Activity. J Cancer 2018; 9: 2012–2023, doi:10.7150/jca.24275.
[9] Huo Q, Li Z, Cheng L, Yang F, Xie, N. SIRT7 Is a Prognostic Biomarker Associated With Immune Infiltration in Luminal Breast Cancer. Front Oncol 2020; 10: 621. doi: 10.3389/fonc.2020.00621.
[10] LaBreche HG, Nevins JR, Huang, E. Integrating factor analysis and a transgenic mouse model to reveal a peripheral blood predictor of breast tumors. BMC Med Genomics 2011; 4: 61, doi: 10.1186/1755-8794-4-61.

BREAKING THE DEFENSES: VITAMINS A & D LEVERAGE SPHINGOLIPID METABOLISM TO POTENTIATE CHEMOSENSITIVITY IN LEUKEMIA CELLS

Pavol Stefik[1], Denisa Nechajova[1], Kamila Durisova[1], Lucia Sofrankova[1], Jana Spaldova[1], Albert Breier[1,2], Boris Lakatos[1]

[1]*Institute of Biochemistry and Microbiology, Faculty of Chemical and Food Technology, Slovak University of Technology in Bratislava, Radlinského 9, 812 37 Bratislava, Slovakia*
[2]*Centre of Biosciences, Slovak Academy of Sciences, Dúbravská cesta 9, 840 05 Bratislava, Slovakia*

Introduction

Acute myeloid leukemia (AML) represents a complex and heterogeneous group of hematological malignancies characterized by the uncontrolled clonal proliferation of immature myeloid precursors, or blasts, in the bone marrow and peripheral blood. This accumulation leads to hematopoietic failure, causing severe clinical symptoms such as anemia, infections, and impaired coagulation [1]. Despite significant progress in induction chemotherapy, typically involving cytarabine and anthracyclines, the overall 5-year survival rate for AML patients remains approximately 30%, dropping drastically to only 10% for patients over the age of 60 [2]. A major obstacle to successful treatment is multi-drug resistance (MDR), often driven by the overexpression of ABC transporters like P-glycoprotein (ABCB1), which actively effluxes various chemotherapeutic agents from the cell [3].

In response to these challenges, differentiation therapy has emerged as a promising targeted strategy. Unlike traditional cytotoxic treatments, it aims to force leukemic blasts to bypass their maturation blockade and enter non-proliferative states, senescence, or apoptosis. While highly successful in acute promyelocytic leukemia (APL) using all-trans-retinoic acid (ATRA), its efficacy in other AML subtypes as a monotherapy remains limited [4]. Recent studies suggest that the effectiveness of differentiation inducers like ATRA and calcitriol (VD3) may extend beyond maturation, influencing the "sphingolipid rheostat" – the metabolic balance between pro-apoptotic ceramide and sphingosine and pro-survival ceramide-1-phosphate and sphingosine-1-phosphate, respectively. Dysregulation of this rheostat is a known factor in cancer progression and MDR [5,6]. This study investigates how pharmacologically relevant, low-dose combinations of ATRA and VD3 modulate sphingolipid gene expression and whether this creates a metabolic vulnerability that can be exploited to overcome resistance in AML cells.

Materials and methods

Cell lines

Human AML cell lines SKM-1 (derived from a 76-year-old patient) and MOLM-13 (derived from a 20-year-old patient) were used alongside their multidrug-resistant sublines SKM-1/VCR and MOLM-13/VCR. The MDR sublines were developed through long-term selection with vincristine, resulting in significant P-glycoprotein overexpression. Cells were cultured in RPMI 1640 medium supplemented with 16% fetal bovine serum and antibiotics (100 U/mL penicillin and 0,1 mg/mL streptomycin) at 37°C in a 5% CO_2 atmosphere. MDR sublines were maintained with 100 ng/mL vincristine in growth medium to preserve the resistant phenotype.

Cell exposure

Cells were treated for 4 days with 0.5 nM VD3, 100 nM ATRA, or their combination (VD3+ATRA). These concentrations were specifically chosen to reflect clinically achievable steady-state plasma levels in patients without inducing adverse effects as well as the comparable induction of respective CYP450 enzymes responsible for degradation of ATRA and VD3.

Following a 4-day pre-incubation with VD3+ATRA, cells were passaged into fresh medium and then exposed to the acid ceramidase inhibitor carmofur (4 nM – 400 μM) for 24 hours. Viability of cells was assessed by MTT assay and LC50 values were calculated using non-linear regression with a modified Hill equation: $viability = [LC50^n/(LC50^n + c^n)] \times 100\%$, where c represents the concentration of carmofur, n corresponds to the Hill coefficient, and LC50 is the concentration of carmofur that results in the death of 50% of the cells within a cell culture.

Methods

Metabolic activity and viability were quantified using the MTT assay, measuring absorbance at 540 nm. The specific mode of cell death (apoptosis vs. necrosis) was determined via flow cytometry (BD Accuri C6) using Annexin V-FLUOS (AV) and propidium iodide (PI) double staining. Cell cycle distribution was analyzed by PI staining of ethanol-fixed cells after RNase treatment employing flow cytometry.

RNA isolation and qPCR

Total RNA was isolated using TRI Reagent, quantified, and reverse-transcribed into cDNA. Gene expression was measured via quantitative PCR (qPCR) using the $2^{-\Delta\Delta CT}$ (Livak) method, focusing on sphingolipid enzymes. *RNA18S* served as the reference gene. To verify maturation at the protein level, immunophenotyping was performed using FITC-labeled antibodies against CD11b, CD14, and CD33, with analysis by flow cytometry.

Results

Exposure of AML cells to 0.5 nM VD3 and 100 nM ATRA triggered a moderate decline in overall metabolic activity across all experimental models (Fig. 1). We observed a consistent trend where the VD3+ATRA combination was more effective than single agents. Interestingly, there was a direct correlation between the cellular resistance status and the degree of metabolic inhibition. In sensitive SKM-1 and MOLM-13 cells, activity decreased by approximately 20% following combination treatment. In contrast, the MDR sublines exhibited heightened sensitivity to this priming: activity dropped by 30% in SKM-1/VCR and 22% in MOLM-13/VCR. VD3 as a single agent had a

negligible impact, causing only a 3-6% decrease, indicating ATRA as the primary driver of metabolic stress at these doses. Flow cytometric analysis revealed that the observed metabolic decline correlated with distinct death pathways based on resistance status. Drug-sensitive variants primarily underwent non-specific necrosis (AV^-/PI^+), which reached nearly 15% in SKM-1 cells. Conversely, resistant sublines favored programmed cell death pathways. SKM-1/VCR cells showed a marked shift toward early apoptosis (AV^+/PI^-), reaching 11% under ATRA treatment, while the VD3+ATRA combination triggered 12% late apoptosis/secondary necrosis (AV^+/PI^+) in the resistant MOLM-13/VCR subline.

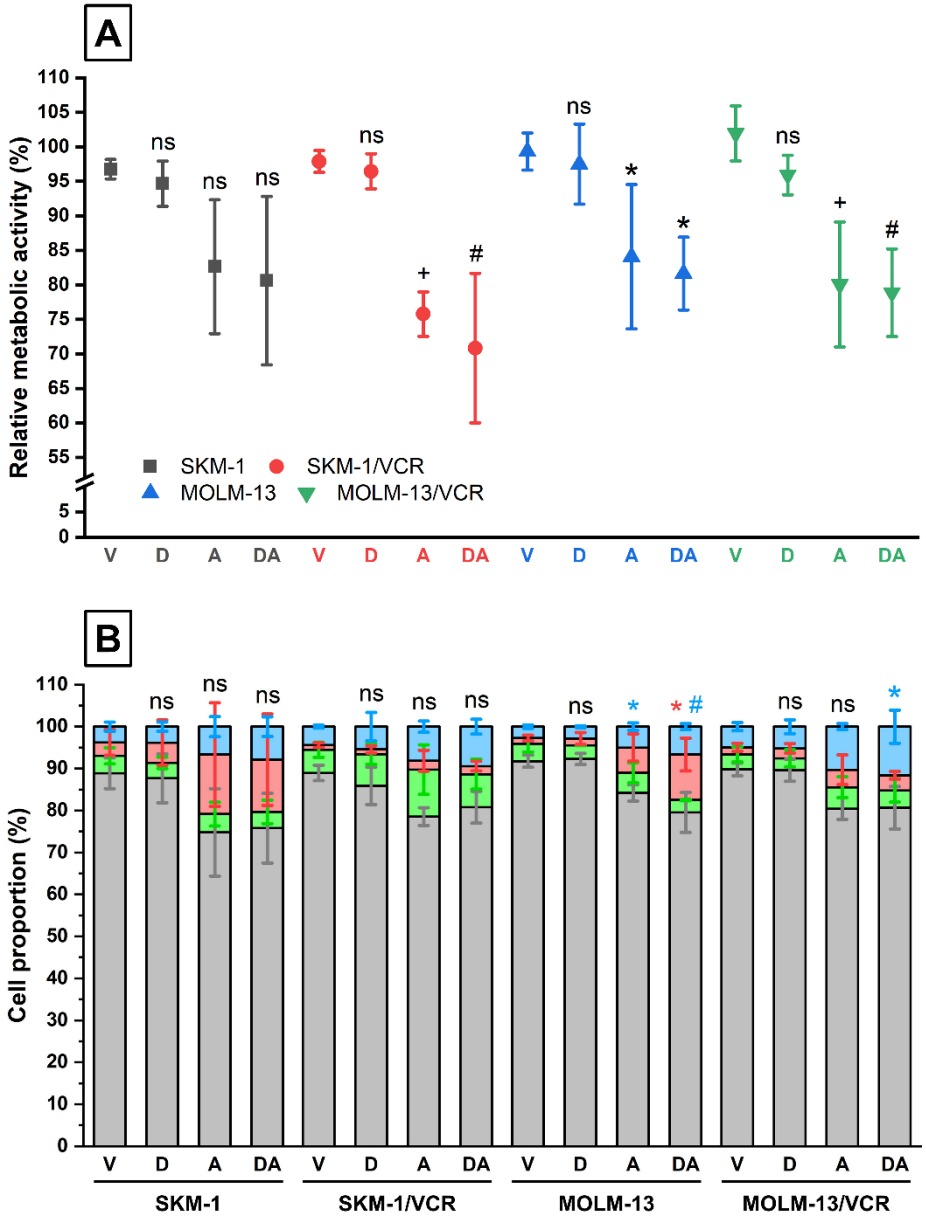

Figure 1. Cells were treated with 0.5 nM VD3 (D), 100 nM ATRA (A) or their combination (DA) for four days. 0.2 % (v/v) DMSO was used as a vehicle control (V). Panel A: MTT assay (metabolic activity) for VD3 and ATRA. Results are shown as the mean of four independent experiments ± standard deviation.

Panel B: annexin V/propidium iodide dual staining; grey: AV^-/PI^-; green: AV^+/PI^-; red: AV^-/PI^+; blue: AV^+/PI^+. Results are shown as the mean of three independent experiments ± standard deviation. Statistical significance: * $p < 0,05$;; # $p < 0,001$; ns – no significance

Despite the metabolic shifts and induced death, cell cycle analysis showed that the vitamins did not trigger significant proliferative arrest at these concentrations (Fig. 2). No statistically significant increase in the G0/G1 phase was detected across all models, although MOLM-13 variants showed a non-significant upward trend (ca. 7-10%). To further characterize the phenotypic state, we analyzed differentiation markers (CD11b, CD14, CD33) at the protein level via immunophenotyping. Representative histograms for SKM-1 cells confirmed that protein expression for all treatments remained identical to vehicle controls and was comparable to the isotype control. This lack of phenotypic maturation indicates that the cells remain in an undifferentiated blast-like state despite significant internal metabolic reprogramming.

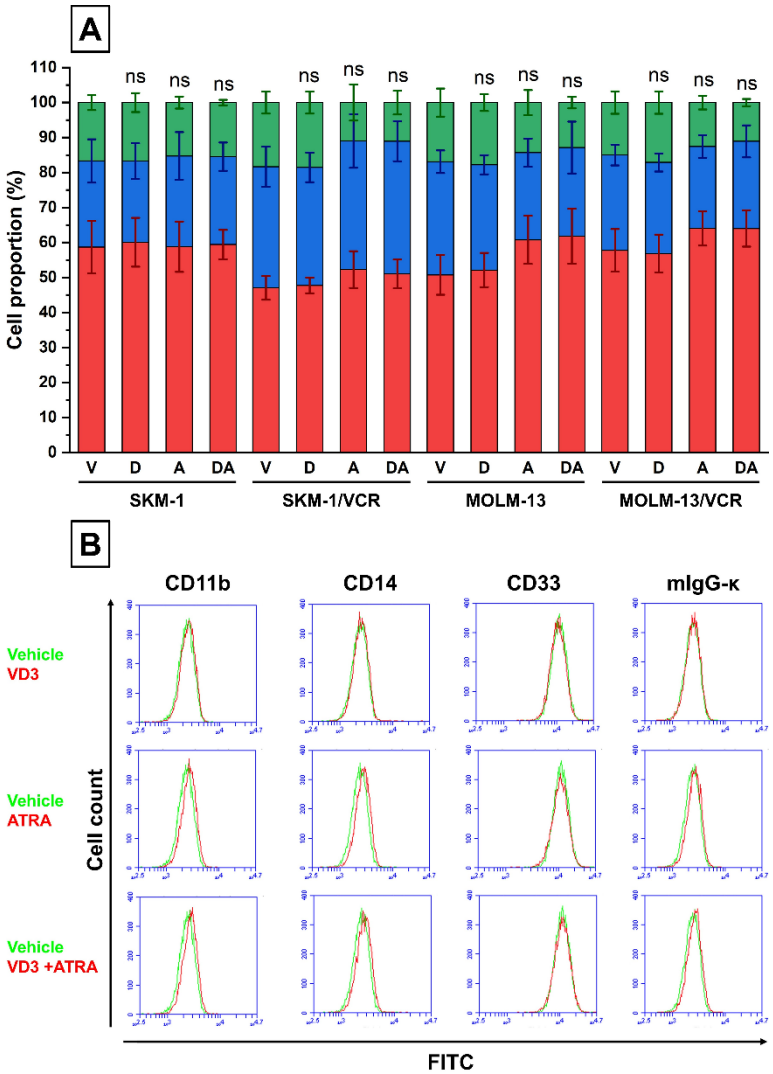

Figure 2. Cells were treated with 0.5 nM VD3 (D), 100 nM ATRA (A) or their combination (DA) for four days. 0.2 % (v/v) DMSO was used as a vehicle control (V). Panel A: cell cycle analysis; red: G0/G1 phase; blue: S phase; green: G2/M phase. Results are shown as the mean of four independent experiments ± standard deviation. Statistical significance: ns – no significance. Panel B: representative histograms show

the expression levels of differentiation markers (CD11b, CD14, CD33) in SKM-1 cells, mIgG-κ served as the isotype control. Green curves: vehicle control; red curves: cell treated with VD3 and/or ATRA.

The most striking molecular shift occurred in sphingolipid metabolism (Fig. 3).

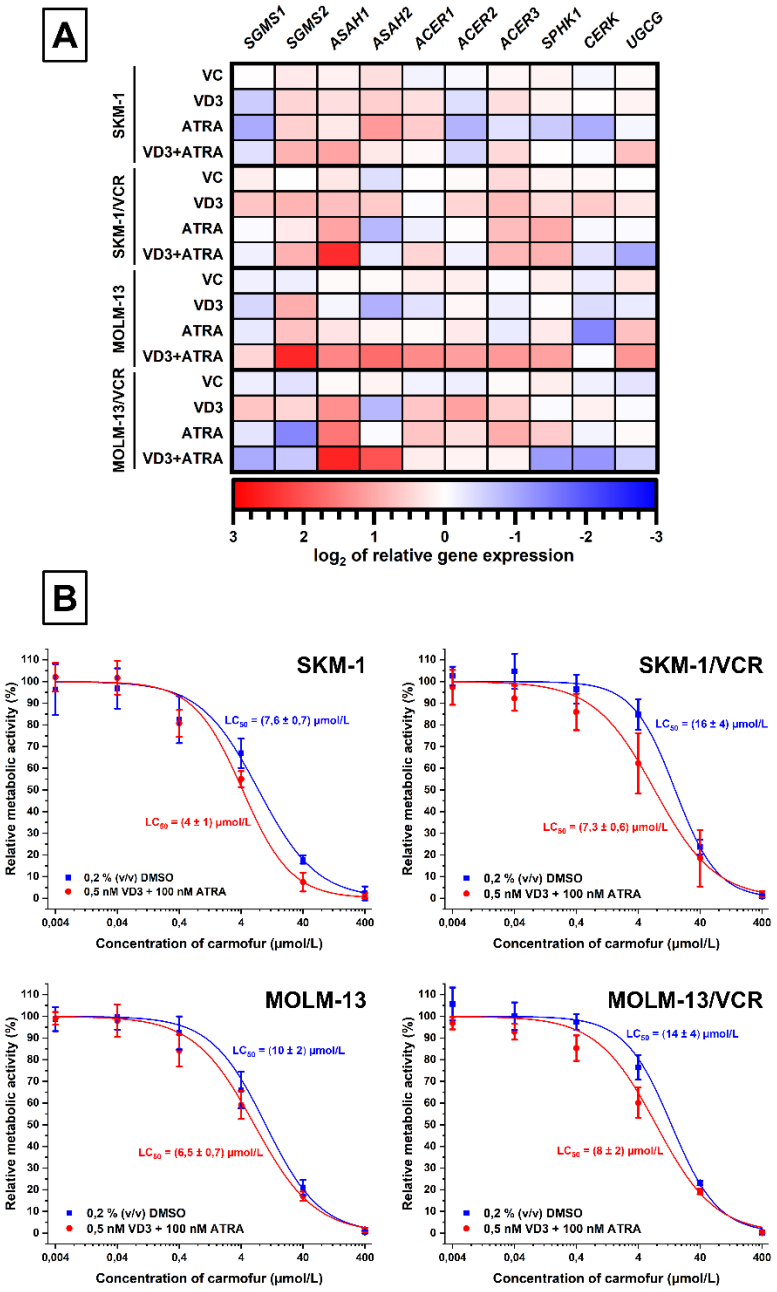

Figure 3. Panel A: the heat map depicts alterations in the relative expression of genes encoding enzymes of sphingolipid metabolism associated with cancer cell survival and drug resistance. Cells were treated with 0.5 nM VD3, 100 nM ATRA, or their combination (VD3+ATRA) for four days. 0.2 % (v/v) DMSO was used as a vehicle control and cells cultivated in the complete growth medium as the reference (calibrator) sample. Results are shown as the mean of three independent measurements. Panel B: Cells were treated with 0.2 % (v/v) DMSO or the combination of 0.5 nM VD3 and 100 nM ATRA for four days. Cells were then passaged into the fresh growth medium for 24 hours followed by the exposure to

carmofur (concentrations indicated in the figure) for additional 24 hours. Results are shown as the mean of four independent experiments ± standard deviation.

qPCR analysis revealed a remarkable upregulation of the *ASAH1* gene, encoding acid ceramidase, following VD3+ATRA treatment. This effect highly correlated with MDR status: resistant sublines exhibited a nearly 6-fold induction of *ASAH1*, whereas sensitive lines showed only a 2- to 3-fold increase. There was a direct and powerful correlation between the magnitude of *ASAH1* induction and subsequent sensitization to the inhibitor carmofur. Pre-incubation with VD3+ATRA significantly lowered values for carmofur in all lines. The most dramatic shift occurred in SKM-1/VCR, where the LC50 dropped by 9 µmol/L, while in resistant MOLM-13/VCR, it shifted from about 14 µmol/L to 8 µmol/L. These results confirm that vitamin "priming" creates a targetable metabolic dependency on acid ceramidase in resistant AML cells.

Discussion

Our findings demonstrate that pharmacologically relevant doses (0.5 nM VD3 and 100 nM ATRA) are bioactive enough to significantly alter the metabolic landscape of AML cells without the toxicity associated with high-dose differentiation therapy. The lack of terminal differentiation at the protein level (CD11b/CD14/CD33) and the absence of G0/G1 arrest suggest that the vitamins act as metabolic modulators rather than maturation inducers at these concentrations.

The massive 6-fold upregulation of *ASAH1* in MDR cells represents a critical survival strategy. Acid ceramidase degrades pro-apoptotic ceramide into sphingosine, which can be further processed into the pro-survival sphingosine-1-phosphate. By "priming" cells with VD3+ATRA, we forced them to rely on this enzymatic "safety valve" to counteract vitamin-induced stress. The direct correlation between *ASAH1* mRNA levels and the significant drop in carmofur LC50 values proves that this induced defense becomes a targetable weakness. This "prime-and-kill" strategy effectively bypasses traditional MDR mechanisms, such as P-glycoprotein-mediated efflux, by targeting the cell's underlying metabolic adaptation.

Conclusion

Low-dose combinations of VD3 and ATRA induce a specific phenotypic shift in AML cells characterized by a moderate metabolic decline and a profound upregulation of acid ceramidase (*ASAH1*), despite the absence of terminal differentiation at the protein level. This molecular change directly correlates with increased sensitivity to the inhibitor carmofur, especially in multidrug-resistant sublines. Our study highlights a novel therapeutic approach that leverages vitamin signaling to create metabolic vulnerabilities, offering a potential strategy to overcome resistance in AML.

Acknowledgement

This work was supported by grants APVV-19-0094, VEGA 2/0046/24, VEGA 2/0030/23, VEGA 2/0016/22, VEGA 2/0070/19, and the grant provided by the Slovak University of Technology in Bratislava within the Young Researchers Support Program.

References

[1] Döhner H, Weisdorf DJ, Bloomfield CD. Acute Myeloid Leukemia. New England Journal of Medicine 2015; 373: 1136-52. doi: 10.1056/NEJMra1406184.

[2] Shallis RM, Wang R, Davidoff A et al. Epidemiology of acute myeloid leukemia: Recent progress and enduring challenges. Blood Rev 2019; 36: 70-87. doi: 10.1016/j.blre.2019.04.005.

[3] Robey RW, Pluchino KM, Hall MD et al. Revisiting the role of ABC transporters in multidrug-resistant cancer. Nat Rev Cancer 2018; 18: 452-64. doi: 10.1038/s41568-018-0005-8.

[4] De Thé H. Differentiation therapy revisited. Nat Rev Cancer 2018; 18: 117-27. doi: 10.1038/nrc.2017.103.

[5] Lewis AC, Wallington-Beddoe CT, Powell JA et al. Targeting sphingolipid metabolism as an approach for combination therapies in haematological malignancies. Cell Death Discov 2018; 4: 72. doi: 10.1038/s41420-018-0075-0.

[6] Raza Y, Atallah J, Luberto C. Advancements on the Multifaceted Roles of Sphingolipids in Hematological Malignancies. Int J Mol Sci 2022; 23: 12745. doi: 10.3390/ijms232112745.

DNA METHYLATION REPROGRAMMING IN PACLITAXEL-RESISTANT BREAST CANCER

Lenka Trnkova[1], Monika Burikova[1], Andrea Soltysova[2,3], Jana Plava[1], Andrea Cumova[1], Lucia Rojikova[1], Boris Tichy[4], Vojtech Bystry[5], Florence Busato[6], Yimin Shen[7], Thomas Fleisher[8], Jorg Tost[6], Svetlana Miklikova[1], Marina Cihova[1], Verona Buocikova[1], Bozena Smolkova[1]

[1]*Department of Molecular Oncology, Cancer Research Institute, Biomedical Research Center of the Slovak Academy of Sciences, Bratislava, Slovakia*
[2]*Department of Molecular Biology, Faculty of Natural Sciences, Comenius University in Bratislava, Bratislava, Slovakia*
[3]*Department of Human Genetics, Institute for Clinical and Translational Research, Biomedical Research Center of the Slovak Academy of Sciences, Bratislava, Slovakia*
[4]*Genomics Core Facility, Central European Institute of Technology, Masaryk University, Brno, Czechia*
[5]*Bioinformatics Core Facility, Central European Institute of Technology, Masaryk University, Brno, Czechia*
[6]*Laboratory for Epigenetics & Environment, Centre National de Recherche en Génomique Humaine, CEA-Institut de Biologie François Jacob, Université Paris-Saclay, Evry, France*
[7]*Laboratory for Bioinformatics, Foundation Jean Dausset - Human Polymorphism Study Center (CEPH), Paris, France*
[8]*Department of Cancer Genetics, Institute for Cancer Research, Oslo University Hospital, Oslo, Norway*

Introduction

Breast cancer is the most prevalent female malignancy worldwide, with an expected increase in incidence due to lifestyle-related risk factors and aging population (1). Clinically, breast cancer is classified into surrogate intrinsic breast cancer subtypes based on the immunohistological staining of specific molecular markers involving estrogen receptor (ER), progesterone receptor (PR) and human epidermal growth factor receptor 2 (HER2).

The main subtypes involve hormone receptor-positive Luminal A and Luminal B (ER- and/or PR-positive) subtypes, HER2-positive breast cancer and triple-negative breast cancer (TNBC; ER-, PR- and HER2-negative). Treatment strategies are largely determined by these molecular subtypes. Particularly, TNBC represents an aggressive disease with limited treatment options due to the lack of specific molecular targets, and chemotherapy remains the main systemic treatment option. Paclitaxel (PAC) is a

microtubule-targeting chemotherapeutic agent from the taxane class. It is widely used in the treatment of TNBC as part of the anthracycline-taxane regimen, where chemotherapy represents the first-line treatment. In addition, PAC is also applied in later stages of other subtypes, such as HER2-positive breast cancer (2).

However, the efficacy of standard breast cancer therapies, including chemotherapy, is often limited by the emergence of drug resistance. Drug resistance can arise due to various mechanisms including changes in drug metabolism, cell survival signaling pathways or DNA repair mechanisms (3). Resistance to microtubule-targeting agents is often associated with changes in tubulin structure, gene expression and post-translational modifications. Similarly, PAC resistance has been linked to increased expression of the ATP-binding cassette transporter gene ABCB1, a well-known mediator of multidrug resistance (4).

Accumulating evidence suggests that, besides genetic alterations, epigenetic mechanisms play a critical role in resistance acquisition (5). DNA methylation changes can alter gene expression, promote tumor adaptation under therapeutic pressure, and contribute to the emergence of resistant phenotypes. Although several studies have investigated mechanisms of PAC resistance (6), genome-wide characterization of DNA methylation remodeling in resistant TNBC models remains limited. The aim of this study was to investigate the role of DNA methylation in the acquisition of PAC resistance in BC.

Materials and methods

Cell lines

Two breast cancer cell lines, MDA-MB-231 and JIMT-1, representing TNBC and HER2-positive subtypes, respectively, were used to generate PAC-resistant (pacR) cells. Resistance was induced by continuous exposure to gradually increasing concentrations of PAC until reaching final PAC concentrations of 20 ng/ml (MDA-MB-231) and 19 ng/ml and (JIMT-1). Cells were cultured in Dulbecco's Modified Eagle's Medium high glucose, supplemented with 10% fetal bovine serum, 2 mM glutamine, penicillin–streptomycin solution and 2.5 µg/mL amphotericin B.

Cell viability assay

Sensitivity of parental and pacR cells to PAC monotherapy and combined treatment with decitabine (DAC) and PAC (DAC+PAC) or doxorubicin (DOX; DAC+DOX) was assessed using CellTiter-Glo® Luminescent Cell Viability Assay according to manufacturer´s instructions. Cell viability following PAC monotherapy was measured upon 6 days of drug exposure. In case of combination treatment, cells were exposed to DAC for 24 hours, followed by PAC or DOX treatment for 5 days. Resulting IC50 values and combination index (CI) were calculated using Calcusyn software. $CI < 1$ indicates synergy, $CI = 1$ additive effect, and $CI > 1$ antagonism.

RT-PCR

Expression of genes associated with drug resistance and epigenetic regulation was assessed using reverse transcription quantitative polymerase chain reaction (RT-qPCR). Following RNA isolation, cDNA was synthesized and used for RT-qPCR analysis with 50 ng of cDNA input. TaqMan assays were used for *DNMT1*, *DNMT3A*, *DNMT3B*,

TET1, *TET2*, *TET3*, *CDA*, and *GAPDH*, while *DCK* and *RPLP0* expression was assessed using in-house designed primers. Relative gene expression was calculated using the ΔΔCT method with *GAPDH* or *RPLP0* used as reference genes.

In vivo experiments

In vivo experiments were performed using SCID beige mice. Mice were housed in the authorized animal facility (SK UCH 02022). The Institutional Ethical Committee and State Veterinary and Food Administration of the Slovak Republic approved this study (registration number 3616/18–221/3). All animal experiments were performed in accordance with institutional guidelines and approved protocols. To generate orthotopic xenografts, mice were injected with parental or pacR MDA-MB-231 cells. Tumor-bearing mice were treated with DAC, DOX, or their combination according to the scheme illustrated in Fig. 1, 2. Tumor size was regularly measured using caliper and tumor volume was calculated using the formula: tumor volume (mm^3) = $1/6\pi$ × tumor length (mm) × tumor width (mm) × [tumor length (mm) + tumor width (mm)]/2. Mice were sacrificed upon completion of the treatment schedule or at humane endpoint defined as the time when at least one of the tumors in the group reached a size of 1000 mm^3 and ulceration of the tumor, significant weight loss and signs of distress appeared. Tumor weights were determined upon autopsy.

RNA isolation and gene expression

RNA was isolated from snap-frozen tumor tissue with on-column DNA digestion step. RNA-seq libraries were prepared from 500 ng of total RNA. Libraries were sequenced in single-end mode using Illumina technology, generating 11-13 million reads per sample. Quality-checked and preprocessed reads were aligned to the human reference genome with gene annotation (GRCh38-p10). Differential gene expression analysis was performed using DESeq2. Differentially expressed genes were identified using an adjusted p-value < 0.05 and |fold change| > 1.5

DNA methylation analysis

DNA was isolated from snap-frozen tumor tissue. In total, 1 μg of genomic DNA was bisulfite treated and used for genome-wide DNA methylation analysis performed using the Infinium Human Methylation EPIC BeadChip covering >850 000 CpG sites. Data analysis was performed using the Bioconductor ChAMP package. Differentially methylated CpGs (DMP) were identified using an adjusted p-value < 0.05 and $|\Delta\beta| > 0.1$. Integrative analysis of DNA methylation and transcriptomic data was performed using Pearson correlation. A significant correlation was defined as an inverse correlation coefficient of $r < -0.3$ and an adjusted p-value < 0.05.

Clinical validation of DNA methylation

Clinical validation of DNA methylation changes was performed by reanalyzing the data from the NeoAva phase II clinical trial (NCT00773695) involving 132 breast cancer patients treated with chemotherapy alone or chemotherapy combined with bevacizumab. Chemotherapy consisted of the FEC100 (5-fluorouracil, epirubicin, cyclophosphamide) regimen followed by either docetaxel or PAC as described in (7). Genome-wide DNA methylation profiling was performed using the Human Infinium Methylation EPIC version 1.0 BeadChip array (8).

Results

Cell viability assay was used to assess the sensitivity of parental and resistant cells towards the PAC. MDA-MB-231 pacR and JIMT-1 pacR cells showed decreased sensitivity following the 6-day PAC treatment compared to their parental counterparts. The fold change of PAC IC50 values was 4.7 in MDA-MB-231 pacR cells and 6.3 in JIMT-1 pacR cells relative to their parental cells.

RT-qPCR analysis revealed deregulation of multiple genes associated with drug resistance and DNA methylation. MDA-MB-231 pacR cells showed upregulations of *DNMT3A*, *TET1*, *TET2* and *TET3*, while *DNMT1* and *CDA* were downregulated, relative to the parental cells. On contrary, we observed downregulation of *TET1*, *TET2* and *DCK* genes in JIMT-1 pacR cells.

Based on the observed changes in gene expression of epigenetic modulators we further tested genome-wide DNA methylation changes in mouse xenografts originating from MDA-MB-231 parental and pacR cells. Using the Infinium Human Methylation EPIC BeadChip (covering >850,000 CpG sites), we observed 230 052 DMPs in MDA-MB-231 pacR xenografts when compared to MDA-MB-231 parental xenografts. Out of these DMPs, 180 106 (78.3 %) were hypermethylated and 49 946 (21.7 %) were hypomethylated in MDA-MB-231 pacR xenografts. Based on the integrative analysis, we identified 1424 hypermethylated and 357 hypomethylated CpG sites located in regulatory regions, including CpG islands, shores, and shelves, affecting 411 hypermethylated and 177 hypomethylated unique genes.

Subsequently, we tested the potential of DNA methyltransferase inhibitor DAC to enhance cytotoxic effect of chemotherapy. In vitro, we pre-treated parental and pacR MDA-MB-231 cells with IC20 concentration of DAC (1.2-4.8 ng/mL for MDA-MB-231 parent and 10-30 ng/mL for MDA-MB-231 pacR) for 24 hours followed by 5-day treatment with either PAC or DOX. In MDA-MB-231 parental cells, combined treatment of DAC+DOX resulted in consistent synergistic effect (CI < 1). Similarly, DAC+PAC combination resulted in synergistic effect except for two concentrations where the effect was additive (CI = 1). in MDA-MB-231 pacR cells, the combination of DAC+DOX yielded mostly synergistic effects, while DAC+PAC combination showed higher CI values and, in multiple cases, resulted in antagonistic effect (CI > 1). In vivo, MDA-MB-231 parental xenografts treated with DAC+DOX therapy showed reduced tumor volumes and tumor weights compared to vehicle treatment or DAC and DOX monotherapy (Fig 1).

In a prolonged treatment schedule, MDA-MB-231 pacR xenografts treated with DAC+DOX combination showed reduced tumor volume compared to vehicle treatment, and reduced tumor weights compared to vehicle treatment and DOX monotherapy (Fig. 2). In MDA-MB-231 parental xenografts, DAC monotherapy resulted in 98 782 hypomethylated DMPs (98.3 % of all DMPs). Out of these, 139 hypomethylated DMPs (located in regulatory regions) were inversely correlated with 68 upregulated genes. In MDA-MB-231 pacR xenografts treated with the same treatment schedule, DAC monotherapy resulted in 207 448 hypomethylated DMPs (97.4 % of all DMPs). Furthermore, 592 hypomethylated DMPs (located in regulatory regions) was inversely correlated with 161 upregulated genes.

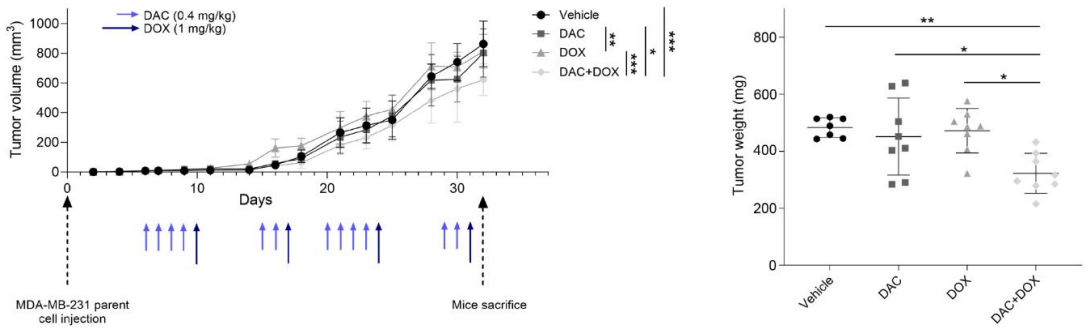

Figure 1: Tumor volumes of MDA-MB-231 parental xenografts over time, with an indication of treatment schedule and tumor weights for each treatment group. Adapted from (7).

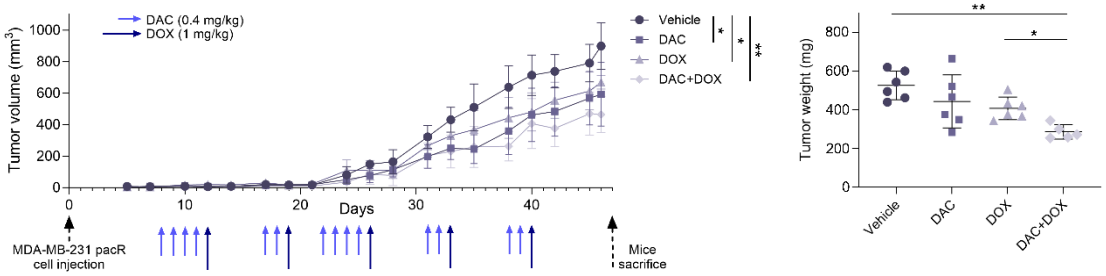

Figure 2: Tumor volumes of MDA-MB-231 pacR xenografts over time, with an indication of extended treatment schedule and tumor weights for each treatment group. Adapted from (7).

To validate the observed changes in MDA-MB-231 pacR xenografts, we reanalyzed DNA methylation data from the NeoAva clinical trial involving breast cancer patients treated with chemotherapy (FEC100 regimen followed by docetaxel or PAC) with or without the bevacizumab treatment. Differential DNA methylation analysis of tumor biopsies collected at the end of treatment, stratified by pathological complete response (pCR), identified 3 820 DMPs (located in regulatory regions) mapping to 1 646 genes. Of these, 2831 DMPs (74.1 %) were hypermethylated in non-pCR patients and 989 (25.9 %) were hypomethylated.

Discussion

Therapy resistance remains a major challenge in breast cancer treatment. In this study, we derived pacR breast cancer cell lines of two distinct molecular subtypes. To investigate the contribution of epigenetic mechanisms to the acquisition of chemotherapy resistance, we first analyzed the expression of genes associated with DNA methylation and observed dysregulation of several epigenetic regulators in pacR cells. Subsequent genome-wide DNA methylation profiling revealed extensive DNA methylation changes in MDA-MB-231 pacR xenograft model. Furthermore, the analysis

of the NeoAva clinical cohort revealed an association between DNA methylation alterations and therapeutic response. However, the most pronounced deregulation of DNA methylation was observed during the early stages of the treatment, while changes during the subsequent taxane phase were comparatively modest (8).

Epigenetic regulators are increasingly recognized as therapeutic targets in oncology, and multiple studies have demonstrated that their pharmacological modulation can enhance tumor cell sensitivity to therapy (5). This is consistent with our previous work showing that inhibition of DNA methylation using DAC potentiates the effects of cytotoxic chemotherapy in preclinical breast cancer models (9). Therefore, we further evaluated the ability of DAC to sensitize MDA-MB-231 pacR cells to chemotherapy. Our data indicate that DAC enhances efficacy of chemotherapy that is unrelated to resistance-inducing agent. Moreover, DAC induces widespread DNA hypomethylation, with implications on gene expression programs. However, future studies exploring candidate genes or pathways will be required to better clarify their causal relationships and contribution to the acquisition of drug resistance.

Conclusion

This work highlights epigenetic and transcriptomic alterations associated with PAC resistance in breast cancer. The obtained findings provide new insights into the complexity of PAC resistance and offer a foundation for refining therapeutic approaches in treatment-refractory breast cancer.

Acknowledgement

This work presents data previously reported in (7). This research was financially supported by the ERACoSysMed project RESCUER, VEGA 1/0434/24, VEGA 2/0067/22, and ANR-19-SYME-0001–05. We acknowledge the Genomics Core Facility and Bioinformatics Core Facility of CEITEC Masaryk University of A4L_ACTIONS, supported by the European Union's Horizon 2020 under grant agreement No. 964997.

References

[1] Bray F, Laversanne M, Sung H, Ferlay J, Siegel RL et al. Global cancer statistics 2022: GLOBOCAN estimates of incidence and mortality worldwide for 36 cancers in 185 countries. CA Cancer J Clin. 2024;74(3):229-263. doi: 10.3322/caac.21834.

[2] Gennari A, André F, Barrios CH, Cortés J, de Azambuja E et al. ESMO Clinical Practice Guideline for the diagnosis, staging and treatment of patients with metastatic breast cancer. Ann Oncol. 2021;32(12):1475-1495. doi: 10.1016/j.annonc.2021.09.019.

[3] Khan SU, Fatima K, Aisha S, Malik F. Unveiling the mechanisms and challenges of cancer drug resistance. Cell Commun Signal. 2024;22(1):109. doi: 10.1186/s12964-023-01302-1.

[4] Němcová-Fürstová V, Kopperová D, Balušíková K, Ehrlichová M, Brynychová V et al. Characterization of acquired paclitaxel resistance of breast cancer cells and involvement of ABC transporters. Toxicol Appl Pharmacol. 2016;310:215-228. doi: 10.1016/j.taap.2016.09.020.

[5] Trnkova L, Buocikova V, Mego M, Cumova A, Burikova M et al. Epigenetic deregulation in breast cancer microenvironment: Implications for tumor progression and therapeutic strategies. Biomed Pharmacother. 2024;174:116559. doi: 10.1016/j.biopha.2024.116559.

[6] Abouzeid HA, Kassem L, Liu X, Abuelhana A. Paclitaxel resistance in breast cancer: Current challenges and recent advanced therapeutic strategies. Cancer Treat Res Commun. 2025;43:100918. doi: 10.1016/j.ctarc.2025.100918.
[7] Trnkova L, Burikova M, Soltysova A, Ficek A, Plava J et al. Molecular profiling of chemotherapy-resistant breast cancer reveals DNA methylation remodeling associated with the acquisition of paclitaxel resistance. Drug Resist Updat. 2026;85:101350. doi: 10.1016/j.drup.2026.101350.
[8] Fleischer T, Haugen MH, Ankill J, Silwal-Pandit L, Børresen-Dale AL et al. An integrated omics approach highlights how epigenetic events can explain and predict response to neoadjuvant chemotherapy and bevacizumab in breast cancer. Mol Oncol. 2024;18(8):2042-2059. doi: 10.1002/1878-0261.13656.
[9] Buocikova V, Longhin EM, Pilalis E, Mastrokalou C, Miklikova S et al. Decitabine potentiates efficacy of doxorubicin in a preclinical trastuzumab-resistant HER2-positive breast cancer models. Biomed Pharmacother. 2022;147:112662. doi: 10.1016/j.biopha.2022.112662.

PULMONARY ADVERSE EVENTS ASSOCIATED WITH TRASTUZUMAB DERUXTECAN IN HER2-POSITIVE METASTATIC BREAST CANCER: A REAL-WORLD ANALYSIS OF THE FDA ADVERSE EVENT REPORTING SYSTEM (2020-2025)

Ekram Hassan Hasanin

Faculty of Medicine, University of Tripoli, Tripoli, Libya

Introduction

Trastuzumab deruxtecan is an effective treatment for HER2-positive metastatic breast cancer, offering significant survival benefits. However, it poses risks of serious adverse effects, notably interstitial lung disease (ILD) and pneumonitis, concerns regarding pulmonary safety are rising, indicating the need for surveillance using large databases to evaluate the real-world incidence and severity of these complications.

Methods

FAERS reports involving trastuzumab deruxtecan patients with HER2-positive metastatic breast cancer reported between 2020 and 2025 were retrospectively analyzed. Cases of interstitial lung disease (ILD) and pneumonitis were identified using MedDRA preferred terms after duplicate removal according to FDA recommendations. Descriptive statistics were used to summarize patient characteristics, seriousness, and clinical outcomes

Results

A total of 462 FAERS reports involving trastuzumab deruxtecan were identified. Interstitial lung disease (ILD) and/or pneumonitis were reported in 267 cases (57.8%), including 192 ILD, 64 pneumonitis, and 11 reports of both conditions. Most of ILD/pneumonitis cases were classified as serious (94.0%), with hospitalization in 52.8% and death reported in 34.8% of cases. Life-threatening outcomes were documented in 12.4%. Mortality was higher in reports describing both ILD and pneumonitis (54.5%) compared with ILD alone (37.5%) or pneumonitis alone (23.4%). All ILD/pneumonitis reports occurred in female patients, and HER2-positive breast cancer was the most frequently reported indication.

Conclusion

Interstitial Lung Disease and pneumonitis represent frequent and severe adverse events reported with trastuzumab deruxtecan, with a high proportion of serious outcomes, hospitalizations, and deaths in real-world FAERS data. These findings underscore the need for vigilant pulmonary monitoring during treatment.

HIGH-SENSITIVITY ELECTROCHEMICAL DETECTION OF HUMAN CYTOMEGALOVIRUS IN ONCOLOGICAL DISEASES

Aneta Fried[1, 2], Karolína Itterheimova[1, 2], Ludmila Moranova[1], Martin Bartosik[1]

[1]*Research Centre for Applied Molecular Oncology, Masaryk Memorial Cancer Institute, Žlutý kopec 7, 656 53 Brno, Czech Republic*
[2]*National Centre for Biomolecular Research, Faculty of Science, Masaryk University, Kamenice 5, 625 00 Brno, Czech Republic*

Human cytomegalovirus (hCMV), a herpesvirus with a global prevalence of approximately 90 %, establishes lifelong latency in the host and can reactivate under immunosuppressive conditions. In oncology, hCMV is increasingly recognized for its oncomodulatory properties, particularly in glioblastoma IDH-wildtype or breast cancer1. hCMV promotes tumor progression by modulating the tumor microenvironment, suppressing the host immune response, and interfering with key oncogenic signaling pathways. Recent clinical evidence suggests that hCMV-positive glioblastoma patients receiving the antiviral valganciclovir alongside standard therapy exhibit improved survival rates2. However, the reported prevalence of hCMV in tumor tissues varies drastically from 0 to 100 % depending on the methodology and biological material3. Traditional techniques like immunohistochemistry (IHC) and ELISA often lack the necessary sensitivity and specificity for clinical oncology.

This study aims to develop a rapid, cost-effective, and selective electrochemical (EC) bioassay to improve the reliability of hCMV detection in clinical samples by combining isothermal amplification techniques (IATs) with EC readout. We evaluated and compared PCR and IATs, specifically loop-mediated isothermal amplification (LAMP) and recombinase-polymerase amplification (RPA), coupled with EC detection. The assay utilizes carboxylic magnetic beads modified with sequence-specific capture probes for selective target DNA immobilization. Following enzymatic labeling with a peroxidase polymer, the addition of a substrate containing hydrogen peroxide and hydroquinone enables the EC readout.

The optimized EC bioassay demonstrated excellent selectivity and achieved a limit of detection (LOD) of 10 pM. The entire workflow from sample processing to readout was completed within 2 hours. Experimental results confirmed that the bioassay could successfully distinguish between hCMV-positive and hCMV-negative cancer cell lines. By eliminating the need for thermal cycling through IATs, the workflow is significantly faster and more straightforward than traditional qPCR. These findings demonstrate the potential of EC-based bioassays as sensitive, affordable, and rapid tools for hCMV detection in clinical samples. This technology offers a promising path toward standardized diagnostics that could allow for personalized antiviral interventions for cancer patients.

Acknowledgement:

This work was supported by MH CZ - DRO (MMCI, 00209805), GAČR (25-15990S), AZV ČR (NU23J-08-00006, 2023-2026), BBMRI.CZ (no. LM2023033) and OP JAC (CZ.02.01.01/00/22_008/0004644).

References:

[1] Geisler J., Touma J., Rahbar A., Söderberg-Nauclér C., Vetvik. K.: Cancers, 11 (2019) 1842.
[2] Stragliotto G., Pantalone M., Rahbar A., Bartek J., Söderberg-Naucler C.: Clin. Cancer Res., 26 (2020) 4031-4039.
[3] Garcia-Martinez, A., Alenda, C., Irles, E., Ochoa, E., Quintanar, T., Rodriguez-Lescure, A., Soto, J. L., Barbera, V. M.: Virol J. 14 (2017).

ROLE OF THE SODIUM/CALCIUM EXCHANGER TYPE 3 IN CANCER CELLS

Kristina Galvankova[1], Ingeborg Rezuchova[2], Ladislav Klena[1], Marian Grman[1], Simona Gazova[1], Veronika Liskova[1], Zuzana Kozovska[3], Ladislav Roller[4], Petr Babula[5], Olga Krizanova[1,5]

[1]*Institute for Clinical and Translational Research, Biomedical Research Center, Slovak Academy of Sciences, Bratislava, Slovakia*
[2]*Institute of Virology, Biomedical Research Center, Slovak Academy of Sciences, Bratislava, Slovakia*
[3]*Institute of Experimental Oncology, Biomedical Research Center, Slovak Academy of Sciences, Bratislava, Slovakia*
[4]*Institute of Zoology, Slovak Academy of Sciences, Bratislava, Slovakia*
[5]*Department of Physiology, Faculty of Medicine, Masaryk University, Brno, Czech Republic*

Sodium/calcium exchanger (NCX) is a membrane protein transporting calcium ions against sodium ions in two operating modes, forward (calcium ions out of the cell) and reverse (calcium ions into the cell). Three types of NCX were described – 1, 2 and 3, with type 1 NCX playing significant role in various tumors, especially under hypoxic conditions in solid tumors in reverse mode. However, little is known about type 2 and type 3 NCX in tumorigenesis. This study has shown the importance of NCX3 in processes, which are considered hallmarks of cancer – apoptosis resistance, proliferation and migration. Selective NCX3 blocker YM-244769 was used to study the effect of NCX3 in four different cancer cell lines, DLD1 (colorectal), HeLa (cervical), MDA-MB-231 (triple negative breast cancer) and JIMT1 (HER2+ breast cancer). NCX3 blockade, but not NCX1 blockade (by selective SEA0400 blocker), resulted in increased apoptosis in a concentration dependent manner, decreased proliferation and suppressed migration potential in all four cancer cell lines, especially breast cancer cells. Hypoxic conditions chemically induced by dimethyloxalylglycine didn´t cause any additional effect. To verify specific role of NCX3 in these processes, we generated MDA-MB-231 cell line with knocked-out SLC8A3 gene (NCX3) using CRISPR/Cas9 technology and observed the same results. We further focused on energy metabolism and found out that cellular respiration was significantly decreased in NCX3 knock-out cells compared to wild type. Taken together, these data clearly show the anti-apoptotic, proliferative and pro-migratory role of NCX3 in cancer cells, probably through disruption of mitochondria morphology and thus energy metabolism. Further research is needed to determine the exact mechanism responsible for supporting cancer cells survival and fate.

Acknowledgement
This work was supported by the grants of the Slovak Research and Development Agency APVV-20-0176 and Research Grant Agency of the Ministry of Education, Science, Research and Sport of the Slovak Republic and Slovak Academy of Sciences VEGA 2/0040/22 and VEGA 2/0030/25

COMBINED TREATMENT OF PROPRANOLOL AND CAMPTOTHECIN DIFFERENTLY AFFECTS MITOCHONDRIAL FUNCTION IN BREAST AND COLORECTAL CANCER CELLS

Simona Gazova[1], Ladislav Klena[1], Kristina Galvankova[1], Ladislav Roller[2], Petr Babula[3], Miroslav Balaz[4], Olga Krizanova[1,3]

[1]Institute of Clinical and Translational Research, Biomedical Research Center SAS, Bratislava, Slovakia,
[2]Institute of Zoology, SAS, Bratislava, Slovakia
[3]Department of Physiology, Faculty of Medicine, Masaryk University, Brno, Czech Republic,
[4]Institute of Experimental Endocrinology, Biomedical Research Center SAS, Bratislava, Slovakia

Increased β-adrenergic signalling due to chronic stress plays a role in the promotion of tumorigenesis. Therefore, the possibility of using β-adrenergic receptor blockers in cancer therapy is studied intensively, however the results remain ambiguous. The focus of this work was on the effect of combination therapy of a non-specific β-blocker, propranolol (PRO), and camptothecin (CPT). We compared the responses of such therapies in vitro on two cancer cell lines: HER2-positive breast cancer (JIMT1) and colorectal adenocarcinoma cancer (DLD1).

The effect of combination therapy was more pronounced in JIMT1 cells. Viability decrease in JIMT1 cells even after PRO only treatment was significant, while in the DLD1 cell line the drop in viability was only by 20%. Apoptosis rates in JIMT1 cells were boosted by the combination treatment, while in DLD1 cells, PRO+CPT did not have this effect. Combination treatment in both cell lines resulted in swelling of mitochondria along with a decrease in oxygen consumption rate and maximal and ATP dependent respiration, though in JIMT1 cells the decrease was notably robust. Greater depolarization of the mitochondrial membrane was observed in the JIMT1 cell line upon PRO+CPT. Reactive oxygen species generation significantly increased after PRO+CPT when compared to CPT in JIMT1 cells but decreased in DLD1 cells, further promoting differences between the two cell lines. To elucidate the mechanism explaining the observed effect, we measured levels of total phospho-protein, phospho-CREB, CREB, and β-catenin. PRO by itself slightly decreased activity of CREB, an effect further augmented by CPT, but not by PRO+CPT. Taken together with changes in β-catenin levels, we propose the hypothesis that in JIMT1 cells phospho-CREB signaling targets β-catenin.

To conclude, this study suggests PRO as an adjuvant therapy to CPT in breast cancer, while not having the same effect on colorectal cancer. PRO seems to disturb mitochondrial metabolism by itself. On top of that, PRO amplifies the effect of CPT in

the HER2-positive breast cancer cell line (JIMT1) by attacking mitochondrial energetics, metabolism, and membrane. This work proposes mitochondria as possible targets in breast tumors connected to β-adrenergic regulation.

Acknowledgement

This work was supported by grants APVV-20-0176, VEGA 2/0030/25 and VEGA 2/0128/23.

PSORIASIS-LIKE DISEASE PREVENTS SQUAMOUS SKIN TUMOR DEVELOPMENT BY NEUTROPHIL-DRIVEN INFLAMMATION

Panagiota Tsokkou[1], Martin Holcmann[2], Katharina Rindler[1], Kamil Mieczkowski[3], Lisa Shaw[1], Matthias Farlik[1], Maria Sibilia[2], Erwin F. Wagner[1,3]

[1]*Department of Dermatology, Medical University of Vienna, 1090 Vienna, Austria*
[2]*Center for Cancer Research, Comprehensive Cancer Center, Medical University of Vienna, 1090 Vienna, Austria*
[3]*Department of Laboratory Medicine, Medical University of Vienna, 1090 Vienna, Austria*

Psoriasis is a chronic inflammatory skin disease affecting millions of people worldwide. Although growing evidence links chronic inflammation with increased cancer risk, the association between psoriasis and cutaneous squamous cell carcinoma (cSCC) is still elusive. Using cell transplantation and chemical-induced models of cSCC combined with inducible genetically engineered mouse models (GEMMs) of psoriasis, we investigated how chronic skin and systemic inflammation affect squamous skin tumor initiation and progression. Here, we show that in the context of severe psoriasis-like disease, neutrophil-dependent inflammation prevents squamous skin tumor development. Cellular and molecular analyses of psoriasis-like skin at the tumor initiation stage revealed a marked infiltration of CD54–expressing neutrophils, associated with the release of cytotoxic granules and neutrophil extracellular traps (NETs), as well as enhanced senescence and the expression of senescence-associated secretory phenotype (SASP) in keratinocytes. Furthermore, single-cell RNA sequencing demonstrated that inflammatory N1-like neutrophils mediate re-programming of the cell-cell communication networks, while keratinocytes displayed diminished responsiveness to mitogenic signals, including EGF and WNT. Importantly, neutrophil depletion ameliorated psoriasis-like inflammation, abolished the senescence-like phenotype in keratinocytes, and restored tumor growth. We propose that the release of neutrophil granules and NETs in psoriasis-like skin eliminates tumor cells and/or mediates oxidative and inflammatory stress-induced senescence in keratinocytes, thereby preventing tumor growth. Taken together, we have defined an innate control of skin tumorigenesis in psoriasis-like disease, which will be relevant for developing cancer prevention strategies.

Acknowledgement
This project was mainly funded by the H2020-MSCA (ITN-2019-859860-CANCERPREV) and the ERC (AdG-2016-741888-CSI-Fun).

TARGETING ENDOPLASMIC RETICULUM STRESS TO OVERCOME IMMUNOSUPPRESSION AND ENHANCE IMMUNOTHERAPY IN OVARIAN CANCER

Barbora Vavrusakova[1,2], Alica Zachejova[1,3], Marie Kundratova[1,3], Kamila Souckova[4], Lukas Pecinka[1], Lenka Krejci[1], Michal Uher[1], Katerna Sumberova[1], Matej Jasik[4], Tana Machackova[4], Renata Bartosova[1,2], Nadezda Vaskovicova[2], Katerina Vasickova[2], Tomas Kazda[1], Lukas Moran[1,2], Marek Svoboda[1]

[1]*Masaryk Memorial Cancer Institute, Žlutý kopec 7, 656 53 Brno*
[2]*Faculty of Medicine, Masaryk University, Kamenice 753/5, 625 00 Brno*
[3]*Faculty of Science, Masaryk University, Kamenice 753/5, 625 00 Brno*
[4]*Central European Institute of Technology, Masaryk University, Kamenice 753/5, Brno*

Ovarian Cancer (OC) remains one of the most lethal gynecological malignancies, characterized by late-stage diagnosis and a high rate of recurrence. While immunotherapy has transformed the treatment landscape for many cancers, its efficacy in OC has been hindered by a hostile Tumor Immune Microenvironment (TIME; Emmanuelli et al., 2024). This study explores the pivotal role of Endoplasmic Reticulum Stress (ERS) modulation in reshaping the TIME of OC. By utilizing in vitro models and a syngeneic in vivo murine model, we evaluated how ERS modulation can influence tumor progression and immune response.

We identified the impact and potential of ERS modulation in cancer–immune co-cultures. We characterized the expression of key ERS-related genes and their translational level and spatial localization. These findings were applied to model the effects of dendritic cell vaccine immunotherapy in OC in vivo. In an OC murine model, the combination of ERS modulation and a Dendritic Cell Vaccine (DCV) achieved the greatest reduction in tumor burden, decreasing both tumor volume and weight by 40%. This synergy was characterized by a shift in the immune profile: a reduction in immunosuppressive markers in the spleen and an increase in pro-apoptotic signaling and CD3+ T-cell infiltration within the tumor tissue. Our results demonstrate that ERS modulation reconfigures the TIME to enhance the antitumor activity of immune cells, thereby improving immunotherapy efficacy. By attenuating systemic immunosuppression, ERS-targeted therapies could overcome the "cold" immune nature of many cancers. This study provides a strong mechanistic rationale for combining ERS modulators with immunotherapy to enhance therapeutic outcomes in resistant OC phenotypes.

Acknowledgement
Supported by the Ministry of Health of the Czech Republic, grant nr. NU21-03-00539. All rights reserved. Supported by the SALVAGE project (OP JAC; reg. no. CZ.02.01.01/00/22_008/0004644) – co-funded by the European Union and by the State Budget of the Czech Republic. Supported by MH CZ - DRO (Masaryk Memorial Cancer Institute; 00209805).

GENE EXPRESSION PROFILE CHANGES IN SEROUS OVARIAN CANCER PATIENTS WITH VARYING LEVELS OF P53 AGGREGATES

Nicole Heinzl[1], Monika Heinzl[2, 3], Hannah Holzer[1], Robert Zeillinger[1]

[1]Department of Obstetrics and Gynecology, Molecular Oncology Group, Comprehensive Cancer Center-Gynecologic Cancer Unit, Medical University of Vienna, Austria
[2]Research Institute of Molecular Pathology (IMP), Vienna BioCenter (VBC), Vienna, Austria.
[3]Vienna BioCenter PhD Program, Doctoral School of the University of Vienna and Medical University of Vienna, Vienna, Austria

Background

TP53 mutations occur in 47.8% of ovarian cancers (OC), with serous OC the most common subtype (~80%). Recent evidence suggests that mutant p53 forms amyloid-like aggregates, which have been commonly found in neurodegenerative diseases. The pathological aggregation of these aggregates may abrogate the wild-type tumor suppressive functions of p53 and can contribute to tumor progression. Surprisingly, our recent findings showed that high levels of p53 aggregation are associated with improved survival in OC patients compared with those with no or moderate aggregation in their primary tumors. [1]. In the present study, we performed RNA-seq on this patient cohort to elucidate the underlying mechanisms and understand differences in survival outcomes.

Material and Methods

We performed RNA-Seq on a cohort of 85 serous ovarian cancer patients with known p53 aggregation status. Sequencing libraries were prepared at the Biomedical Sequencing Facility (BSF, Center for Molecular Medicine, Vienna, Austria) and sequenced on an Illumina NovaSeq 6000 S2 flow cell (2x50bp libraries). We used the DESeq2 workflow to identify changes in gene expression profiles among patients with no, moderate, or high levels of p53 aggregates.

Results

The transcriptome analysis revealed 114 differentially regulated transcripts between patients with high and moderate p53 aggregation, 529 transcripts between high and negative, and 500 transcripts between moderate and negative aggregation levels. The Gene Ontology (GO) analysis showed that significantly deregulated genes in high vs. moderate and high vs. negative were involved in immune response, DNA replication, damage, and repair. Further, we identified a set of 55 genes that are uniquely deregulated

in patients with high p53 aggregation, including nine p53 target genes such as WRAP53 and MYEOV.

Conclusion

Our transcriptome analysis revealed distinct gene expression profiles among OC patients with varying p53 aggregation levels in their primary tumors. Further analysis is required to understand p53 aggregation-related mechanisms and their implications for ovarian cancer, but our preliminary results suggest that altered pathways include immune response and DNA damage/repair pathways.

Acknowledgement

We thank the Biomedical Sequencing Facility at CeMM for assistance with next-generation sequencing.

References

[1] Heinzl N, Maritschnegg E, Koziel K, Schilhart-Wallisch C, Heinze G, Yang WL, Bast RC, Sehouli J, Braicu EI, Vergote I et al: Amyloid-like p53 as prognostic biomarker in serous ovarian cancer-a study of the OVCAD consortium. Oncogene 2023, 42(33):2473-2484.

FROM NON-INVASIVE PRENATAL TESTING TO CANCER SCREENING: A TRANSLATIONAL JOURNEY IN CFDNA-BASED ONCOLOGY

Ondrej Pos[1,2], Zuzana Hanzlikova[2,3], Jakub Styk[1,2], Silvia Bokorova[1,2], Lydia Lukyova[1,4], Monika Kubanova[1,5], Terezia Duranova[1,5], Werner Krampl[1,2], Tatiana Sedlackova[1,2], Jaroslav Budis[1,2,6], Pavol Janega[7], Tomas Szemes[1,2,4]

[1]*Comenius University Science Park, Bratislava, Slovakia*
[2]*Geneton Ltd., Bratislava, Slovakia*
[3]*Slovak Academy of Sciences, Institute of Clinical and Translational Research, Biomedical Research Center, Bratislava, Slovakia*
[4]*Department of Molecular Biology, Faculty of Natural Sciences, Comenius University, Bratislava, Slovakia*
[5]*Institute of Medical Biology, Genetics and Clinical Genetics, Faculty of Medicine, Comenius University, Bratislava, Slovakia*
[6]*Slovak Center of Scientific and Technical Information, Bratislava, Slovakia*
[7]*Institute of Pathological Anatomy, Faculty of Medicine, Comenius University, Bratislava*

Low-coverage whole-genome sequencing of cell-free DNA (cfDNA) has demonstrated clinical utility in non-invasive prenatal testing (NIPT), enabling reliable detection of fetal chromosomal abnormalities from maternal plasma. Building on these principles, our research team explore whether similar genome-wide cfDNA approach could be translated into oncology, with the long-term goal of developing a minimally invasive cancer screening strategy.

Our initial experiments adapted NIPT-like analytical workflows to plasma cfDNA from colorectal cancer patients, focusing on genome-wide copy number variation (CNV) profiles. These early analyses revealed increasing CNV burden and genomic instability with advancing tumor stage, including recurrent alterations affecting genes associated with malignant transformation. However, the lack of well-matched control cohorts highlighted a key limitation for population-level screening. To further refine our approach, we analyzed publicly available whole-genome cfDNA datasets spanning multiple tumor entities and healthy cohorts. These analyses demonstrated that CNV profiles alone lack sufficient universality as standalone cancer biomarkers and underscored the importance of technical standardization and biological context. Consequently, we shifted from single-feature analyses toward integrative cfDNA profiling, incorporating mutation patterns, cfDNA fragmentation characteristics, and additional qualitative and quantitative sequencing features. Fragment length distributions, in particular, reflected tumor biology and differentiation status. At the same time, we observed that numerous physiological and pathological factors substantially influence cfDNA properties and complicate cancer screening in real-world populations.

Overall, our experience illustrates that effective cfDNA-based cancer screening requires integrative analytical frameworks capable of capturing biological complexity

and population heterogeneity, rather than reliance on isolated biomarkers. These insights underpin our ongoing efforts to develop robust, scalable, and clinically meaningful non-invasive screening tools.

Acknowledgement

This work was supported by the Slovak Research and Development Agency grants APVV-23-0520 (INHALE) and VV-MVP-24-0290 (GESTALT). Additional support was provided by the Horizon Europe programme under grant no. 101160008 (FORGENOM II) and grant no. 101213916 (PREDI-LYNCH).